SUBWAVELENGTH ANTIREFLECTION FOR SPACE APPLICATIONS

HUGH PODMORE

A THESIS SUBMITTED TO THE FACULTY OF GRADUATE STUDIES
IN PARTIAL FULFILMENT OF THE REQUIREMENTS
FOR THE DEGREE OF

MASTER OF SCIENCE

GRADUATE PROGRAM IN EARTH AND SPACE SCIENCE
YORK UNIVERSITY
TORONTO, ONTARIO
AUGUST 2015

Abstract

In this research the potential for CubeSat power enhancement through the application of bio-mimetic subwavelength antireflective nanostructures to solar cell coverglass is investigated. Antireflective nanostructures derived from the eyes of moths are simulated using effective medium theory and rigorous coupled wave analysis in order to determine the impact of subwavelength antireflection (SWAR) on CubeSat power budgets. An optimized SWAR structure for CubeSat applications using commercially available triple junction solar cells is designed, and design rules for the space environment are presented. SWAR structures were fabricated on quartz and a novel single-step fabrication process was developed which was shown to produce structures close to the optimized design. The impact of SWAR structures on solar-cell power production at incidence angles from 0° to 85° was demonstrated experimentally using a purpose-built solar simulator environment. Solar-angle simulations for CubeSats in a variety of attitudes and orbits were carried out using experimentally determined values for solar cell power production and it was determined that SWAR-enhancement may increase CubeSat power production by as much as 10%.

"The first principle is that you must not fool yourself and you are the easiest person to fool." – Richard Feynman

Acknowledgements

First and foremost this research would not have been possible without the guidance and support of my supervisor, Prof. Regina Lee who gave me the freedom to pursue my ideas, as well as the focus and direction to see them through. I have benefited immensely from Prof. Lee's counsel on space technologies, attitude control, microfabrication, effective research methods and much more.

I would also like to extend my thanks to Prof. Brendan Quine for his support of this research in the form of laboratory space in the CRESS Space Instrumentation Laboratory clean-room. To Dr. Henry Lee, Yimin Zhou and the Toronto NanoFabrication Centre I also extend my gratitude for allowing me access to their fabrication facilities and for their technical support. Furthermore I would like to express my gratitude to Dr. Brian Solheim for providing the laboratory space and equipment required for experimental validation of the research, as well as advice for achieving greater repeatability in terms of optical alignment. I would also like to gratefully acknowledge Prof. Michael Daly for providing equipment used for calibration and characterization.

To my friend and tireless research assistant, Juan Guzman, I extend my sincere gratitude. There were so many moving components to this research that it would not have been possible without your help and I appreciate greatly the bright, inquisitive and hard-working manner in which you supported this research.

To my lab mates Andrew Lohman, Thong Thai, Sriyan Wisnarama, Guy Benari, Kartheephan Sathiyanathan, Thomas Wright and Arthur Lin, thank you for the shared camaraderie, team spirit and for being willing to discuss my wild theories and research obstacles. Thanks especially are due to my friend and lab mate Patrick Irvin for providing a listening ear, a critical eye and a helping hand. To everyone who kept me well-fed throughout the last two years, and everyone who ever had to hear my complaints: thank you for your patience and for your friendship, they mean the world to me. To Hermina, thank you for helping me to keep on swimming.

I would also like to thank and acknowledge all of the teachers and supervisors over the many years who have had a positive influence on my outlook in life and on my personal development as a scientist and a person. Most importantly, thanks are due to Dr. Jean Dupuis of the Canadian Space Agency and Dr. Pierre-Olivier Quirion–who first set me on my path to independent research.

The greatest thanks of all are due to my family and especially to my parents: Neil and Dorothy Podmore. Thank you for your decades of love and support, your kindness and your patience.

Table of Contents

List of Tables

List of Figures

1 Introduction and Motivation

Space has long been the near exclusive purview of large government sponsored mega-engineering projects. The Hubble Telescope, the International Space Station, and the upcoming James Webb Space telescope are all massive investments of capital and expertise by participating government agencies–and the list goes on. The reason for the traditional dominance of governmental agencies above the stratosphere are myriad but are chiefly a consequence of the high financial, technical and regulatory barriers to entry into space. Recently these barriers have begun to fall, as small satellites *i.e.* satellites with total mass under $500kg$ are increasingly welcome to participate in major space launches. Unused capacity on major launch vehicles may be filled using small satellites, microsatellites (mass less than $100kg$), and nanosatellites (mass less than $10kg$) in order to maximize the utility of any one single launch. These ride-sharing programs significantly lower the cost of entry for small satellite developers, which has lead to incredible growth in nanosatellite and microsatellite development.

Nanosatellites in particular saw explosive growth following the introduction of a standardized form factor, the "CubeSat" and a standardized deployment method, the Poly-Picosatellite Orbital Deployer (P-POD). CubeSats are small, modular satellites that consist of integer or half-integer numbers of "Units" that have been joined together. A single CubeSat unit is a $10cm$ by $10cm$ by $10cm$ cube with total mass less than one kilogram. A CubeSat consisting of just one of these units would be referred to as a 1-unit or "1-U" CubeSat; two units joined together make a 2-U, three units a 3-U and so on. This modular approach to nanosatellite form-factor has allowed for the standardization of components that, in the past, were custom built for each new mission. Access to standard components thus shortens the turnaround time for satellite development, but also further lowers the barriers to entry. In the past ten years CubeSats have become the platform of choice for low-cost, short-term missions in Low Earth Orbit (LEO). Some example applications for a CubeSat mission include *in-situ* measurements of the mid to lower thermosphere, characterizing the LEO radiation environment [5], or even simple earth imaging. CubeSats are often used for educational and training purposes as they are a cheap path for graduate and undergraduate students to gain hands on experience in satellite systems engineering. CubeSats are also an ideal vehicle for technology demonstration and space qualification, indeed many CubeSats fly with no grander purpose than merely demonstrating that a certain technology works in the space environment. So called "beepsats" make up a large percentage of 1-U CubeSat flights.

Over 300 CubeSats have now been flown, and an ever increasing number of these satellites are 3-U CubeSats flown with a primary scientific or technical objective [6, 7]. Scientific missions, however, carry more stringent technical demands than mere beepsats. Primarily, scientific missions such as direct earth observation (EO), remote-sensing and astronomy require precise knowledge and control of spacecraft attitude. Attitude determination and control systems (ACS) are somewhat unique in that they are difficult to miniaturize. Reaction wheels are the traditional actuator for an ACS, and a reaction wheel is by definition a spinning wheel with a high angular moment of inertia *i.e.* it is either large in diameter, massive, or both. CubeSats, however, are limited by their $10cm^3$ form factors: any component or subsystem, including the ACS, must fit inside some combination of CubeSat units. Precise pointing is still possible using the CubeSat platform, however limiting the size and mass of the ACS restricts the total output torque that may be generated by the system reducing the ability of a CubeSat to compensate for destabilizing forces such as disturbance torques and flexible structures.

In addition to precise attitude knowledge and control scientific observations typically require high levels of power draw. A portion of this power draw will necessarily go to the ACS in order to maintain fine pointing control, and another large portion will go to the scientific payload. As the required accuracy of the scientific measurement goes up, so too does the

power draw; the same can be said for the frequency of observations. Hence, the ability of a particular CubeSat to perform high-quality science is dependent on its ability to generate and store power. As a rule, power generation on CubeSats is performed using solar cells, therefore the ability of a CubeSat to generate power is dependent on the capabilities and configuration of its solar cells.

Nanosatellites and other small satellites rely on body mounted solar panels, and occasionally extendible solar arrays to generate electrical power [8]. Unfortunately, the CubeSat is a low volume spacecraft and only a small amount of physical surface area will be available for solar power generation, hence scientific capabilities will be similarly limited. In a conventional satellite this issue would be resolved by the addition of large, deployable, sun-tracking solar arrays that increase the amount of surface area available for power generation. However, the flexible nature of these arrays will place greater demands on the ACS system on a CubeSat, hence large solar arrays may not always be desirable or even possible. Beyond the consideration of mere surface area, low power-production is also a consequence of high angles of incidence of those surfaces with respect to the sun. Lacking large, sun-tracking arrays, the solar panels on CubeSats will often experience high angles of incidence with respect to the sun. Solar power generation is strongly affected by incidence angle as the visible surface area is reduced at oblique incidence and the reflectance of a surface at high incidence is also greatly increased [9]. CubeSat missions with scientific objectives therefore face a difficult

design trade-off: increased science output requires increased surface area, however increased surface area places additional demands on the ACS, potentially limiting scientific output. It is possible to increase the power budget of a CubeSat through improved power storage, however the frequency of scientific observations will be determined by the ability of a CubeSat to generate power–not to store it.

A third, and under-explored option in the field of nanosatellite research is to improve the efficiency of the solar cells themselves. It is not surprising that this solution path has been overlooked, as CubeSat developers and solar-cell manufacturers are members of two very different fields of study. The field of photovoltaic research is well defined and broadly self contained; it is somewhat separate from the space industry, and where it does overlap it is focused primarily on the interests and objectives of traditional, major satellites. CubeSat developers on the other hand tend to purchase commercial off-the-shelf (COTS) cells in bulk from third-party suppliers, and have little interest in their properties. Indeed, until recently some of the most popular cells for CubeSats were assembled from by-products and clippings left over from major satellite cells–an apt metaphor for the level of involvement of CubeSat developers. The developers of large satellites are not as limited as developers of CubeSats are in terms of the volume and mass of their spacecraft. Accordingly, it is of comparatively little consequence to address the efficiency of solar cells at high angles of incidence. If the angles of incidence on a large satellite are too high, actively-tracking arrays can always be employed

to resolve the power deficit. CubeSat developers do not have this capability, and yet have remained unable or unwilling to address the issue of power generation at the solar-cell level.

1.1 Contributions of The Thesis

In the fields of optical and RF physics, as well as micro and nanofabrication there is a well known method for increasing the absorption of light in silicon photodiodes: subwavelength antireflection (SWAR). SWAR techniques have been successfully applied to reduce the reflection of electromagnetic waves in radio, microwave, infrared, optical, and ultraviolet systems. Reduced reflectance in these systems using SWAR, particularly silicon photo diodes, has been shown to demonstrate increased photovoltaic power-production–particularly at high angles of incidence. SWAR technology as applied to CubeSats is an interesting avenue of inquiry as SWAR is a passive technology that places no additional demands on the mass or volume of a satellite. In addition, SWAR is not exclusive to CubeSats nor is SWAR incompatible with solar arrays; it is a highly generalizable technique that has a wide range of applications.

Recently, moth-eye antireflection (MEAR) techniques–a subset of SWAR–have been applied to the protective coverglass layers of COTS silicon solar cells in order to improve overall power generation without risk of damaging the cells themselves [10–12]. This finding is par-

ticularly applicable to CubeSat developers as solar cells flown in space nearly always deploy a coverglass layer in order to protect cells from radiation damage, and these coverglass layers are quite often purchased separately from the cells themselves. Despite impressive increases in performance, the fabrication approaches developed to produce these enhanced coverglass layers are not suitable for space application. The MEAR and SWAR structures that have been demonstrated to-date are either unsuitable for broadband triple-junction cells, or are insufficiently robust for the space environment. Though the theory behind SWAR has been well understood for years, fabricating SWAR surfaces is a non-trivial task and it is only recently that advances in micro and nanofabrication techniques have opened the door to space-qualified SWAR.

It is now reasonable to investigate the potential for SWAR technology to improve CubeSat power generation, and this is the fundamental question that this research seeks to address. The main contributions of this research are as follows:

1. The theoretical case for applying SWAR to CubeSat missions is investigated using conventional SWAR models and CubeSat attitude simulations.

2. The design of optimal MEAR surfaces for CubeSat applications is investigated and a constrained optimized design is presented for maximal transmittance at normal incidence.

3. Low-cost manufacturing techniques suitable for CubeSat developers are investigated and it is determined that traditional fabrication methods are unsuitable for space applications.

4. A novel, single-step, low-cost manufacturing technique suitable for space applications is developed making SWAR accessible to CubeSat developers.

5. Increased power-production in COTS solar-cells through the application of SWAR-enhanced coverglass was experimentally verified.

6. Single-step fabricated SWAR glass was shown to increase power-production on orbit by $\sim 7\%$ over untreated glass, and by $\sim 5.5\%$ over a conventional AR coating.

This thesis is separated into five chapters. Chapter 1 introduces the rationale behind the investigation of SWAR surfaces for satellite applications and lists the key contributions of the research. Chapter 2 describes the theoretical background of moth-eye antireflection, current modelling techniques, SWAR and MEAR optimization for space applications and solar-cell performance simulations. Chapter 3 provides a treatment of current manufacturing approaches, highlighting those which are suitable for space application. Chapter 3 also details the fabrication approaches pursued throughout the course of this research, as well as the development of a novel single-step fabrication method. Chapter 4 details the experimental validation of SWAR technology applied to coverglass on COTS cells; the results of this experiment are presented and discussed as well as the implications for CubeSat power

budgets. Chapter 5 concludes the thesis, summarizes the contributions of the research and discusses implications and future work.

2 Theory and Modeling

Moth-eye antireflection (MEAR), is a subset of the more general field of SWAR and is a well studied technology for reducing reflection at the interface between two adjacent media. By definition, a moth-eye surface consists of a two-dimensional periodic array of cones, rods, paraboloids or similar geometric structures fabricated on the surface of the interface [13]. SWAR surfaces are similar in that structures on the surface must be spaced more tightly than the wavelenghts of incident light, however SWAR structures are not required to have a well-defined or ordered structure–black silicon is the classic example of a SWAR surface [14]. Moth-eye antireflection takes its name from the eyes of the eponymous arthropod where these surface features were first observed [15] as illustrated in Fig 2.1. The fabrication of synthetic moth-eye structures on silicon has since been repeatedly shown to increase the transmission of light at the air/Si interface, and subsequent work has demonstrated that the effect is repeatable at the air/SiO_2 interface [10, 11, 16–18].

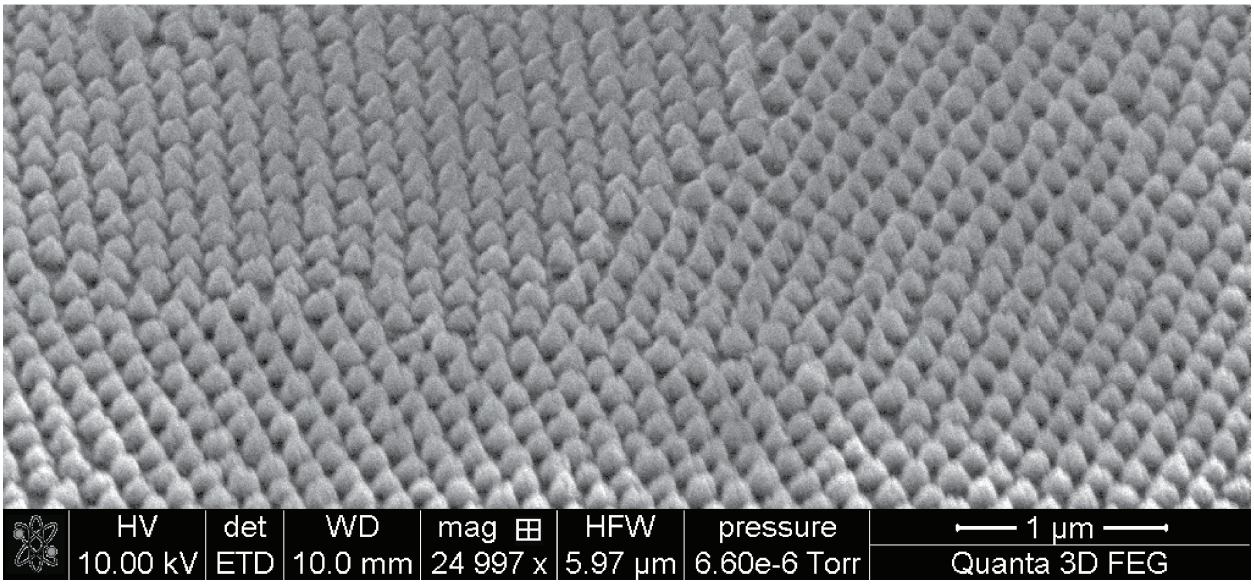

Fig. 2.1 Artificial MEAR surface fabricated on SiO_2. MEAR surfaces are defined to consist of well-ordered, hexagonally-spaced arrays of subwavelength structures.

2.1 The Moth-Eye Principle

Fundamentally, the SWAR and MEAR effects enhance the transmission across a boundary between two media through the use of a smoothly graded change in the refractive index. The impedance of the overall transition is minimized by introducing an intermediate "transition" layer with a precisely engineered refractive index. An instructive example of refractive index engineering for lossless transmission is the single quarter-wavelength antireflection (AR) film first described by Lord Rayleigh [19]. A quarter-wavelength AR coating consists of a transition layer of height h and refractive index n_L sandwiched between two media of refractive indices n_0 and n_1. Reflection of light is minimized at the wavelength λ_0 and the

height of the AR layer is given by $\lambda_0 = 4h \cdot n_L$. At the "central" wavelength, λ_0, incoming light will reflect from the primary surface with some phase $\phi_{\mathrm{R1}} = \phi_{\mathrm{inc}} + \pi$ where ϕ_{inc} is the phase of the incident light. The incident ray continues to propagate through the quarter-wavelength film, gaining phase shift $\delta\phi_{\mathrm{inc}} = \pi/2$ in the process; at the interface with the secondary boundary another reflection occurs producing a second reflected wave with phase $\phi_{\mathrm{R2}} = \phi_{\mathrm{inc}} + \pi/2 + \pi$, this reflected wave traverses the quarter-wavelength film again and arrives at the primary surface with total phase $\phi_{\mathrm{R2}} = \phi_{\mathrm{inc}} + 2\pi$, *i.e.* the second reflected wave R2 will be out of phase with respect to the first reflected wave, R1 by π. This process is shown schematically in Fig 2.2.

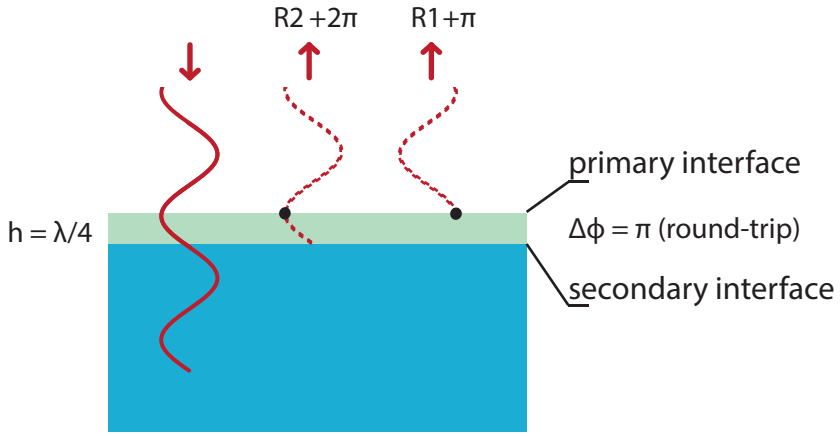

Fig. 2.2 Diagram showing an incident light wave (left) along with its two reflected components $R1$ and $R2$ (right) and their respective phases due to the geometry of the quarter-wavelength AR coating.

Destructive interference between these two reflected components will reduce the total

intensity of the reflected light and increase the intensity of the transmitted light for one specific wavelength. This effect can be further improved by engineering the refractive index of the quarter-wavelength film such that the intensity of the reflected wave at the primary interface is equal to the intensity of the interfering wave produced by reflection at the second interface. The refractive index at which optimal antireflection will occur is given by the geometric mean of the two materials $n_L = \sqrt{n_0 n_1}$.

One drawback of Single layer AR coatings is that they strongly reduce reflection at only the central wavelength, λ_0, and the AR effect is diminished as the difference in wavelength from λ_0 is increased. This effect may be mitigated by introducing multi-layered thin-film AR structures which will produce a more broadband effect, although historically minimized reflectance has been best achieved using smoothly graded changes in the refractive index [13]. To understand why this is the case it is useful to consider the case of generalized wave-impedance. For an electromagnetic wave travelling across the boundary between two media the discontinuity at the boundary produces a reflected wave propagating in the opposite direction from the first. The reflection coefficient corresponding to this component is a function of the wave-impedances, Z, of the two media such that:

$$r = \frac{Z_1 - Z_0}{Z_1 + Z_0}. \tag{2.1}$$

Eliminating impedance mismatch, in this case the difference between Z_0 and Z_1, elimi-

nates the reflectance of the wave. For optical systems, the wave-impedance is determined by the refractive index of the media. As the wave enters this new media it will excite periodic motion in the charged particles of the lattice structure of that media; if the lattice structure of the two media are sufficiently different then a phase-lag will occur. The wave-impedance may be thought of as a measure of the phase-lag between two media. The greater the wave-impedance the greater the phase lag between the two media, and for two media in which no phase-lag occur there will be no change in impedance and therefore no reflection. A slowly graded change in the refractive index is expected to mitigate the onset of this phase-lag which will result in a system in which the light does not ever encounter a "hard" boundary in terms of impedance mismatch. In such a system, the reflection at any particular point is expected to be very low. Recently, an analytical solution to electromagnetic impedance matching in microwave systems has been found, and the resulting structures have been demonstrated to yield perfect antireflection, validating the impedance matching approach [20]. The analytical solution suggests, contrary to expectations, that a discontinuity in the refractive index at the beginning and end of the GRIN region is required for an ultra-thin AR layer to produce perfectly matched impedances across the interface. It is not clear, however, that this requirement will translate well to optical systems, in fact the analytical solution for permittivity found by Kim and Park suggests that for GRIN regions of sufficient height zero discontinuity is still preferred.

A physical explanation relating a GRIN transition to the quarter-wavelength coating

is the scenario in which a GRIN region is discretized into an infinite stack of thin-films. These thin films are assumed to be of monotonically increasing index, n_i, where i refers to the i-th layer of the stack. As a light wave propagates through this infinite stack of thin films it produces an infinite number of reflections, similar to the reflections produced by the quarter-wavelength coating in Fig 2.2. Each of these reflections, R_i, will have some different phase ϕ_i corresponding to its spatial position in the AR structure. If the optical path of the entire stack is longer than $\lambda_0/2$ then all phases of light will be present in the set of reflected components. Hence, as these components propagate backwards to the primary interface all phases will be present at the primary interface. If all phases of the incident light are present at the primary interface then destructive interference occurs and the sum of the reflected components can fall to zero provided that the amplitudes of each reflected component are matched. Amplitude matching may be achieved by tailoring the profile of the change in refractive index; in reality a monotonic increase in the refractive index is unlikely to be ideal–a smooth function will be preferred. It has been demonstrated that for a GRIN region of height h minimal reflectance may first occur for a monochromatic source at $h = 0.4\lambda_0$ after which a series of maxima and minima occur as h is increased [13]. It is therefore possible to achieve near total transmission across a broad, arbitrary waveband spanning $\lambda_{min} < \lambda < \lambda_{max}$ through the use of a GRIN region with $h > 0.4\lambda_{max}$.

A GRIN region may be formed through the use of ultra-finely spaced structures composed

of a heterogeneous mixture of materials. To illustrate this point it is useful to consider the case of the simple square refraction grating with height h and pitch Λ under illumination from a single monochromatic source with wavelength λ_0 and incident angle θ_{inc} as shown in Fig 2.3. Light reflected by this grating will be diffracted into N different diffraction orders each with diffraction angle θ_m given by the formula

$$\theta_m = arcsin(\frac{m\lambda_0}{n_1\Lambda} - sin\theta_{\text{inc}}) \tag{2.2}$$

in which it should be apparent that the pitch (spacing) of the grating, Λ and the refractive index of the grating material n_1 control the diffractive properties of the entire system. The grating is operates in the subwavelength regime when $n_2\Lambda < \lambda_0$; if we consider the case in which $\theta_{\text{inc}} = 0$ then the right hand sinusoidal term in Eq 2.2 will disappear, if we then apply the subwavelength condition to this system then we see that there is no real solution for θ_m where $m > 0$. In physical terms, entering the subwavelength regime strongly suppresses all diffraction orders above the 0-th, and therefore the reflection and transmission of light will be purely specular. For incident angles greater than 0 a more stringent form of the subwavelength condition is given by the limiting case of $\theta_{\text{inc}} = 90°$, yielding the requirement

$$\frac{m\lambda_0}{n_1\Lambda} - 1 > 1 \implies \lambda > 2n_1\Lambda. \tag{2.3}$$

For a diffraction grating with sufficiently fine spacing, then, specular reflection and transmission will be guaranteed [9, 13]. In this scenario the light is unable to resolve the diffraction grating, meaning that the light cannot perceive the individual structure of the grating and

instead perceives only a region with some inhomogeneous distribution of refractive index. Since the light is unable to resolve these regions of varying refractive index into discrete areas the overall refractive index of the grating at any point will be determined by some combination of the substrate and vacuum index as described by Effective Medium Theory [9,21,22].

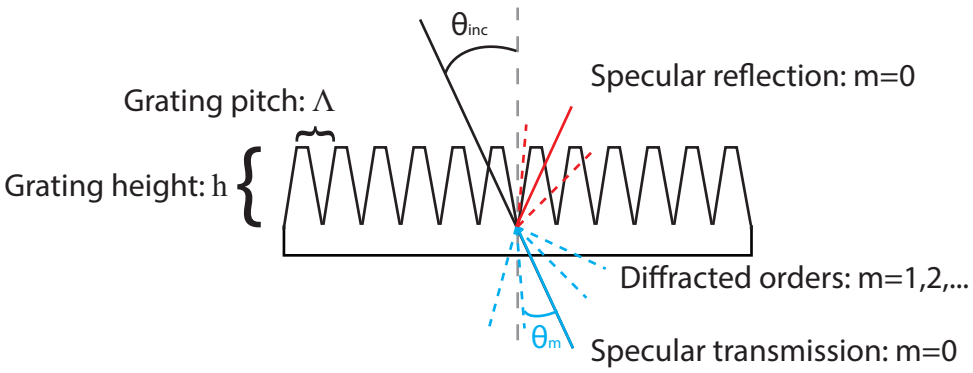

Fig. 2.3 Simple 1D diffraction grating with height h, pitch Λ showing specular transmittance (blue) with orders $m = \{-2, -1, 0, 1, 2\}$ and reflectance (red, $m = \{-1, 0, 1\}$).

In summary, enforcing the subwavelength condition given by Eq 2.3 will ensure that the reflection and transmission of a diffraction grating will be determined solely by specular effects, and that the refractive index at any point in the grating may be described by the refractive indices of the surrounding media. The profile of the diffraction grating may therefore be tailored to produce a GRIN structure with a smoothly increasing index of refraction, and if the height of that grating is greater than $0.4\lambda_0$ then destructive interference of the reflected light is guaranteed, and the reflectance of the overall structure will be significantly

reduced.

2.2 Thin-Film Model

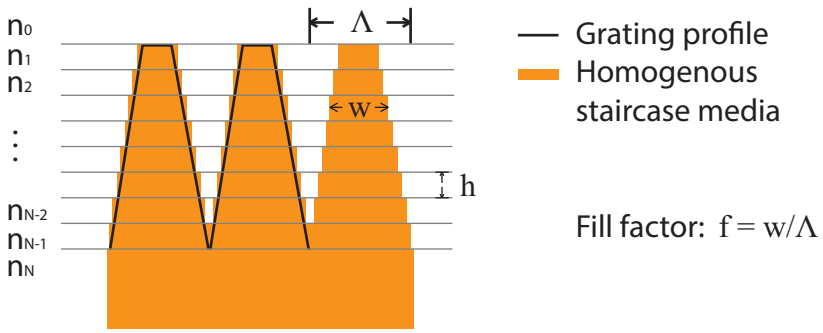

Fig. 2.4 Staircase approximation for 1D diffraction grating with substrate index n_N and bulk media index n_0, the fill factor is defined as $f = w/\Lambda$.

MEAR structures in the subwavelength regime suppress diffraction orders above the 0-th and permit only specular components of reflection and transmission; the same process occurs for the more general case of SWAR, MEAR is used in this example for the benefit of its simplicity. Following the approach of Ono *et al.* [9] it is then possible to use the transfer matrix method (TMM) to model a MEAR structure as a many-layered stack of thin films. In this model light incident upon the stack with angle θ_i from the normal propagates through N films, each with thickness d, and transmission matrices T_i given by the equation

$$T_i = \begin{pmatrix} \cos\delta_i & (j/\omega_i)\sin\delta_i \\ j\omega_i & \cos\delta_i \end{pmatrix}, \tag{2.4}$$

where $\delta_i = \frac{2\pi}{\lambda} n_i d \cos(\theta_i)$ is the phase of light at the beginning of the i-th layer in the N-layered stack. ω_i defines the impedance at each layer, which is itself dependent on the polarization of light,

$$\omega_i = \begin{cases} n_i \cos(\theta_i); TE - polarized, \\ n_i / \cos(\theta_i); TM - polarized. \end{cases} \tag{2.5}$$

Where TE-polarized refers to light in which the time-varying electric field is aligned perpendicular to the direction of propagation, and parallel to the plane of the surface of the stack. TM-polarized light refers to light in which the time-varying electric field is aligned perpendicular to the direction of propagation and parallel to the plane of incidence. Light from an unpolarized source such as the sun is considered to consist of equal parts TM and TE-polarized light, each of which will interact with the surface differently. The convolution of the matrices in Eq 2.4 yields the Fresnel reflectance and transmittance-which correspond to the total reflectance and transmittance of the stack in the case where $m = 0$:

$$\prod_{i=1}^{N} T_i = \begin{pmatrix} A & B \\ C & D \end{pmatrix}. \tag{2.6}$$

This gives reflectance, R, at the air-stack-substrate interface of

$$R = \left| \frac{\omega_0 A + \omega_0 \omega_N B - C - \omega_N D}{\omega_0 A + \omega_0 \omega_N B + C + \omega_N D} \right|^2. \tag{2.7}$$

This equation is highly analogous to the generalized expression for reflection coefficients due to a change in impedance presented in Eq 2.1. The refractive indices at each layer in the film may be defined according to the fill factor of the grating at that height. In this research a staircase approximation is used in which the grating structure is discretized into a "staircase"

of rectangular blocks of equal height and gradually increasing width as shown in fig 2.4. This staircase approximation yields the refractive index at each layer

$$n_i = \sqrt{(1/n_0^2)f + (1/n_N^2)(1-f)} \tag{2.8}$$

where n_0 refers to the refractive index of the incident media, and n_N is the refractive index of the final media, *i.e.* the substrate. The volume fraction, f, or "fill-factor" is defined as the ratio of the stair width to grating period Λ at the i-th layer in the staircase.

Tailoring the profile of the MEAR structure, or the average profile of SWAR structures, is a a method well-suited to control the grade in refractive index between a vacuum into the coverglass or solar cell. As discussed previously, producing a GRIN structure of sufficient height is guaranteed to improve the transmission of light; using the TMM formulation of MEAR or SWAR structures it is now possible to numerically evaluate the overall performance of a surface.

To model the performance of MEAR surfaces using the TMM formulation, the free optical simulation package OPTISCAN developed at the University of Arizona is used to determine the transmittance and reflectance of this thin-film stack [23]. The OPTISCAN thin-film calculator calculates the Fresnel reflectance and transmittance for a thin-film system using the same formulation as presented in Eqs 2.4- 2.7. By performing this calculation over a range of wavelengths $\lambda_{min} < \lambda < \lambda_{max}$ and incidence angles $\theta_{min} < \theta < \theta_{max}$ the information

required to characterize solar cell performance may be determined.

There are some limitations of the EMT-TMM formulation as applied to MEAR and SWAR structures: specifically, while EMT-TMM simulations perform well in description of these systems at normal angles of incidence they have been shown to break down at higher angles of incidence [21, 24]. There is some disagreement over the threshold at which EMT fails to accurately describe the refractive index of a grating. Many authors choose to restrict the use of EMT to features with periodicity less than one tenth of the wavelength of incoming light however the mathematical basis of $n\Lambda/\lambda < 1$ remains popular. The reliability of EMT-TMM simulations are known to be strongly dependent on the strength of the subwavelength condition; this may explain the break-down in EMT-TMM observed by previous authors. In work by Foberich *et al.* MEAR structures with a periodic spacing of approximately $300nm$ are used to decrease the reflectance over the range $350nm < \lambda < 800nm$ [24]. The solar cells used in this experiment provide peak power-production at a wavelength of $550nm$, however this wavelength would be expected to violate Eq 2.3 at a mere 15° incident angle. The performance of their MEAR enhanced solar cell is shown to fully diverge from the simulated performance at 60°, however the trends of the simulated and experimental results begin to exhibit disagreement as early as 20°. These results demonstrate the importance of applying the TMM formulation to cells in which the subwavelength condition is strongly guaranteed, especially at higher angles of incidence.

2.3 Rigorous Coupled-Wave Analysis

Another method for determining the effective transmittance and reflectance of MEAR surfaces which is commonly used is three dimensional rigorous coupled wave analysis (3D-RCWA), in which the MEAR structures are discretized in both the horizontal and vertical domains and a more robust method of light propagation is used to determine the transmittance and reflectance of the structure. Similar to the TMM formulation, structures defined in RCWA are often discretized using a staircase approximation [21], however in each spatial block or step of the 3D-RCWA structure the propagation of light is determined by numerically solving Maxwell's equations rather than using a thin-film approximation to the Fresnel reflectance and transmittance.

The general RCWA algorithm in top-down propagation (*i.e.* free-space-into-substrate) proceeds as follows. For some arbitrary step in a staircase-approximated structure initial values of the time-varying electric field, **E(z,t)** and the time varying magnetic field, **H(z,t)** are defined for one side of step. The corresponding fields at the opposite boundary of the step may then be calculated by the propagation of light through the block according to Maxwell's equations. These calculated field values are then defined as initial field conditions for all adjacent blocks. By matching boundary conditions in this manner light may be propagated

through any arbitrary structure with a high degree of accuracy. For a MEAR surface, an incident plane wave will define the boundary conditions at the highest accessible step in a staircase similar to the structures shown in Fig 2.5. Light will be propagated through each of these blocks until the substrate at the bottom of the staircase is reached and the boundary conditions at the end of the N-th step are known. The intensities of the **E(z,t)** and **H(z,t)** fields entering the substrate relative to the intensities of the very first initial conditions then define the transmittance and reflectance of the entire MEAR structure. Throughout this process, and unlike in EMT-TMM, each block in the staircase is assumed to be composed of a homogeneous medium such as SiO_2 with complex permittivity $\epsilon = \sqrt{n}$. The lack of any explicit EMT formulation of the permittivity and refractive index ensures that the RCWA method is robust to the subwavelength constraint. Hence, RCWA simulations can be relied upon to produce accurate expected values for the transmittance and reflectance of MEAR surfaces, regardless of their particular geometries.

In this research the commercially available GD-CALC software (KJ Innovation) was used to model the performance of MEAR structures of various heights, periods and vertical profiles. Initial simulation work was performed using EMT-TMM and RCWA was later employed to ensure reliability of these results as well as provide a robust estimate of an optimized MEAR design based on the observed profiles and periodicity of the final etched structures.

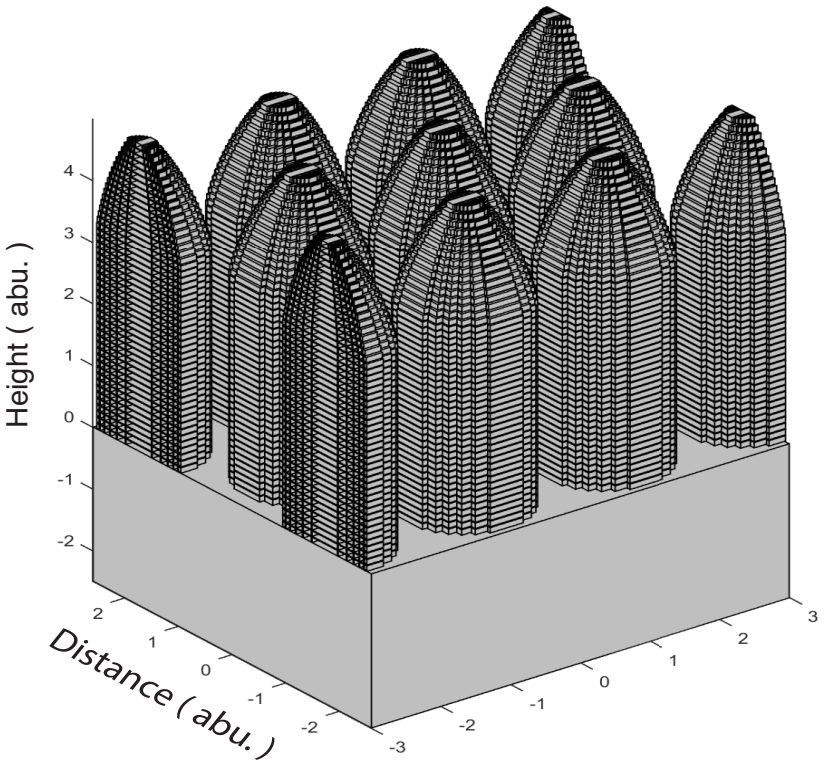

Fig. 2.5 Grating structure for use in RCWA. Produced by GD-CALC using a staircase approximation in three dimensions.

2.4 Simulation and optimization of MEAR surfaces

The objective of both the TMM and RCWA simulation routines is to generate values for the transmittance and reflectance of MEAR structures as a function of both the incidence angle and wavelength of incident light. These values may be tied to a model for solar-cell responsivity in order to estimate the impact of flying MEAR enhanced solar cells on a CubeSat. Throughout this research commercially available Triangular Advanced Solar

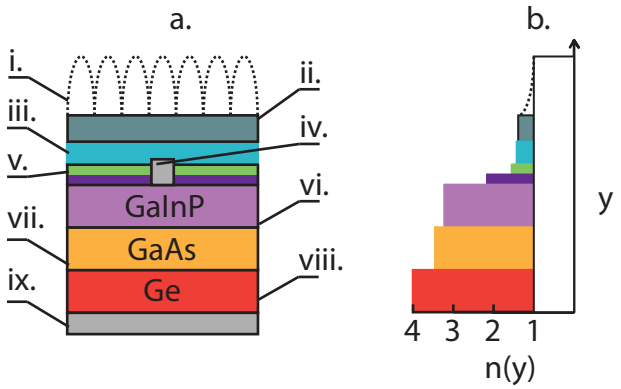

Fig. 2.6 Cross section of a modern triple-junction cell (a), and the corresponding refractive indexes of each media as a function of the height in the stack (b). The triple-junction cell consists of: a SWAR surface structure (i), a protective coverglass layer (ii), index-matching adhesive gel (iii), front contact for current collection (iv), a double layer antireflective coating (v), the $GaInP$ top-cell for blue light-capture (vi), the $GaAs$ mid-cell for yellow and red light-capture(vii), a Ge bottom-cell to capture infrared light (viii) and the rear contact to complete the circuit (ix).

Cells (TASC) were used as the reference cell. TASC cells are small triple junction solar cells consisting of a $GaInP_2$ top cell $GaAs$ mid cell and Ge bottom cell; this structure is shown in Fig 2.6. TASC cells were chosen as a reference cell because of their widespread use. Until their recent decommissioning TASC cells were the solar cell of choice for many CubeSat missions thanks to their low cost and high efficiency. TriSolX Wing cells, the primary successor to TASC, are also similar in structure and performance. In addition, TASC cells are also highly representative of more traditional cells as they are manufactured from clippings of the larger and even more ubiquitous Ultra Triple Junction (UTJ) cells produced

by Spectrolab. The Spectrolab Ultra and Extreme triple junction cell families make up the bulk of today's CubeSat solar cell market and are expected to exhibit a similar response to the TASC cells in terms of MEAR enhancement of the coverglass. Hence, improvements seen in the TASC cells are expected to have implications for nearly all CubeSat, nanosatellite, and microsatellite missions employing COTS solar cells.

MEAR and SWAR surfaces are designed for the air-glass, or vacuum-glass interface despite the relatively low change in refractive index when compared with the adhesive-$GaInP$ transition in Figure 2.6. Addressing the efficiency of the $GaInP$ transition is ideal in terms of the potential impact, however, the addition of MEAR structures to the surface of the $GaInP$ cell may cause defects in the lattice structure at the surface, which would promote greater amounts of carrier-recombination, reducing overall power output. In addition, many triple-junction cells are already packaged with a double-layer AR coating; introducing SWAR to this system would require removal of that layer–likely resulting in surface damage during the process. Furthermore, many fabrication processes that are required in order to realize SWAR surfaces would not be suitable for an integrated solar cell, hence CubeSat developers would not be able to take advantage of the technology in the first place.

The reference spectra used for simulation and cell design was the Air Mass Zero solar spectrum (AM0) developed by the American Society for Testing and Materials (ASTM) [25], which is the accepted standard reference source for solar irradiance observed in LEO. Given

the external quantum efficiency of a TASC cell as a function of wavelength [26], $EQE(\lambda)$, and the solar irradiance, $\beta(\lambda)$ in $W/cm^2/nm$, then the short circuit current of a cell with total projected area $A(\theta) = \int dA(\theta)$ in cm^2 at incident angle θ may be calculated from the equation

$$I_{\mathrm{SC}}(\theta) = \int\int \frac{\lambda \cdot EQE(\lambda)}{1240W \cdot nm/A} \cdot \beta(\lambda)T(\lambda,\theta)d\lambda dA(\theta), \tag{2.9}$$

where $T(\lambda,\theta)$ is a matrix containing the calculated values of transmittance of the MEAR surface, coverglass, and Solar Cell ARC layer (where applicable). $T(\lambda,\theta)$ exhibits dependencies in wavelength and incident angle; it is also dependent on the polarization of incoming light. The reference spectra, $\beta(\lambda)$, and the quantum efficiency of the cell, $QE(\lambda)$, are arbitrary functions that may be populated by data from any light source and solar cell in order to simulate a particular system. Likewise, the projected area $A(\theta)$ for an individual TASC cell may be replaced with the geometric configuration of an arbitrary solar cell or panel of multiple cells such as would be found on the body of a satellite. The short circuit current of the cell is chosen to demonstrate this principle as the maximal power produced by a solar cell is directly related to the short circuit current, and as the change in the open circuit voltage, V_{OC}, is expected to be unaffected by the MEAR effect. The maximal power output of the solar cell, P_{max}, should exhibit a purely linear relationship with $T(\lambda,\theta)$ according to the relationship

$$P_{\mathrm{max}} = \eta I_{\mathrm{SC}} V_{\mathrm{OC}}, \tag{2.10}$$

where η represents the "fill factor", a constant which describes the efficiency of the solar cell

and I_{SC} is related to $T(\lambda, \theta)$ through Eq 2.9.

Given an understanding of this relationship between $T(\lambda, \theta)$ and $P_{\max}(\theta)$, which are related through the short circuit current I_{SC}, it is possible to build up a model of the enhancement in $P_{\max}(\theta)$ from the MEAR effect based on the ratio of $T_{\mathrm{MEAR}}(\lambda, \theta)$ to $T_{\mathrm{BARE}}(\lambda, \theta)$ or to $T_{MgF_2}(\lambda, \theta)$ where the subscripts "$MEAR$", "$BARE$", and "MgF_2 refer to MEAR enhanced coverglass, bare coverglass and coverglass employing a quarter-wavelength AR coating composed of the commonly-used material MgF_2. Detailed knowledge of $P_{\max}(\theta)$ combined with the known configuration of commercially available solar panels, as well as simulated or historical CubeSat attitude data, yields the expected power output on orbit. Altogether, given the well-documented accuracy of RCWA simulation methods, the established theoretical framework behind solar cell operation and the highly-standardized nature of CubeSats, it is expected that the influence of MEAR-enhanced coverglass on a CubeSat power budget may be simulated accurately and with a high degree of confidence.

First, the free optical simulation software OPTISCAN was used to simulate MEAR structures using the EMT-TMM formulation of MEAR transmittance and reflectance. The structures simulated ranged in height from $300 - 800nm$, using both paraboloidal and conical tapered profiles. The TMM method does not allow for investigation into the periodicity of MEAR structures, hence all simulated structures are assumed to have periodicity with suf-

ficiently small spacing to satisfy the subwavelength criterion. When the number of thin-film layers in the EMT-TMM model, N, was greater than 5000 the reflectance and transmittance values computed by OPTISCAN were found to converge. Beyond this threshold the addition of further thin film layers had negligible impact on the computed reflectance and transmittance. Conical and paraboloidal profiles were used in this analysis in order to compare differences in performance due to profile changes in the MEAR structures; the conical profile is known to produce a very strong AR effect [9]. However, pyramids are difficult to fabricate, and the majority of fabricated MEAR structures exhibit paraboloidal-like profiles [10–12, 16, 27, 28]. These two profiles are expected to provide a comparison between the performance of an "ideal" MEAR structure, versus the structures likely to be achieved through fabrication.

Figure 2.7 shows the computed values of transmittance $T(\lambda, \theta)$, of MEAR structures in conical and paraboloidal configurations relative to the transmittance of bare SiO_2 coverglass across the range of operational wavelengths for a TASC cell $(350 - 1800nm)$, across incident angles from $50^\circ - 90^\circ$ assuming equal amounts of p and s type polarized light. High angles of incidence are shown in order to highlight the divergence in performance between the three technologies at high angles of incidence–below 50° the effect is uniform. These relative transmittance values indicate that the application of MEAR structures to SiO_2 coverglass increases the intensity of transmitted light at all wavelengths and, especially at high angles

of incidence. This is to be expected as the bare SiO_2 surface exhibits no AR enhancement. EMT-TMM results also indicate that the application of MEAR structures to SiO_2 coverglass will increase the intensity of transmitted light to a greater degree than that of a traditional thin-film MgF_2 coating.

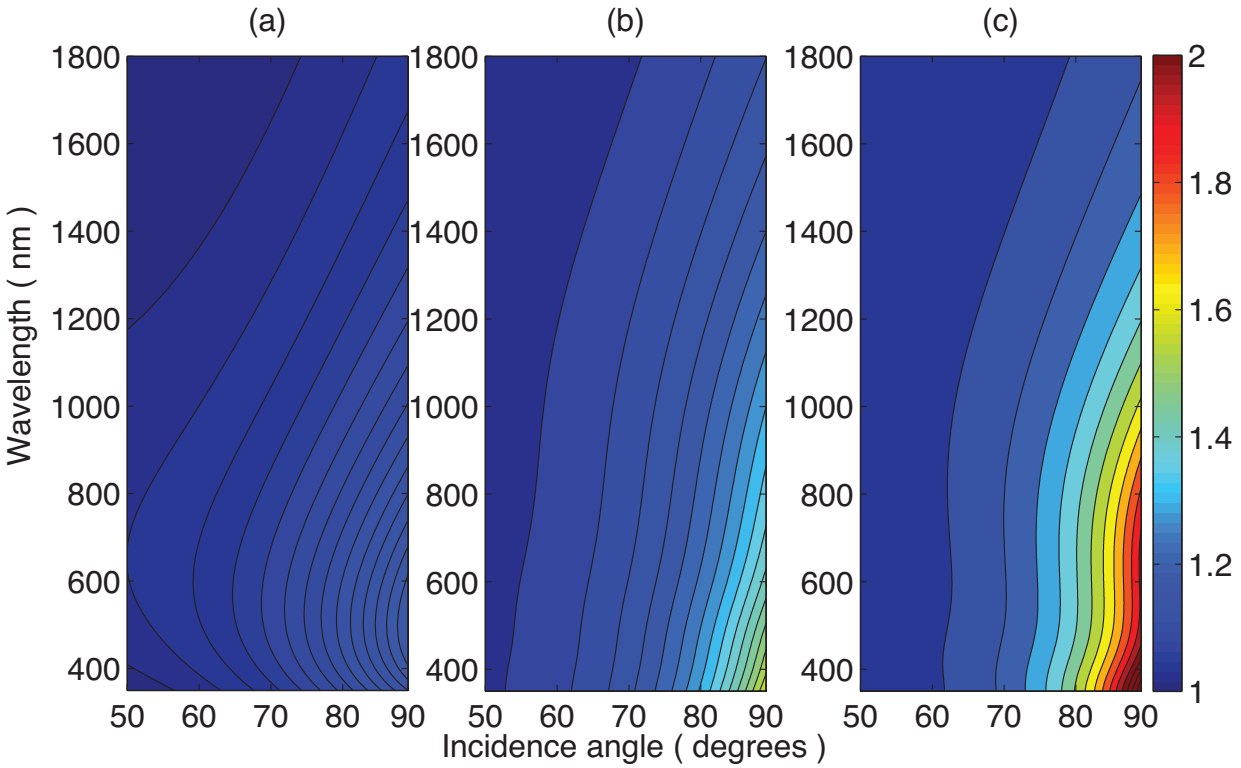

Fig. 2.7 Contours of $\frac{T(\lambda,\theta)}{T_{\mathrm{BARE}}(\lambda,\theta)}$ showing enhancement in transmittance due to the application of (a) quarter-wavelength MgF_2 AR coating, (b) SiO_2 with $500nm$ tall paraboloidal MEAR structures, and (c) SiO_2 with $500nm$ tall conical MEAR structures.

Convolution with the AM0 solar spectrum in each wavelength bin and integration ac-

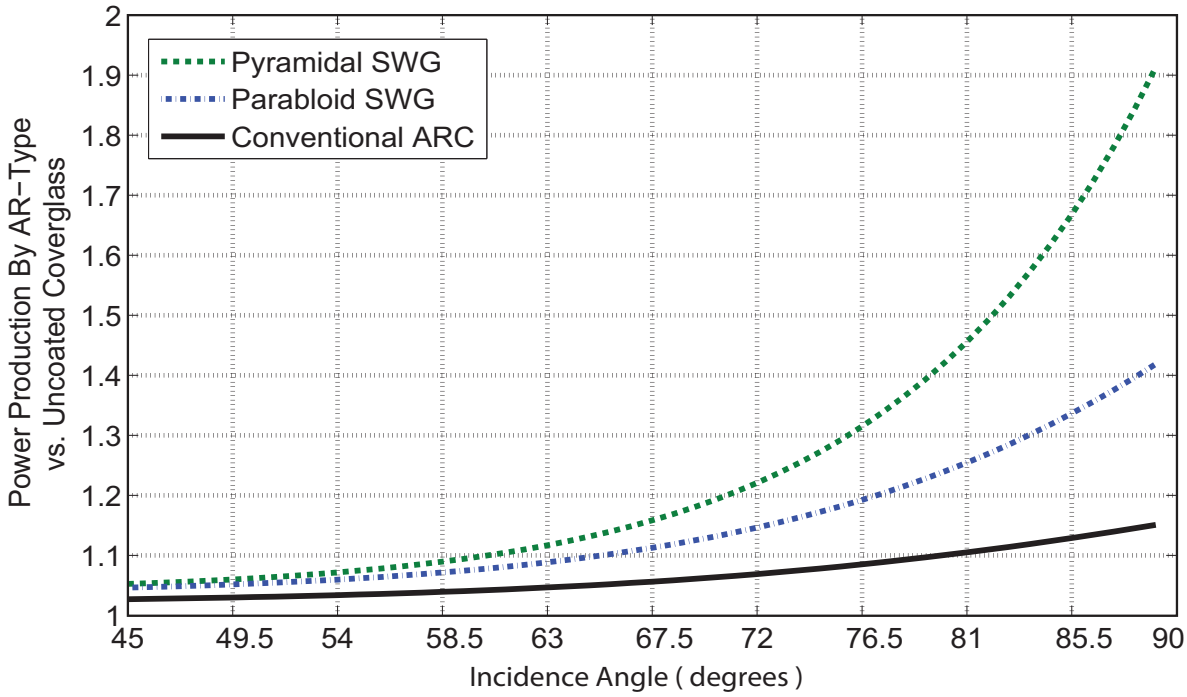

Fig. 2.8 EMT-TMM-computed ratios in peak power-production versus untreated SiO_2 as a function of incidence angle. Paraboloidal and conical MEAR structures are shown, along with the expected performance of a commercial MgF_2 quarter-wavelength coating.

cording to Eq 2.9 yields the expected short circuit current of a solar cell under each type of coverglass at each angle of incidence from 0° to 90°. This data is visualized for angles $> 45°$ in Fig 2.8 in which it is apparent that the conical MEAR structure outperforms the paraboloidal structure by a wide margin at high angles of incidence. MEAR enhancement is uniform at angles of incidence from 0° to 45°, and both MEAR structures exhibit nearly identical performance in this range. The figure also shows both MEAR structures begin to greatly outperform the commercial MgF_2 coating at high angles of incidence. The curves

displayed in Fig 2.8 are crucial tools for analyzing the impact of MEAR structures on a nanosatellite mission.

Using the data from Fig 2.8 it is possible to analyze the impact of MEAR application to commercial coverglass for a typical CubeSat mission by propagating the enhanced power-production curves, $P(\theta)$, through simulated attitude and orbit data for a given configuration of solar panels. A 3-U CubeSat with the body-axis frame, $\underset{\rightarrow}{\mathbf{F}}_B^T$, is assumed to have solar panels mounted on all sides of the satellite, and the surface normals are aligned with the bases of the body-axis frame: $\underset{\rightarrow}{\mathbf{F}}_{B_1}^T$, $\underset{\rightarrow}{\mathbf{F}}_{B_2}^T$, and $\underset{\rightarrow}{\mathbf{F}}_{B_3}^T$. The power produced at any point throughout the orbit may be described using the apparent position of the sun as a vector in the body frame $\underset{\rightarrow}{\mathbf{S}} = \underset{\rightarrow}{\mathbf{F}}_B^T \cdot \mathbf{S}$ where $\underset{\rightarrow}{\mathbf{S}}$ has magnitude in time $|\mathbf{S(t)}|$ given by the piecewise function

$$\|\mathbf{S(t)}\| = \begin{cases} 1; \text{ satellite illuminated,} \\ 0; \text{ satellite in shadow.} \end{cases} \tag{2.11}$$

Using Eq 2.11, the angular-dependent power-production for each side of the satellite in Eq 2.9 becomes time dependent with $\theta(t)$ where

$$\theta_k(t) = \arccos \underset{\rightarrow}{\mathbf{A}}_k \cdot \underset{\rightarrow}{\mathbf{S(t)}}. \tag{2.12}$$

The vector $\underset{\rightarrow}{\mathbf{A}}_k = \underset{\rightarrow}{\mathbf{F}}_B^T \cdot \mathbf{A}_k$ is the surface normal of the k-th solar panel in the body frame. Since the total power over orbit is directly related to the short circuit current over orbit, then the increase in power-production due to MEAR application over an entire orbit may

be computed simply by

$$P' = \frac{I_{MEAR}}{I_{BARE}}. \tag{2.13}$$

Here the subscripts correspond to the particular transmittance function used in Eq 2.9 and the total amount of power generated over time $0 < t < \tau$ will be proportional to

$$I = \sum_{k=1}^{6} \int_{0}^{\tau} I_{\mathrm{SC}}(\theta_k) \cdot \|\mathbf{S(t)}\| dt. \tag{2.14}$$

Following this procedure, and using the data shown in Fig 2.8 the expected increase in power-production over orbit was investigated for a 3-U CubeSat in LEO over a variety of different orbits. The CubeSat was assumed to have body mounted solar cells fully covering each side of the satellite which is a marginally unrealistic configuration for a 3-U CubeSat in which, typically, one of the 1-U sized panels would house the aperture for an instrument. One week of attitude data was generated for satellites in circular orbits with altitude of $650km$ at inclinations ranging from $0°$ to $100°$ in increments of $5°$. It was assumed that the satellite was constantly oriented in the nadir configuration with the long-axis aligned with the nadir.

The results of propagating the relative transmittance of paraboloidal-MEAR-enhanced, conical-MEAR-enhanced, and MgF_2-enhanced coverglasses are shown in Fig 2.9, the results

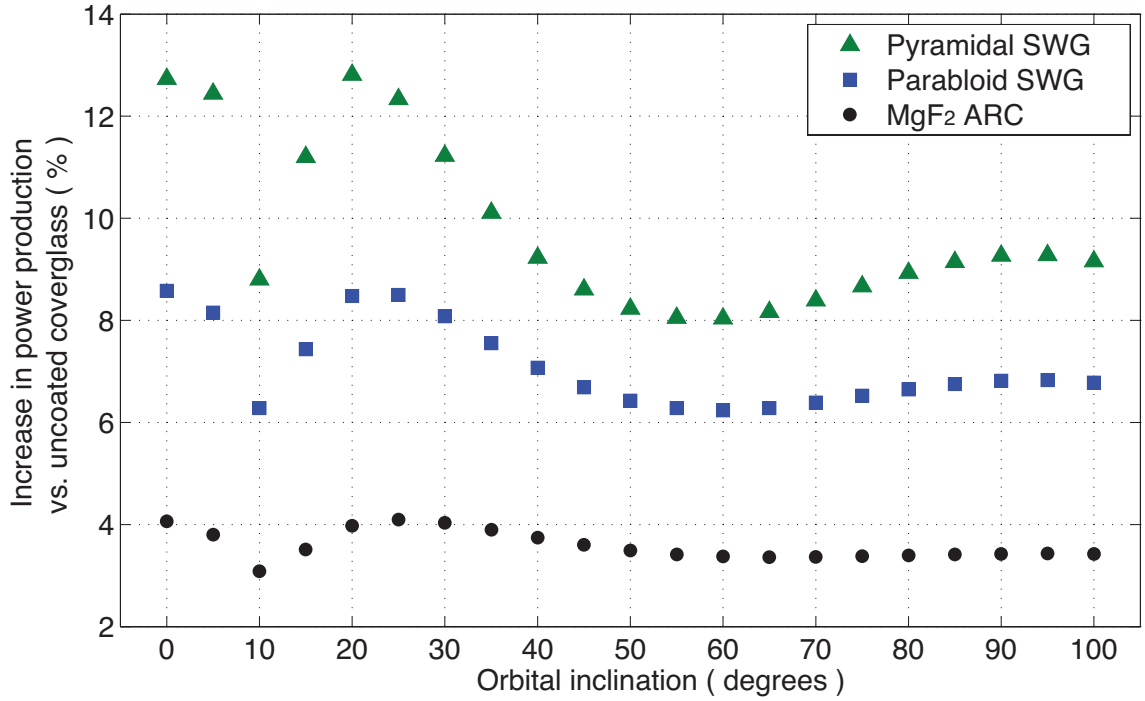

Fig. 2.9 EMT-TMM-computed ratios of peak power-production over orbit versus untreated SiO_2 as a function of orbital inclination. Ratios were computed for conical and paraboloidal MEAR structures $500nm$ tall, as well as a commercial MgF_2 coating.

of the TMM simulation indicate that the application of MEAR surfaces to SiO_2 coverglass will increase the amount of power generated over orbit to 7% above the amount generated under bare coverglass. This stands in contrast to the 3% increase in power-production afforded by MgF_2-coated coverglass. In summary, then, EMT-TMM predicts that the MEAR-effect of paraboloidal structures at $h = 500nm$ is expected to produce a 7% power increase over untreated glass and a 4% increase in power over orbit versus a standard quarter-wavelength coating.

EMT-TMM simulations showed that the transmittance of the MEAR structure was monotonically increasing with feature height, but with significantly diminishing returns at feature heights higher than $500nm$. Unfortunately current state-of-the-art fabrication techniques for realizing MEAR structures on SiO_2 have been unable to produce structures with aspect-ratios greater than 5:1. This is primarily a consequence of poor mask-to-substrate selectivity between selected etch masks and SiO_2. This implies that $500nm$ tall MEAR structures would have a minimum pitch of $100nm$. While grating pitch of $100nm$ does weakly satisfy the subwavelength constraint to justify the use of EMT-TMM it is unlikely that fabricated structures will meet this requirement, therefore the expected performance of MEAR structures must be verified by RCWA calculations.

Generally speaking, RCWA methods are expected to be more exact than EMT-TMM, however, care must still be taken to avoid mathematical artefacts in numerically simulated results. In 3D-RCWAs there are a greater number of convergence criteria in order to be confident of the results. It is determined that discretizing the staircase approximation into 14 horizontally arranged strata and 1000 vertically stacked layers yields convergent while maintaining computational efficiency. Rather than discard all diffracted orders above the 0th, as in EMT-TMM, diffracted orders up to the fourth diffracted order are considered; again, the fourth order was found to balance converging results against computational efficiency.

The use of the fourth diffracted order is not an indication that the SWG criterion does not hold, *per se*. Reassuringly, the computed values of transmittance were less sensitive to diffraction order than they were to the staircase approximation by orders of magnitude; this implies that the sub-wavelength condition holds. RCWA calculations are used to calculate the transmittance directly into the $GaInP$ top cell assuming that the TASC cell has been coated with a MgF_2/ZnS double layer antireflection coating; as in the case of EMT-TMM the transmittance is calculated for MEAR enhanced coverglass, bare glass and MgF_2 coated glass.

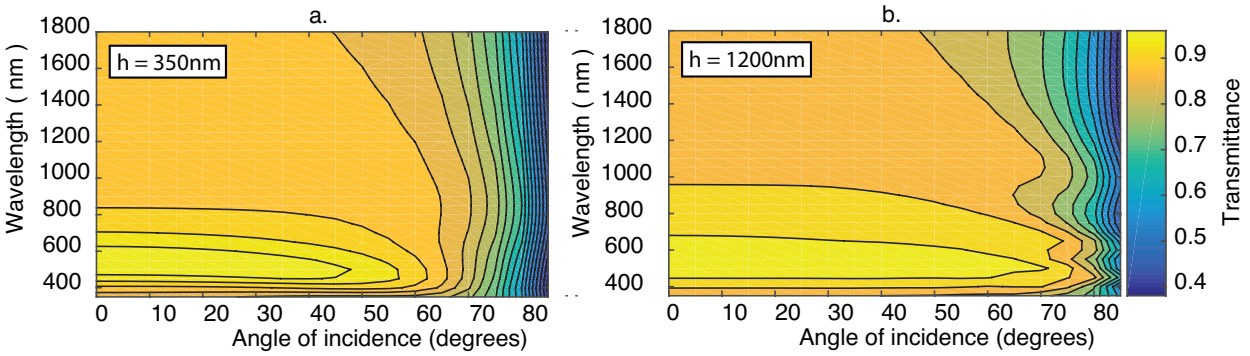

Fig. 2.10 RCWA-computed contours of the transmission of MEAR-enhanced glass relative to uncoated glass for MEAR structures shown in Fig 2.5. $350nm$ tall MEAR structures produced the contour in (a), while $1200nm$ tall structures produce the contour shown in (b).

An example of a moth-eye grating used for RCWA calculation is shown in figure 2.5. Calculated transmittance values for this grating structure at two different heights are shown

as a contour plot in Fig 2.10. As has been discussed previously, the height of the grating is a strong determinant of the overall reflectance; and the effect of this parameter must be considered beyond merely meeting the criteria for total interference at the primary interface ($h > \lambda_{max}/4$)). The effect of varying the height of MEAR structures as a function of wavelength is shown in Fig 2.11; this effect is also apparent in Fig 2.10. Increasing the height of MEAR structures, while keeping the criterion for destructive interference of reflected components has the effect of pushing the reflectance minima at $\lambda = \frac{5}{2}\lambda$ to longer wavelengths, as well as introducing new minima at shorter wavelengths [9, 13, 16]. Varying the structure height serves to control the position of transmittance maxima, hence this parameter should be optimized in order to produce maximal transmittance. In Fig 2.12a a low-resolution one-dimensional maximization routine was carried out to determine the optimal height of a MEAR structure for the space environment. The coarse optimization indicated that optimal MEAR height would occur between $1150nm$ and $1250nm$, and a second higher resolution search (Fig 2.12b) was carried out in this region. The optimization seeks to maximize the total power produced by the cell, P at normal incidence only, and the grating period for this routine is fixed at $130nm$ which is the approximate limit of the subwavelength criterion. The high-resolution optimization was fit to a second-degree polynomial and the maxima was determined to be $1204nm$ with a fitting uncertainty of $\pm 15nm$. Subsequent analysis revealed that MEAR structures with periods $\Lambda < 130nm$ showed inferior performance, indicating that a MEAR structure with $h = 1200nm$ and $\Lambda = 130nm$ is the ideal structure–given our

assumptions–for maximizing power-production on CubeSats.

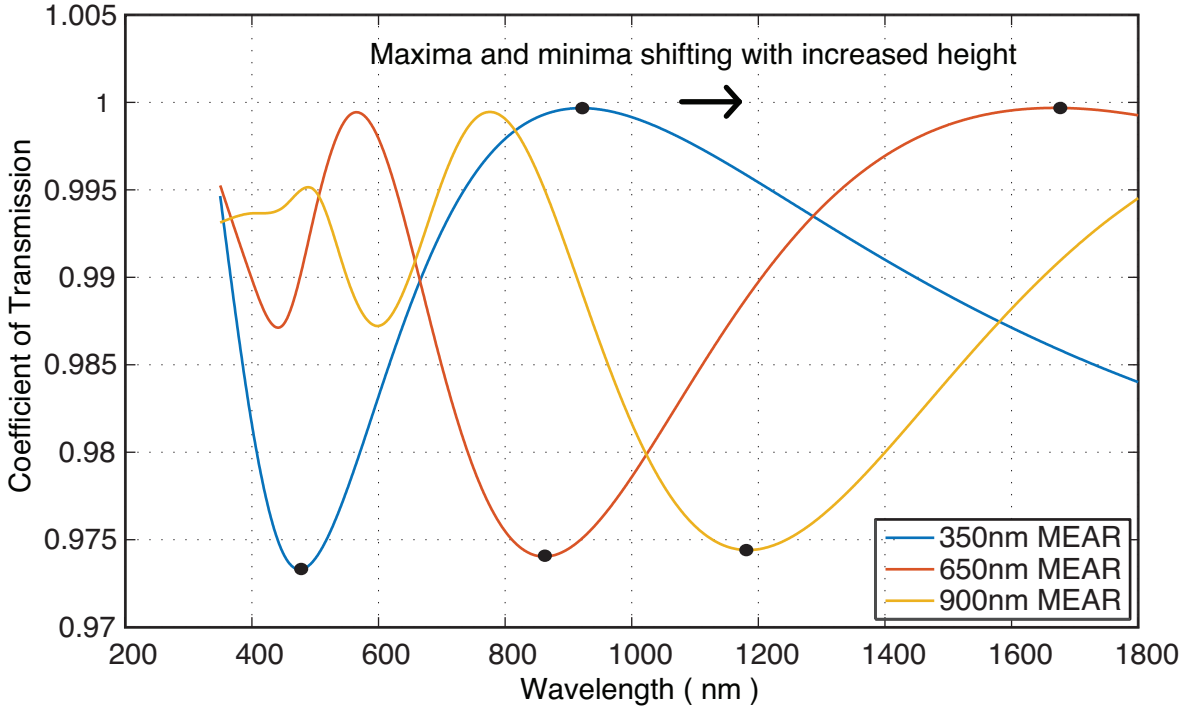

Fig. 2.11 Plot showing the transmittance of MEAR surface as a function of wavelength at normal incidence, transmittance maxima and minima are shown to move as the MEAR structure height is increased. Three different MEAR structure heights are shown: $350nm$, $650nm$ and $900nm$.

A note on the assumptions and constraints of the optimization routine. The first constraint is that only the transmittance at normal incidence was considered as a heuristic; this constraint was implemented for reasons of computational efficiency. RCWA is a much more computationally intensive simulation routine than EMT-TMM and it is not reasonable to

run an optimization routine which requires the use of the full 2D contour plots shown in Fig 2.10 and Fig 2.7. If the full-surface were used, each iteration in the optimization routine would require multiple weeks' computation time. Instead, the total transmittance at normal incidence convolved with the EQE of the TASC cells, and the solar spectrum is used as a substitute. This motivation behind this substitution is that for a given grating pitch the optimal height at normal incidence is unlikely to produce significantly sub-optimal results at high angles of incidence. Furthermore, it is standard mission design practice to configure the resting attitude of a CubeSat to minimize angles of incidence. Optimizing the performance at normal incidence is therefore expected to result in ideal performance during standby and station-keeping operations while still providing significant improvement at times of high incidence. The second constraint applies to the grating pitch; originally the RCWA routine was implemented as a two dimensional minimization in both pitch and height. Implemented as a 2D search, the optimization routine quickly converged at the maximum allowable grating pitch $\Lambda = 130nm$ and from that point on followed a purely one-dimensional search. The routine was only considering normal transmittance for the reasons stated above, however the subwavelength criterion is much weaker at normal incidence than at oblique incidence. It is certain that the optimal grating pitch for enhanced transmission at normal incidence is greater than $130nm$, however at higher angles of incidence grating pitch greater than $130nm$ will reduce overall transmission as the subwavelength criterion is broken. Therefore an upper constraint of $\Lambda = 130nm$ is applied to the MEAR pitch in order to ensure that

the requirements of subwavelength operation under oblique incidence are met. A computationally efficient optimization routine which uses EMT-TMM formulation as a coarse-grid optimization tool, followed by RCWA for fine-grid minimization has been demonstrated to lead to an optimal MEAR structure in a reasonable time-frame. Unfortunately the mixed EMT-TMM approach cannot be employed here as the subwavelength criterion is not strongly satisfied, hence a breakdown in the EMT-TMM formulation would be expected similar to what was observed by Foberich *et al.* [24].

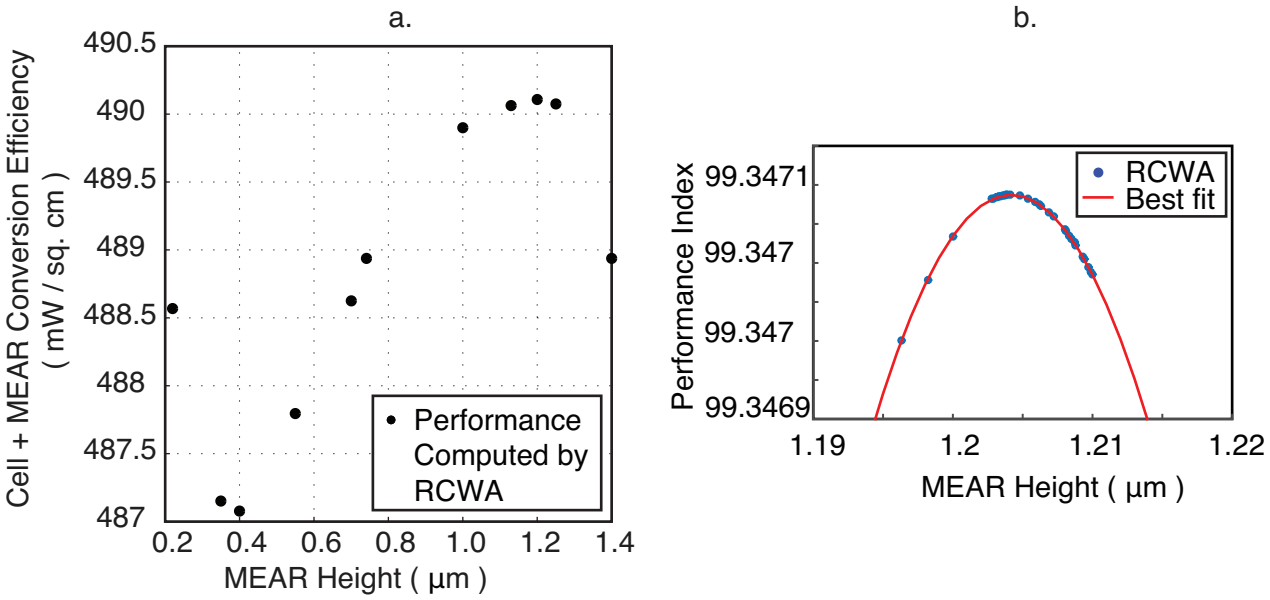

Fig. 2.12 High-resolution and low-resolution RCWA optimization routines for a 1D search of MEAR height with pitch fixed at $\Lambda = 130nm$. The high resolution optimization yielded a maxima of $1240.1nm$ with a three-sigma uncertainty of $\pm 15.1nm$.

Following the optimization routine the transmittance and reflectance of optimal MEAR structures is calculated by RCWA, and the results are propagated through the same orbital dataset as was explored in Fig 2.9. The results of this simulation demonstrate that an optimal MEAR structure with height $h = 1204nm$ and pitch $\Lambda = 130nm$ is expected to demonstrate a mean improvement in power over orbit of 7%. The improvement in power from the optimal RCWA structure is equivalent to those predicted by EMT-TMM for a paraboloidal MEAR structure with comparatively lower height. This discrepancy may be accounted for by the difference in geometry between RCWA simulations and EMT-TMM. The MEAR structure geometry used in RCWA simulations is presented in Fig 2.5 and features a cylindrical structure with a parabolic cap; this structure was selected for its resemblance to the observed geometry of fabricated MEAR surfaces and is expected to demonstrate a less effective taper in refractive index than both the parabolic and conical MEAR structures. In addition, EMT-TMM does not account for feature-spacing, rather it assumes that all structures are strictly subwavelength; RCWA structures spaced at $130nm$ likely see greater loss than structures with arbitrarily small pitch. Despite these differences, the RCWA computations are strongly preferred and are more likely to give a more realistic picture of on-orbit MEAR performance.

Simulated MEAR structures through both EMT-TMM and RCWA methods have been shown to outperform standard MgF_2 coatings across the board; the increase in power-production over orbit for paraboloidal MEAR structures with $h = 500nm$ is expected to

be 7% over bare coverglass, while RCWA predicts a mean 7% increase in power-production for MEAR structures with $h = 1204nm$ and $\Lambda = 130nm$. If borne out by experimental data, these results would have broad implications for CubeSat power budgets; solar cells are already a highly optimized technology, so much so that at this point a 1% increase in the base cell efficiency (typically 28%) would be a valuable result. Conversely, MEAR enhancement of the power budget by 7% is equivalent to raising the base efficiency from 28% to 30%. In the case of MEAR enhancement versus conventional AR techniques, the effect is equivalent to going from 28% to 29.5%; a smaller gain but still a valuable improvement. Finally, it is worth reiterating that MEAR or SWAR enhancement of the coverglass is a passive, non-invasive, mass-neutral and volume-neutral method for increasing the amount of power generated by solar cells. CubeSats, nanosatellites, and microsatellites all already fly solar panels with coverglass layers in order to protect cells from UV and radiation damage; in other words, the application of MEAR technology is expected to increase power-production of CubeSats without requiring the addition of any new components.

3 Moth-Eye Fabrication

In the previous chapter an optimized design for a moth-eye antireflective surface for a triple-junction solar cell on a CubeSat was found to possess an array pitch of $130nm$ and feature height of $1204nm$. The feature profile for these structures is a cylinder with a rounded tip as shown in Fig 2.5; this profile is chosen for its resemblance to fabricated structures and is not an optimized profile. This surface should evenly and completely cover the outward facing surface of the coverglass layer such that the moth-eye structures produce a graded transition between the vacuum of space and the bulk material of the coverglass. Ideally, this surface should be defect-free, resilient to repeated and rapid thermal cycling and resistant to the atomic oxygen environment of LEO. This chapter details the various methods for fabrication of MEAR and SWAR surfaces for ground applications and further explore those methods which are suitable for space applications.

3.1 Introduction to Nanofabrication

The fundamental geometric constraint of MEAR and SWAR surfaces is that the pitch, or the spacing between the individual surface structures, Λ, must satisfy the subwavelength condition $\Lambda < \lambda_{min}/2n$ [9]. In any optical application then, full realization of a MEAR surface will require repeatable fabrication of features at the nanometer scale and hence a nanofabrication approach will be required. Thankfully, MEAR surfaces are geometrically and structurally well-suited to realization through existing nanofabrication methods.

Nanofabricated structures, like MEAR or SWAR structures, are typically created either by depositing new material onto a surface, or by removing material from a surface in order to produce structures in relief; in either case, the resultant widgets are anchored to a particular surface or substrate. It is uncommon to fabricate widgets on the nanometer scale in the absence of this supporting substrate due to the inherent challenges in fabricating components at this size as well as the difficulty in handling those components. Notable exceptions to this rule include nanoparticles and nanowires, both of which may be easily stored in an aqueous solution.

It is reasonable to classify nanofabrication techniques into two broad groups. In the first group are surface micromachining techniques in which additional material or components are deposited onto the surface of a bulk substrate. This set of techniques is also referred to as "bottom-up" manufacturing, since the formation of each structure begins at the base

and proceeds upwards until the top of the structure is reached and deposition ceases. The second type of fabrication techniques create structures by removing material from a substrate. Typically a protective mask is placed on the face of the substrate, and the substrate and mask are both exposed to an etchant which removes any exposed bulk material to produce structures in relief. Fabrication by the removal of the bulk material, sometimes called bulk micromachining is referred to in this thesis as "top-down" manufacturing. Thus the broad categories for nanofabrication processes are: surface, or bottom-up techniques; and bulk, or top-down methods [29].

In reality, fabrication processes will employ a combination of these two techniques. For example, the use of an etching mask during any top-down process implies that at some point the masking material was deposited on the surface of the substrate. "Top-down" and "bottom-up" monikers are therefore used hereafter to refer to the composition of the final structure of interest: if the structure was present in the bulk material before the start of the fabrication process then the overall process was top-down, if the relevant structure was added to the bulk material at some point during the process then the overall process shall be considered to be bottom-up.

There are various advantages and disadvantages associated with each approach. In particular, due to the strength of the underlying crystal lattice, structures formed by top-down fabrication are expected to exhibit greater tensile strength than structures with the same chemical composition formed by the deposition of new material. Structures formed from the

bulk material are also expected to experience less thermal strain due to expansion-coefficient mismatch. Top-down processes yield systems in which the substrate and the exposed structures are part of the same lattice; hence their expansion-coefficients will be well-aligned in both direction and magnitude.

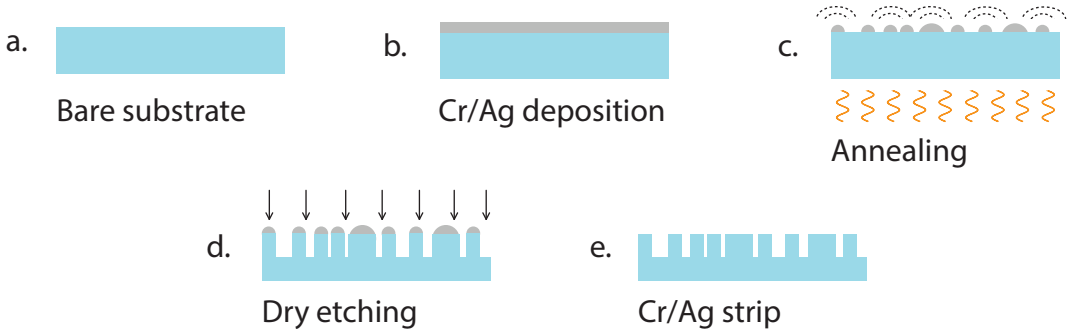

Fig. 3.1 Cross section diagram of a top-down process carried out an arbitrary substrate. Beginning with a bare substrate (a): a chromium etch mask is deposited onto the surface by electron-beam evaporation (b), then annealing the substrate then results in the agglomeration of the thin film and the formation of nano-islands (c). Following nano-island formation a dry-etch is performed to produce structure (d) after which any remaining masking material is stripped away using a "Piranha" (H_2SO_4/H_2O_2) or HF solution (e).

Bottom-up processes, however, are generally preferred in part due to their lower cost and scalability; in the specific case of MEAR surfaces, nanoimprint lithography (NIL)–a bottom-up process–has been demonstrated to produce high-quality, large-area MEAR structures with excellent repeatability [30–32]. NIL techniques, however, are not well suited to the space environment as they employ curable photoresists to build nanostructures, and

these resists are not robust to the atomic-oxygen (AO) environment in LEO [33–35]. A number of techniques also exist for nanopillar growth however these techniques typically require particular nanopillar chemistries which are not suitable for reducing reflectance at the vacuum-glass interface [36, 37].

For the purpose of producing a MEAR surface for the space environment, then, top-down processes are preferred due to their inherently greater robustness as well as their favourable chemistry with respect to atomic oxygen bombardment. In this case the substrate used for nanofabrication is merely the coverglass that will be bonded to the solar cells before space flight; all that remains then is to determine a top-down process for fabricating MEAR structures on a coverglass substrate.

A typical top-down fabrication process will first involve the deposition of a masking layer. The mask layer may be composed of metals such as nickel, silver, gold, chromium *etc.* or for photolithographic processes the masking layer may be composed of poly-methylmethacrylate (PMMA), polymide resist or some other plastic; holes in the mask layer may then be defined using electron-beam lithography, laser etching, annealing, UV lithography or a variety of other techniques [38, 39]. Once the mask layer has been deposited, and gaps in the mask have been introduced an etch process is carried out to remove material from the substrate at sites exposed by gaps in the mask layer. Etch processes are typically tuned for their selectivity in etching the substrate over the mask layer as well as their "anisotropy", a term which refers to the directionality of the etch process. A schematic diagram of a simple top-down

process consisting of deposition, annealing, etching and stripping steps is shown in figure 3.1.

The small feature size and the desired chemical composition of MEAR structures further restrict the available fabrication approaches: the minimum possible feature size achievable with UV lithography is just now approaching the subwavelength limit as defined in Chapter 2.2. This is hardly unexpected as UV lithography uses intense ultraviolet light to resolve and define features, but subwavelength features are smaller than light to begin with! Furthermore as the aspect-ratio required for these small features is quite high–approximately 9:1 for the optimized MEAR structure–any highly isotropic etch process, such as wet-etching, must be summarily eliminated. All together these restrictions leave only dry-etching techniques as the remaining candidates for MEAR fabrication; these techniques are reactive-ion etching (RIE), inductively coupled plasma (ICP) etching and deep reactive-ion etching (DRIE).

RIE, ICP and DRIE techniques are functionally similar etching techniques based on the excitation of gas in a chamber to a plasma state by the use of radio frequency (RF) generators, the two most popular configurations: traditional capacitively-coupled plasma (CCP) and ICP are shown schematically in Fig 3.2. In an RIE process the substrate is placed in an evacuated chamber which is then filled with a gaseous mixture that is tightly regulated in both its stoichiometry and pressure. Once the chamber has been filled an RF electromagnetic field is applied to the platen on which the substrate is mounted; the RF field excites the gas near to the platen, dissociating electrons from their parent molecules

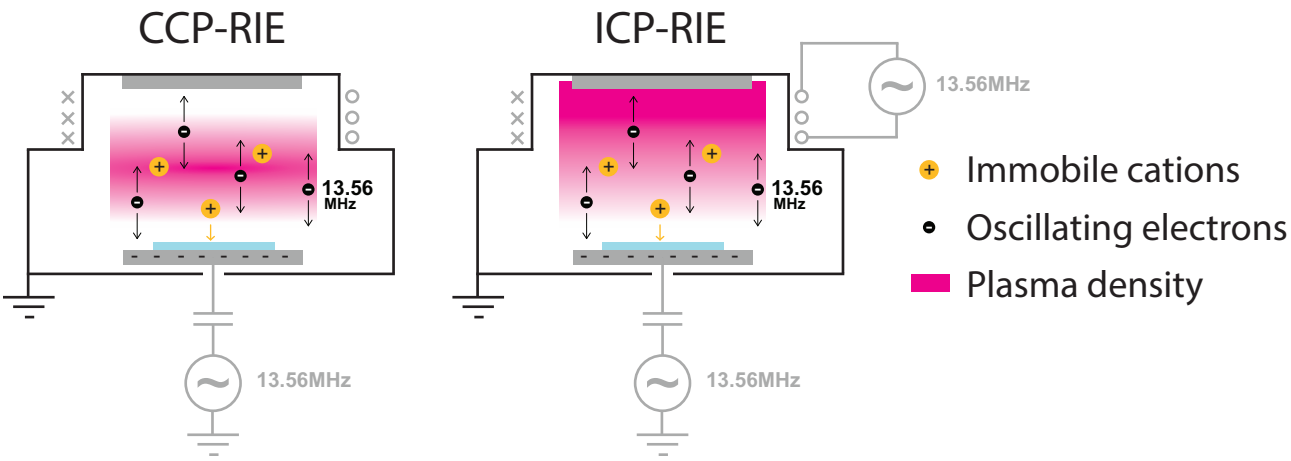

Fig. 3.2 Schematic of plasma formation mechanisms and chamber configurations for a CCP-RIE system and ICP-RIE system. Oscillating electrons (black) strike the electrically isolated platen (grey, bottom) building up a steady-state bias voltage that accelerates positively charged ions (yellow) onto the substrate.

and allowing the electrons to be propelled throughout the chamber according to the field generated by the RF source. The heavier positively charged ions are stable with respect to the RF field due to their relatively large mass, however as the mobile electrons strike the platen and substrate a negative electric charge will build up at the platen which will accelerate the positively charged ions towards the substrate. As these ions reach the surface they will remove material at the substrate in accordance with the chemistry of the reaction. Tuning the power applied to the RF source will increase or decrease the amount of negative charge that is able to build up at the surface of the substrate–the bias–and hence will control the bombardment energy of the incoming ions. Increasing the RF power applied during an RIE etch will control both the etch rate as well as the anisotropy of an etch,

as more energetic ions will be more likely to react with the surface and will also be more likely to arrive at normal incidence. Care must be taken during an RIE process, however, to ensure that the bombarding ions do not become so energetic as to etch the surface through physical sputtering as this will reduce the etch selectivity between the substrate and mask layer [40, 41]. In Fig 3.2 the plasma density is represented by a gradient showing the main regions in which plasma formation is excited. The high-density plasma region is truncated by the onset of ion-bombardment which removes cations that are $< 1cm$ from the surface of the substrate. Cations such as $CF_3^+, CF_2^+, CHF_2^+, CHF^+$, and O^+ are depicted in yellow, while electrons excited by the RF field are depicted as smaller black particles.

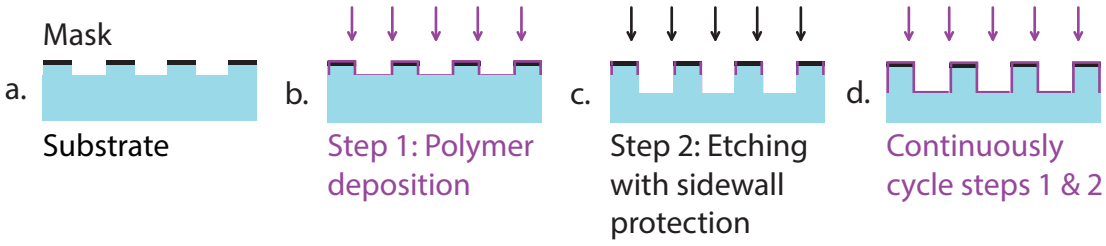

Fig. 3.3 Cross sectional diagram of a simple Bosch-based DRIE process. First the etch-mask is defined (a), then a thin polymer-layer is deposited uniformly over the substrate (b) before a traditional etch step is carried out in order to remove substrate material (c). During the etch, the sidewalls are protected from chemical etching, producing a highly anisotropic etch. This process is continuously cycled until the desired etch depth has been achieved (e).

ICP and DRIE etch processes are similar to the RIE method described above. The primary difference is that in an ICP etch the ion density and energy will be raised by the

application of a second RF source at the top of the chamber, which further excites the gas using a large induction coil to generate an intense, oscillating magnetic field. An electric field is still required to accelerate ions towards the surface of the substrate, hence ICP is often referred to as "ICP-RIE". In Fig 3.2 an RIE chamber configured for ICP is shown on the right. DRIE is a specific set of ICP-RIE techniques used to produce very high aspect-ratio structures; the most common form of DRIE is the patented Bosch process in which the etch process cycles between two alternating etch recipes. The first of these cycles is a traditional etch process similar to the RIE process described in the paragraph above and the second cycle is a "passivation" cycle in which an extremely thin fluorocarbon layer is deposited onto the substrate in order to protect the side-walls from chemical etching. This process is shown diagrammatically in Fig 3.3.

3.2 Colloidal Lithography

MEAR surfaces have a distinct hexagonal arrangement pattern and as such the ideal etch mask will be required to replicate this pattern [42]. As discussed in the introduction, a typical method for fabrication of the etch mask may involve UV lithography or electron beam lithography (EBL), however these two approaches have significant drawbacks which make them unsuitable for use in MEAR fabrication. In the case of UV lithography, the resolution at the nanometer scale is not sufficient for the fabrication of a mask for MEAR surfaces, and in the case of EBL the lengthy beam write-time required to cover the surface area of

even a very small solar cell would make the fabrication of MEAR structures prohibitively expensive [43]. It is necessary to develop an assembly technique that is capable of producing an even mask layer with a repeating, nanoscale hexagonal pattern over a total surface area of up to $5cm^2$. Furthermore, to encourage adoption by CubeSat developers this assembly method should be straightforward and inexpensive. Two mask assembly methods meet these criteria: deposition and annealing of a thin metallic film as shown in Fig 3.1, and a "colloidal lithography" approach in which the mask is composed of a monolayer of self-assembled nanoparticles dispersed from commercially available solutions of nanoparticles, ethanol and water.

To assemble the mask layer using a thin-film annealing approach first the sample would be sputter coated with a thin (tens of nanometers) metallic film, typically composed of nickel, silver or chromium. The sample would then undergo an annealing step in which the temperature of the sample and the thin film is raised above the melting point of the thin film layer; this annealing step will cause the thin film to agglomerate in a semi-randomized pattern forming metal "islands" with some size distribution that is controlled by the temperature and duration of the annealing step [11]. The advantages of this approach are that the available masking materials are known to have very good etch-selectivity when compared with SiO_2, hence, an etch mask assembled using a thin-film anneal will be able to produce MEAR structures with very high aspect-ratios. In addition, thin-film annealing is a well-understood

and very simple process that is common to many microfabrication facilities and does not require extensive training. Thin-film annealing, however, does not produce an even hexagonally spaced array, and the level of control over the MEAR spacing–the critical parameter–is reduced; furthermore, the use of a metallic etch-mask requires additional post-processing to remove the mask material. In the case of metallic masks this post-processing will require a potentially hazardous wet-etching step using an H_2SO_4/H_2O_2 (Piranha) solution. A safer and more repeatable alternative is preferred.

Colloidal lithography, shown diagrammatically in Fig 3.4 involves the preparation of a mask layer by the deposition and arrangement of nanoparticles or nanospheres on the surface of a substrate, either by spin-coating or through Langmuir-Blodgett (LB) techniques [44,45]. The primary advantage to this approach is that nanoparticles, which are small particles with diameters between 1-1000nm naturally self-assemble in a hexagonal array, allowing for the formation of even mask layers over large surfaces [43, 44, 46, 47]. This allows for cheap fabrication of large, periodic structures with feature resolution as low as tens of nanometers. Colloidal lithography has long been used to fabricate photonic crystals, which require evenly spaced structures on the nanometer scale, for these very reasons. Colloidal lithography techniques typically employ organic colloids prepared from poly-methylmethacrylate (PMMA) or polystyrene (PS). Despite the volatility of these compounds relative to metal etch-masks, PMMA and PS have been demonstrated to provide an etch selectivity sufficient for the fabrication of optical MEAR surfaces [12,16]. In addition to their suitability for the production

of MEAR surfaces it is possible to use a short dry-etch step with O_2 to tune the size of PMMA and PS particles or even remove them altogether, eliminating the need for post-processing of the substrate [43,48]. Like thin-film deposition the procedures for spin-coating and LB-deposition are well established in the literature [49–51], and can be performed with relatively little training. Spin-coating stations are a staple of the modern microfabrication facility, and the equipment required for basic LB-deposition can be purchased cheaply from major science supply stores such as Fisher, Sigma-Aldrich or Cole-Parmer [43, 44]. The primary drawback of colloidal lithography is that the etch selectivity of nanoparticles to SiO_2 is limited when compared to metallic masks. In fact selectivity greater than 5:1 on SiO_2 has yet to be demonstrated using this technique and as such only low to medium aspect-ratio MEAR structures may be fabricated.

The merits of each technique were evaluated and it was determined that for the purposes of MEAR fabrication for CubeSats, the trifold advantages of user safety, natural hexagonal arrangement over large areas, and lower cost outweighed the poor etch selectivity as compared with a metallic mask produced through thin-film annealing. Within the domain of colloidal lithography techniques it was determined that a lift-off procedure using LB techniques was preferable to spin-coating due to the greater surface coverage achievable through LB [43]. LB techniques were also preferred for their low cost and their simplicity.

Mask preparation through LB deposition is presented diagrammatically in Fig 3.4. First, a de-ionized water (DI water) bath is prepared with the substrate immersed below the wa-

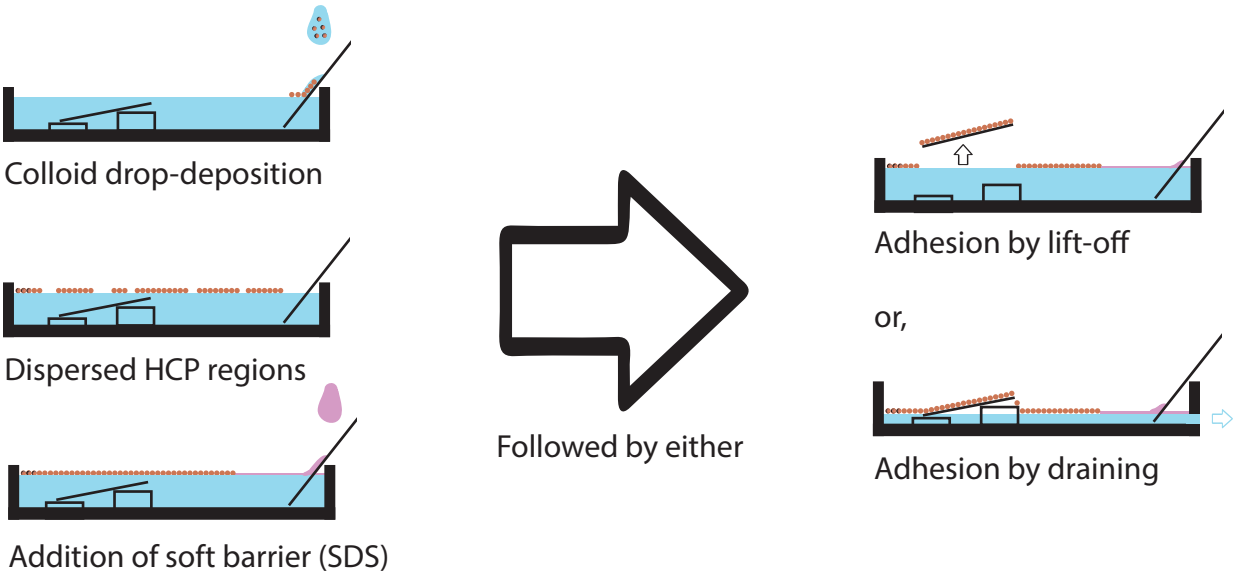

Fig. 3.4 Flow diagram demonstrating the nanoparticle deposition processes used to assemble etch-mask layers.

terline, then colloids are introduced to the liquid air interface by drop deposition onto a partially immersed slide that is tilted at 45° away from the water surface. The nanoparticles naturally self-assemble at the liquid-air interface into domains of hexagonally close-packed (HCP) monolayer arrays, and full surface coverage may be achieved through careful tuning of the drop deposition process [49, 52]. Following the introduction of colloids to the DI water bath the nanoparticles at the surface are compressed by the addition of a soft-barrier to the liquid-air interface; the surfactant sodium dodecyl-sulfate (SDS) is used as the soft-barrier, and its addition to the DI water surface acts to increase the surface tension, eliminating residual gaps between separate HCP domains and ensuring that the array is uniformly close-packed [44, 49]. Once the monolayer has formed at the liquid-air interface and SDS has been

added to compress the nanoparticles, the substrate is lifted upwards through the waterline and the monolayer at the surface is transferred to the substrate. The substrate is subsequently left to dry at an inclined angle [52] and the underside of the substrate is cleaned with DI water to remove any residual nanoparticles.

Initially, the liquid to substrate transfer was to occur in reverse. A bath was designed such that the substrate could be placed on a central pedestal, and the waterline lowered by releasing a valve at the bottom of the DI water bath. This procedure is shown diagrammatically in Fig 3.4. This procedure was intended to yield improved repeatability and eliminate human error during the crucial monolayer transfer step. A bath, valve and pedestal system was designed and fabricated, however this procedure was found to yield poor results with lower repeatability than performing the monolayer transfer step by hand. The reasons for the poor performance of this bath are twofold: firstly, unlike work by other groups, the walls of the bath were not made hydrophobic [52], hence when the water level was lowered the nanoparticles near the walls of the bath were attracted to and deposited onto the walls of the container by the same capillary forces that are used in traditional LB deposition techniques. The unwanted deposition of nanoparticles onto the walls of the container reversed any compression of the monolayer by the SDS solution, and often introduced gaps into the monolayer above the substrate itself. Secondly, the bath failed due to poor design of the pedestal: the pedestal was intended to service a number of substrates of various sizes up to and including circular substrates with diameter $50mm$, however it was discovered that

the presence of the pedestal adversely affected deposition of a monolayer onto any smaller substrate. As the waterline descended below the surface of the pedestal runoff was observed whereby monolayers at the center of the pedestal were disturbed by water cascading over the edge of the pedestal, this motion caused nanoparticles to be wicked away from the center of the pedestal where the substrate was located and the resultant monolayers were found to exhibit significant gaps between HCP domains. These problems do not manifest when manual surface-to-substrate transfer is performed and for that reason the pedestal and drain system was abandoned.

A 0.5L Pyrex bath (Fisher Scientific) was partially filled with DI water (MilliQ, resistivity $18.2 MOhm$, $TOC < 5 ppb$) and substrates were fully immersed at the bottom of the bath on a small raised platform to facilitate lift-off. Sterile borosilicate slides were partially immersed at an angle of approximately 45° and were used as a ramp from which dispersed nanoparticles could roll down the slide and directly onto the liquid-air interface. Monodisperse 10% *vol.* nanoparticle solutions of three different sizes ($120nm$, $190nm$ and $600nm$, Magsphere Inc.) were mixed with ethanol at a ratio of 1:1, and the resultant solutions were drop deposited onto the partially immersed borosilicate slides using a bulb-operated $40\mu L$ capillary micropipette. The addition of nanoparticles to the subphase is highly sensitive to slide contact angle, initial drop position and nanoparticle flow rate. Three distinct monolayer assembly regimes were observed to occur depending on the unique combination of these parameters. These regimes are shown diagrammatically in Fig 3.5.

The contact angle between the borosilicate slide and DI water was found to be of crucial importance to the addition of nanoparticles to the subphase: steep contact angles caused nanoparticles to submerge at the bottom of the slide or agglomerate into very small, disperse HCP domains rather than assemble at the surface of the bath, resulting in the waste of nanoparticles as well as poor monolayer formation corresponding to the first regime in Fig 3.5. Conversely, shallow contact angles reduced the incidence of particle submersion, but inhibited the dispersion of particles away from the slide; instead, particles formed a HCP domain almost immediately after encountering the DI water, and this domain was "pushed" away from the slide by the introduction of further nanoparticles. Following this process, illustrated in Fig 3.5 the original HCP domain propagated away from the slide in a linear manner until it encountered the edge of the DI bath, at which point the HCP domain fractured, and the process would then repeat. Ideal monolayer formation was only achieved in the third regime shown in Fig 3.5, in which a balance between the formation of large, immobile domains and small, disperse domains was found. With the borosilicate slide at an angle of 45° the particles were observed to exit the slide at velocities similar to that of the first regime, however rather than forming small distinct HCP domains these particles formed an advancing wavefront which spread to cover the surface of the entire bath as nanoparticles were added to the wavefront in an even fashion. The wavefront was sustained by the constant addition of particles forming a region of high concentration between the edge of the borosilicate slide and the edge of the wavefront; visually this region of high particle concentration manifested as a

billowing of the surface revealing obvious modification of the surface tension. By maintaining an approximate flow-rate of approximately $3\mu L/s$ of nanoparticle/ethanol solution from the micropipette it was possible to sustain this wavefront until the monolayer region achieved near full coverage of the DI water bath.

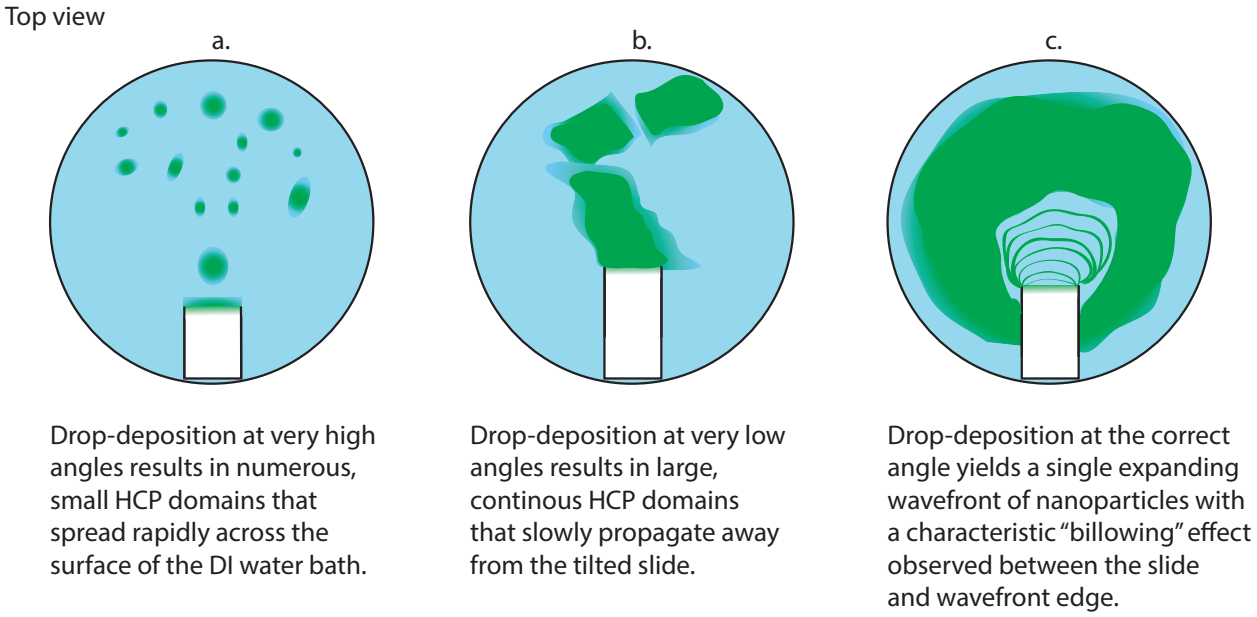

Fig. 3.5 Diagram illustrating the three observed colloid dispersal regimes based on the contact angle of the partially immersed slide used for nanoparticle addition; the diagram shows a birds-eye view of the DI water bath, with the deposition slide adjusted to three different positions.

Following drop deposition of the nanoparticle solution to form a monolayer on the surface of the DI water bath SDS (Fisher Scientific) was drop deposited either onto the borosilicate slide or directly onto the surface of the liquid-air interface. The addition of SDS to the DI water caused surface monolayers to compress and bunch-up away from the SDS, resulting

in a higher quality monolayer with fewer gaps between nanoparticles and greater continuous HCP regions [44, 49, 52]. Once the monolayer had been sufficiently compressed, a pair of angled forceps were used to grasp the substrate and lift it through the liquid-air interface thereby depositing the monolayer onto the surface. The substrates were lifted at an angle to ensure that capillary action would help the monolayer to adhere evenly; after lift-off the substrates were left to dry at an angle of 35° for an hour [52]. Larger nanoparticles such as the $600nm$ diameter particles were used initially in order to practice the drop deposition technique; large nanoparticles are especially useful in this regard because HCP monolayers of large nanoparticles exhibit Bragg scattering allowing for visual identification of HCP regions on the surface of the DI water bath [44]. Using the $600nm$ particles it was possible to identify the visual cues accompanying HCP region formation, such as the billowing effect described above.

A number of factors were found to adversely affect the formation of an even monolayer: the flow rate during drop deposition of nanoparticles, the drying angle of the slides and the steadiness of the lift-off motion were all found to contribute significantly to the formation of an even monolayer. Uneven flow rates during the drop deposition of nanoparticles tended to result in bunching of the monolayer and the formation of multiple high-density regions in which nanoparticles formed a multilayered structure rather than a monolayer array. These multilayered structures were then be transferred to the underlying substrate, resulting in a masking area under which no MEAR structures are able to form. During the drying

a.

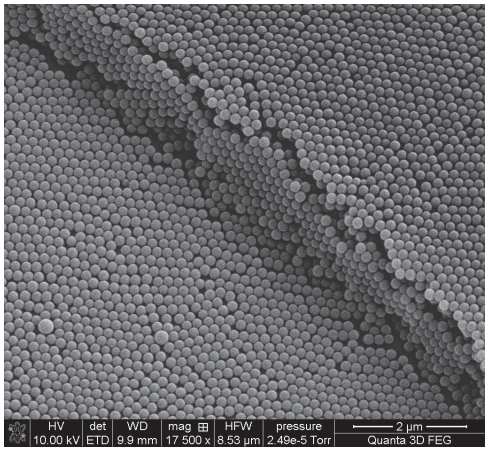

Close-up micrograph of the edge of a multilayered structure formed by evaporation during the drying process.

b.

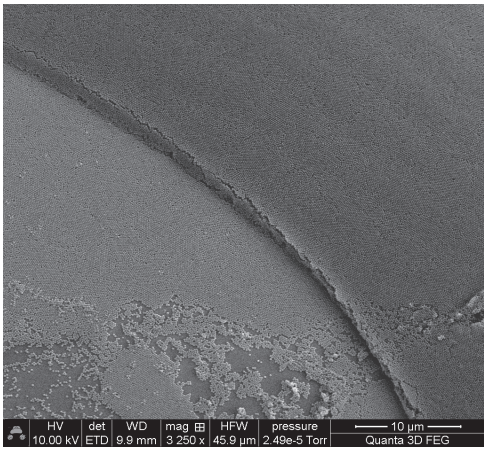

Expanded view showing the extent and and appearance of multilayered structures as well as an uneven area of deposition in the lower left corner of the micrograph.

Fig. 3.6 SEM micrograph showing two common defects due to drying as well as improper deposition. In (a) a close inspection of a multilayered domain is shown and in (b) the expanded view of that same structure. In (b) additional defects such as a poorly-ordered or empty monolayer regions as well as clumped regions may be seen in the lower left corner.

process even monolayer formation was hampered at the lower edge of the tilted slide by the evaporation of residual DI water containing nanoparticles. Streaks and waves of multilayer structures formed at the waterline of DI water droplets and propagated down the slide as the droplets evaporated during the drying process. It was possible to mitigate the formation of these streaks to some extent by increasing the tilt angle during the drying process, however an overcorrection in tilt angle introduced gravitational strain in the monolayer which resulted in the formation of new gaps and cracks in the monolayer. Finally, and most intuitively, the

deposition of an even monolayer was strongly dependent on the smoothness of the motion during the surface-to-substrate transfer of nanoparticles. The nanoparticles were not strongly bound to the substrate during the lift-off procedure and any sharp movements or unwanted vibrations easily led to cracks in the monolayer. SEM micrographs of these defects are shown in Fig 3.6.

For the purposes of this research the defects resulting from the evaporation of residual DI water at the foot of the substrate are inconsequential due to the large size of the substrate relative to the solar cells under testing; the coverglass may be positioned in such a way that these regions are well away from the solar cells themselves, hence these defects are not expected to influence measurements of the transmission of MEAR surfaces. Using this procedure it was possible to achieve full, repeatable, even coverage over $50mm$ by $25mm$ quartz substrates, and work by other groups has indicated that full wafer coverage of even larger substrates is possible [44]. This method could be improved through the use of hydrophilic substrates, which would reduce the contact angle between slide and the DI-water/nanoparticle solution. Reducing this contact angle during the drying process would mitigate the formation of streaks by reducing the amount of vertical space at the waterline, which would inhibit the formation of multilayered regions. Hydrophilic slides would also experience greater amounts of runoff, which would speed-up evaporation by reducing the amount of DI water remaining on the substrate immediately following the lift-off procedure. The deposition process could be further improved by the use of a commercial LB trough

in which the motion during lift-off is automated, which would provide a more repeatable process [44].

Despite these small caveats, the monolayer deposition process was shown to be an effective method for producing large scale, even monolayers in an HCP configuration; furthermore the process was inexpensive and relatively straightforward requiring neither training in advance nor prior experience with LB techniques. These factors make this deposition method a highly favourable approach for MEAR structure fabrication for the space environment, as the typical CubeSat engineer works on a limited budget and does not have the resources to employ experts in microfabrication or thin-film deposition techniques. None of the supplies used to fabricate this mask are subject to stringent import-export regulation, and the quality of the monolayer produced is sufficient for the purposes of both SWAR and MEAR fabrication as shall be shown later in the chapter.

3.3 Reactive Ion Etching

Reactive-ion etching was performed in 3 steps, as shown in Fig 3.7. In the first step, the mask layer which is composed of a monolayer of polystyrene nanoparticles, is modified by a short RIE step in a pure-oxygen plasma. During this step the size of the particles is reduced and the gaps in the mask layer are widened in order to facilitate etching of the SiO_2 substrate during the second step in the overall fabrication process. The second fabrication step is an extended etch using CCP-RIE in which the underlying SiO_2 is removed from exposed areas

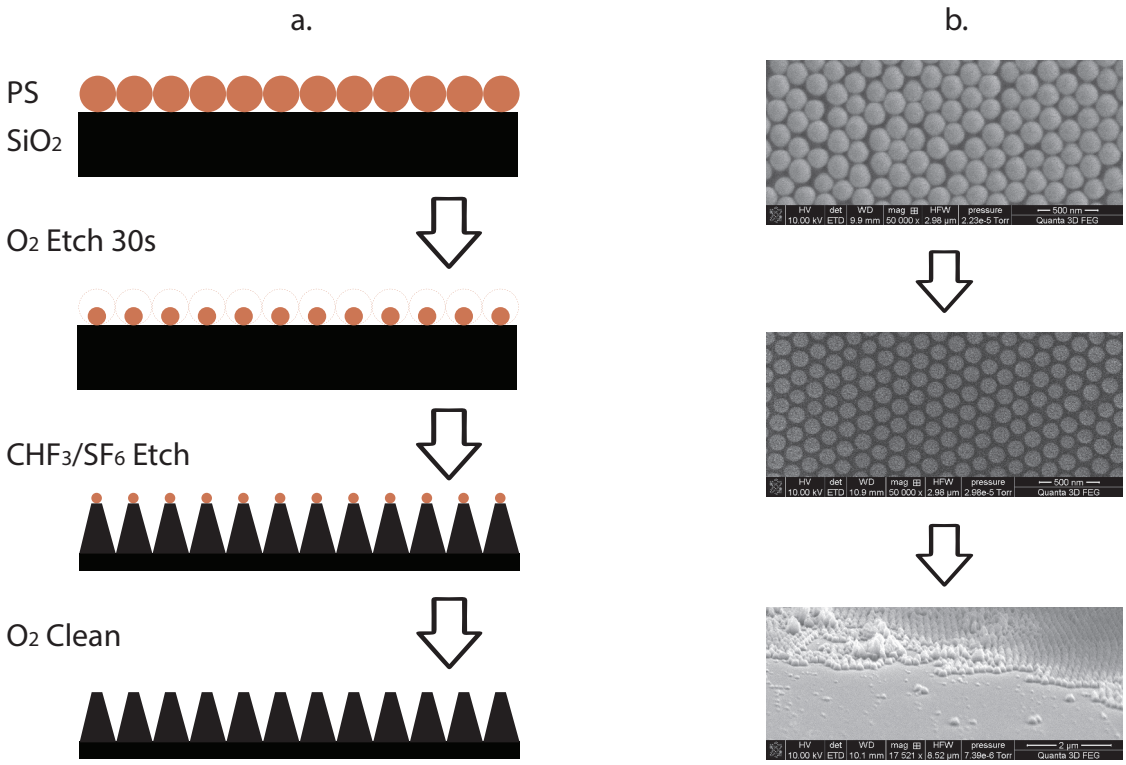

Fig. 3.7 Diagram and SEM Micrographs of RIE process used for the fabrication of MEAR surfaces. In (a), a process similar to that of Fig 3.1 is carried out using PS nanoparticles as the etch mask, in (b) the corresponding micrographs may be seen.

on the substrate, while the remaining nanoparticles act as an etch mask resulting in the apparent growth of nanopillars. The final fabrication step is a post-processing clean, again using O_2 plasma. This is intended to remove any residual mask material.

In the first fabrication step, the size of the particles in the mask layer is reduced by oxide etching at $100W$ RF power, $8mTorr$ chamber pressure with an O_2 flow rate of 10 standard cubic centimeters per minute ($sccms$). Etches were carried out at various time steps from

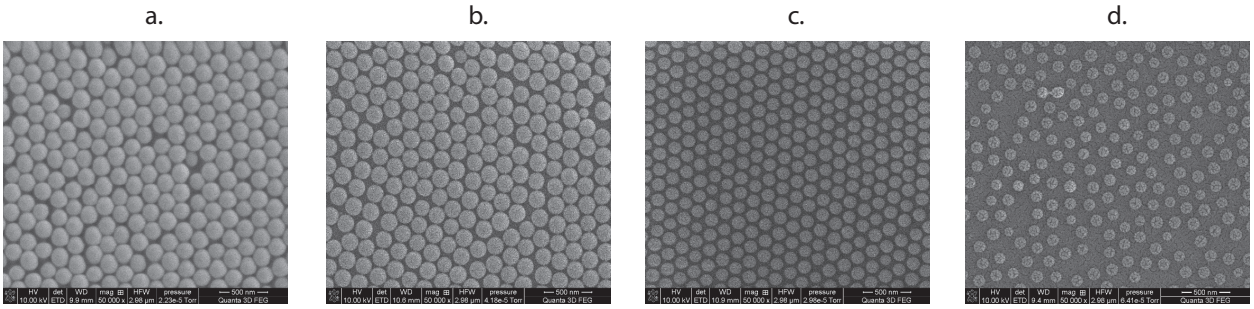

Fig. 3.8 SEM micrographs of etch masks produced through the colloidal deposition method and subsequently etched using O_2. The change in particle diameter as a function of time is visually apparent, after 45 seconds of RIE the mean particle diameter has been reduced from $176nm$ to $123.5nm$.

$15s$ to $1m30s$ and the mean inter-particle distance post-etch was determined by examination under a scanning electron microscope, SEM micrographs obtained before and after the mask reduction step are shown in Fig 3.8. The mean inter-particle distance as a function of time is plotted in Fig 3.9, as well as a linear fit to the data which reveals an approximate diameter reduction-rate of $1.2nm/s$. During subsequent etching work the mask layer was exposed to a $30s$ mask size reduction step, yielding a $15nm$ reduction in individual nanoparticle radius, and an average mask separation-distance of $30nm$.

The primary challenge during fabrication was the selection of the appropriate etch recipes. While the fabrication of MEAR structures on SiO_2 has been reported through the use of gaseous mixtures containing carbon, fluorine, oxygen and hydrogen, dry-etching is a notori-

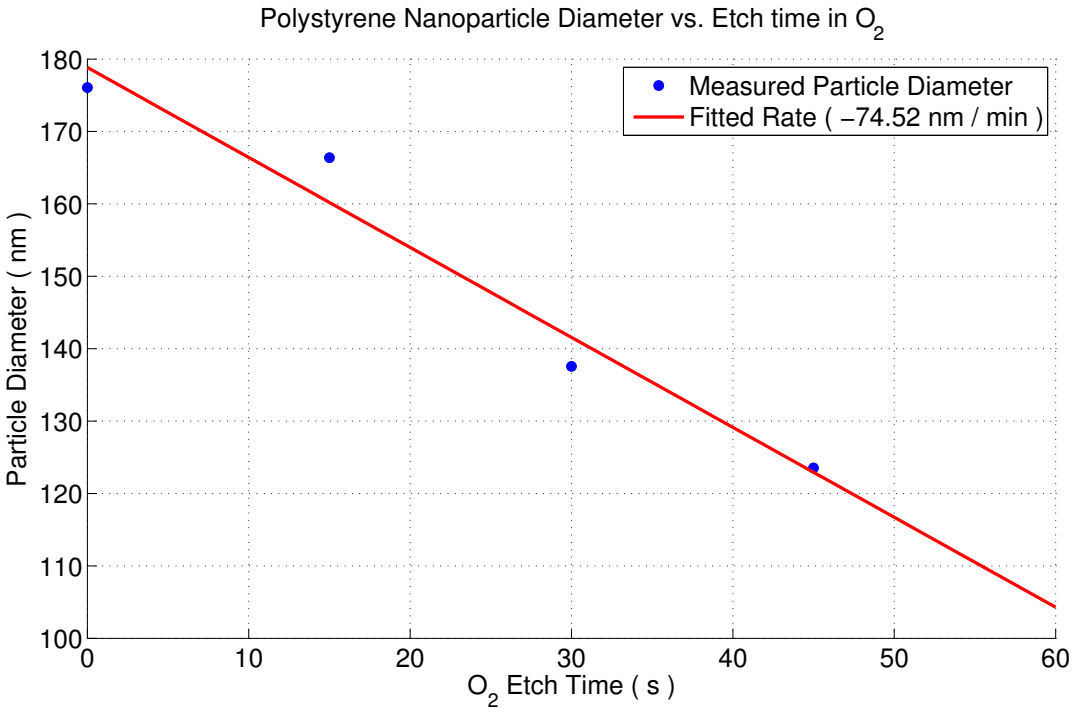

Fig. 3.9 Measured and fitted particle diameters as a function of time, yielding the particle diameter reduction rate of $75nm/min$.

ously particular process and plasma energies, densities, temperatures, and compositions can vary greatly between facilities. Throughout this research a large component of the fabrication work was an investigation into the chemistry of SiO_2 etching and the mechanisms that contribute to anisotropy, etch selectivity and etch rate.

The primary parameters of an RIE process are the plasma energy or temperature, the ion bombardment energy, plasma stoichiometry and the etch time. Unfortunately, with the exception of "etch time" modern RIE fabrication facilities are yet to implement these parameters directly into their equipment interfaces and it is therefore left to the judgement of

the microfabricator to adjust gas flow rates, chamber pressure, RF power and ICP power in order to indirectly control the four primary parameters listed above. The first of these parameters, plasma energy, primarily affects the etch rates as hotter or more energetic species are more likely to chemically react with the substrate; despite the frequent use of the term "bombardment", RIE is a fundamentally chemical process and as such the energy of the reactants involved plays a significant role in the overall yield [40, 53]. The second parameter, ion bombardment energy controls the anisotropy of the etch as a plasma exhibiting higher ion bombardment energy will accelerate ions more strongly in the direction normal to the surface of the substrate, as a result ions will be less likely to arrive at glancing angles and will be able to penetrate further into exposed trenches before reacting with sidewalls. Blindly increasing the ion-bombardment energy, however, is not a one-size-fits-all approach to producing anisotropic structures as increased bombardment energy carries with it the risk of physical sputtering. During physical sputtering ions are arriving with kinetic energies that are large enough to damage the lattice structure of the substrate and thereby remove material from the surface even in the absence of a chemical reaction, the ideal etch process is a non-sputtering chemical etch that is nonetheless close enough to the sputtering threshold to produce anisotropy. Increasing ion-bombardment energy is accompanied by decreasing etch selectivity as the mechanism of physical sputtering does not differentiate between the lattices of the substrate and the mask material [53].

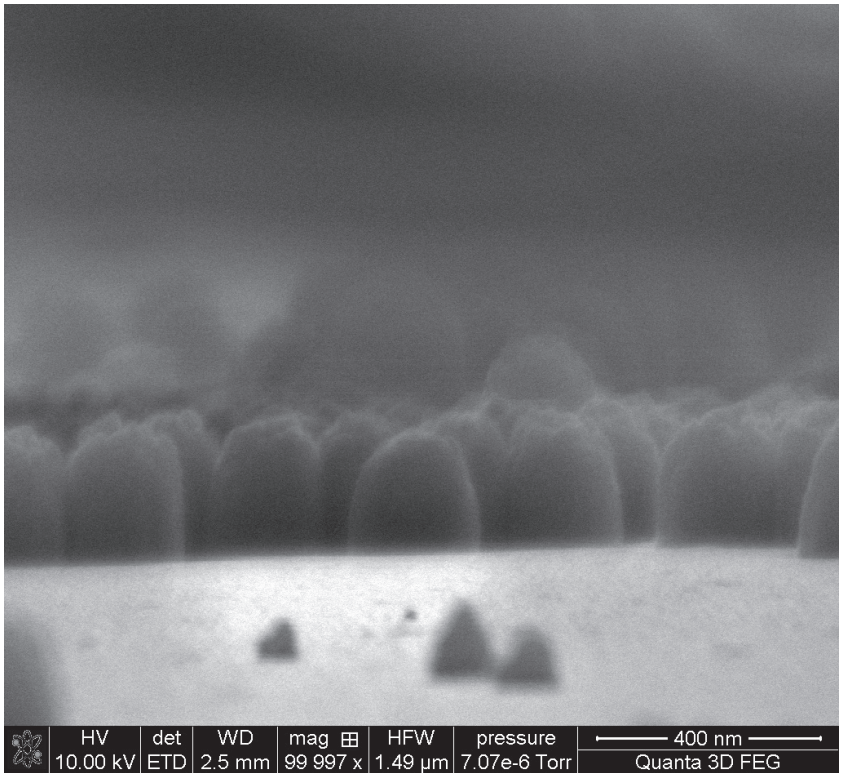

Fig. 3.10 Sideview micrograph of MEAR structures fabricated using a low-powered CHF_3 etch, the MEAR structures exhibit spacing of $180nm$ and heights of $230nm$. The etched profile is roughly parabolic with good uniformity at the sides, although not at the tips–this is likely the result of over-etching.

An increase in the RF power applied to the plasma in a CCP-RIE system will have an impact on the ion density and bombardment energy. Raising the applied RF power will promote the dissociation of electrons from the feed gas, resulting in increased electron-gas collisions and the promotion of a greater number of ionic species in the plasma. The increased dissociation of electrons will also result in a greater number of collisions between the electrons and substrate, thereby raising the DC bias between plasma and substrate and

increasing the anisotropy, and ion-bombardment energy of the etch. The ion-bombardment energy may also be controlled by reducing the etch pressure [53]: decreased pressure during the etch process increases the mean free path distance for ionic species thereby reducing energy loss to free collisions. Tuning of the pressure and RF power then, will control the anisotropy of the etch through increasing the density of the more anisotropic ionic species, as well as increasing the ion-bombardment energy during ion-assisted etch processes.

The third parameter, plasma stoichiometry, is the most complex of the fundamental etch parameters. At the surface level, the gas mixture and associated flow rates employed in a particular etch process would appear to be a direct method by which the plasma stoichiometry might be controlled, and while this interpretation is broadly correct and sufficient for a first approximation it does not paint a full picture of plasma interaction. To understand the interplay between the gas mixture and the precise stoichiometry of the plasma it is useful to recall Fig 3.2 and revisit the discussion of plasma formation in a CCP-RIE system. In CCP-RIE gas is excited by an RF source which promotes the formation of plasma through the dissociation of electrons and subsequent formation of radicals, free anions, and cations. For each individual molecule there are multiple molecular transitions that may occur during plasma formation, each with an associated reaction and transition energy; for illustrative purposes, the possible transitions for CHF_3 are listed in Table 3.3. The likelihood of a particular molecule undergoing these transitions at any one time is dependent on the power supplied by the RF source as well as the electron and positive ion density in the area im-

No.	Reaction	Electron energy loss (eV)
1.	$e^- + CHF_3 \rightarrow CF_3^+ + H + 2e^-$	15.2
2.	$e^- + CHF_3 \rightarrow CHF_2^+ + F + 2e^-$	16.8
3.	$e^- + CHF_3 \rightarrow CF_2^+ + HF + 2e^-$	17.6
4.	$e^- + CHF_3 \rightarrow CF^+ + 2F + H + 2e^-$	20.9
5.	$e^- + CHF_3 \rightarrow F^+ + CHF_2 + 2e^-$	37.0
6.	$e^- + CHF_3 \rightarrow CHF^+ + 2F + 2e^-$	19.8
7.	$e^- + CHF_3 \rightarrow CF_3 + H + e^-$	11.0
8.	$e^- + CHF_3 \rightarrow CHF_2 + F + e^-$	13.0
9.	$e^- + CHF_3 \rightarrow CF_2 + HF + e^-$	23.6
10.	$e^- + CHF_3 \rightarrow CHF + 2F + e^-$	35.0
11.	$e^- + CHF_3 \rightarrow CF + 2F + H + e^-$	13.3
12.	$e^- + CHF_3 \rightarrow CF_3 + H + e^-$	11.0
13.	$e^- + CHF_3 \rightarrow F^- + CHF_2$	1.3
14.	$e^- + CHF_2 \rightarrow CF_2^+ + H + 2e^-$	17.2
15.	$e^- + CHF_2 \rightarrow CHF^+ + F + 2e^-$	14.3
	...	
23.	$e^- + CF_3 \rightarrow CF^+ + 2F + 2e^-$	21.4
	...	
33.	$e^- + CF \rightarrow C + F^-$	2.1

Table 3.1 Reactions and corresponding electron collision energies for the first 33 dissociation reactions in a pure CHF_3 plasma. This table has been reformatted and reproduced from an unlimited report by Sandia National Laboratories [1], which is derived using reaction cross sections from [2–4].

mediately surrounding the molecule under consideration. Hence, even a plasma composed of a single reactive species may experience differences the relative concentrations of its ionic species as the pressure and RF power are varied. It should come as little surprise then, that the introduction of multiple species into a simple CCP-RIE environment will compli-

cate matters, as different molecules will increase the ambient ion-density by greater or lesser amounts according not only to the pressure and RF power, but also by their response to the dissociated ions of other reactive species listed in Table 3.3.

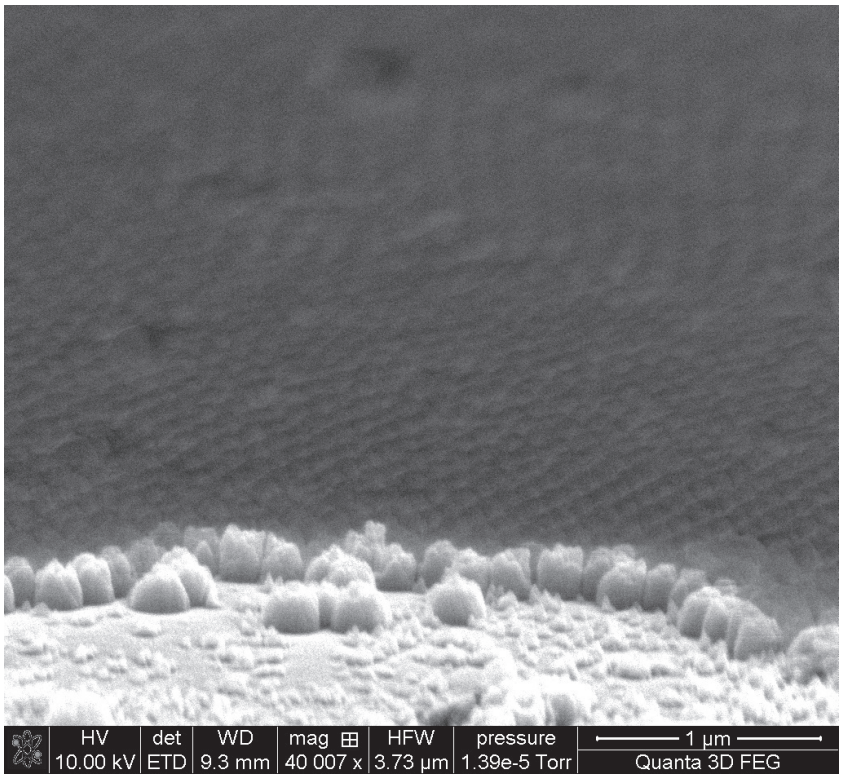

Fig. 3.11 Tilted SEM micrograph showing a MEAR structure fabricated through bombardment with CHF_3 and O_2; detritus can be seen strewed around the base of the HCP region and closer inspection reveals chips in the sidewall of the individual MEAR structures. These nano-fractures in the SiO_2 lattice indicate that the bombardment energy is too high.

There is a careful atomic interplay between the atomic species present in a CHF_3/O_2 plasma or $CF_4/O_2/H_2$ plasma controlling the etch rate, selectivity and anisotropy of Si/SiO_2

etching [41, 53–57]. The driving mechanisms behind SiO_2 etching using these gases are the two reactions between carbon radicals and surface oxygen, and fluorine radicals and the underlying silicon. In a pure CF_4 plasma the ionic species CF, CF_2, and CF_3 will form along with ionic and radical F species due to the dissociation of fluorine atoms through impacts with excited electrons. Etching of the SiO_2 substrate will then proceed through the chemical interaction between radical F species and SiO_2 where the fluorine takes the place of oxygen in the SiO_2 lattice following the reaction [57]

$$4F + SiO_2 \rightarrow SiF_4 + O_2. \tag{3.1}$$

This reaction is isotropic and hence unsuitable for the production of high aspect-ratio structures, however, anisotropy may be achieved by the addition of H_2 to the gas mixture. The introduction of H atoms into the plasma mixture will serve to partially remove free F species from the mix through recombination to form neutral HF species [53, 54, 58]; the reduction in free F relative to CF_3, CF_2, and CF species will result in increased etching by carbon containing species, as well as some formation of a fluorocarbon polymer CF_{x} on the surface of the substrate. An example of SiO_2 etching by carbon species occurs is given by the reaction [57]

$$4CF_3 + 3SiO_2 \rightarrow 2CO + 2CO_2 + 3SiF_4 \tag{3.2}$$

The formation of a CF_{x} polymer on the surface of SiO_2 acts as a barrier to the reactive

species in the plasma, attenuating the impact energy of incident ions, reducing etch rates, and increasing the anisotropy by inhibiting chemical etching by radical F [53]. This same effect occurs during CHF_3 etching, without the need for further addition of H_2 [59]; the F/C ratio can be understood, then, to be the controlling factor behind the formation of the passivation layer, and hence the anisotropy and etch rate of the process itself. The F/C ratio may be further altered, however by the introduction of a high-fluorine gas such as SF_6 or by the addition of O_2 which will bond with free CF_{x} to form COF_{x} species, CO, and CO_2 [53, 54, 56]. The removal of CF_{x} species, and the lack of significant interaction between O_2 and free F will therefore increase the F/C ratio. The addition of O_2 to a fluorocarbon or hydrofluorocarbon plasma is expected to inhibit polymer formation, increase etch rates and decrease anisotropy–a careful balance must be maintained in order to achieve high aspect-ratios. The F/C ratio to the point where a thin passivation layer forms, but not to reduce it to the point where net fluorocarbon deposition occurs [59, 60]. Achieving this can be particularly difficult when adding complex gases such as SF_6 since the breakdown energy of the gas is different to that of CF_4, so for example an equal gas mixture of SF_6 and CF_4 would not necessarily produce an F/C ratio of 10/1.

Altering the gas chemistry, then, will allow for some control over the F/C ratio, either through the introduction of additional F species or the removal of C and F. Controlling the F/C ratio will then allow the microfabricator to tune the polymer deposition rate and control the passivation layer thickness. The thickness of the passivation layer, and the related

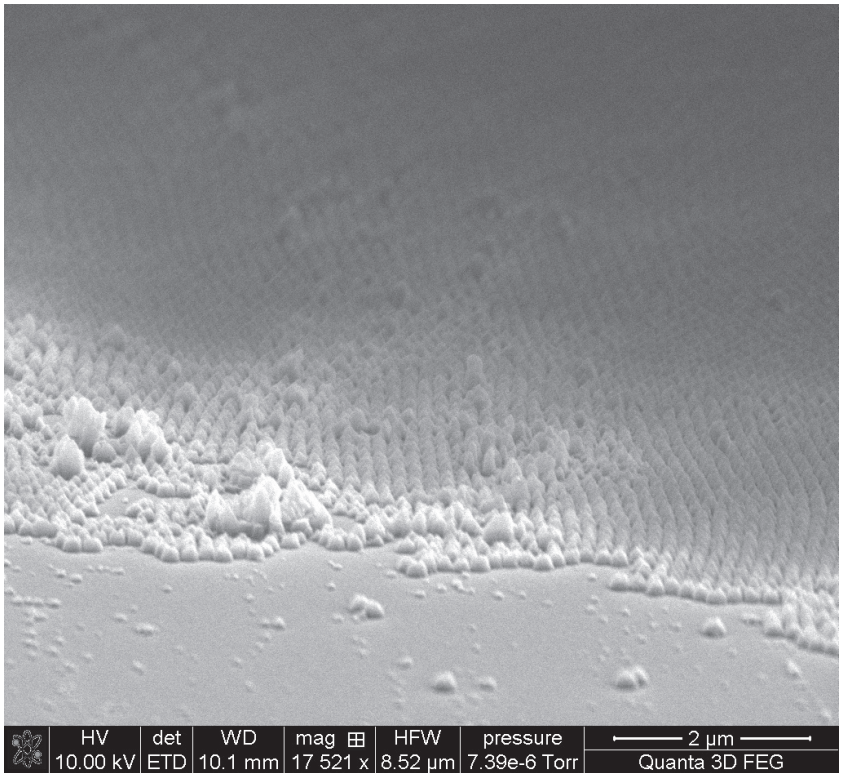

Fig. 3.12 Tilted micrograph of clean, evenly spaced MEAR structures etched using pure-$SF6$. These structures display a conical profile and spacing on the order of $180nm$, unfortunately the their structure height was less than $200nm$, making them unsuitable for MEAR operation.

etching characteristics may also be tuned by the impact energy of the ions, as higher energy ions will preferentially remove the passivation layer rather than add to it. Assuming an etch process in which the F/C ratio has been lowered to the point where polymer formation occurs, then etching must be assisted by ion-bombardment in which high energy ions strike the passivation layer with sufficient energy to reach and etch the underlying SiO_2 through the etch process detailed in equations 3.1 and 3.2. Bombardment energy, as previously discussed,

is a function of the pressure and applied RF power. Therefore changing the etch chemistry in an SiO_2 etch will strongly affect the etch mechanism from a chemical standpoint, which will have implications for the required RF power and chamber pressure.

A number of etch chemistries were employed using both CCP-RIE and ICP-RIE methods; the suitability of pure CHF_3, pure SF_6, two different $CHF_3 + O_2$ mixtures as well as a $CHF_3 + SF_6$ mixture were all examined, and it was ultimately determined that a combined $CHF_3 + SF_6$ chemistry yielded structures with the greatest aspect-ratio. The parameters for these etch processes are listed in Table 3.3; a micrograph corresponding to the low-powered etch in the first line of Table 3.3 is shown in Fig 3.10. The high-powered $CHF_3 + O_2$ etch found in the fourth line of Table 3.3 is shown in the micrograph in Fig 3.11. By far the smoothest and cleanest MEAR structures were fabricated using the pure SF_6 recipe described in line three of Table 3.3, its corresponding micrograph is shown in Fig 3.12.

In an effort to increase selectivity in the original CHF_3 dominated etch, SF_6 was introduced in order to increase the F/C ratio and reduce the passivation layer as discussed above. The addition of SF_6 to CHF_3 yielded SWG structures with greatly improved feature height and aspect ratio (Fig 3.13), however the control of structure profile was poor and as a result optimal MEAR structures could not be realized. Despite the introduction of a passivating layer, and the accompanying benefits in terms of sidewall protection, the selectivity between PS and SiO_2 remained poor. The structures produced through the addition of SF_6 to the process gas do exhibit the same hexagonal spacing as the original mask layer, however the

Pressure (mTorr)	**RIE (W)**	**ICP (W)**	O_2 **(sccm)**	CHF_3 **(sccm)**	SF_6 **Flow (sccm)**	**Height (nm)**	**Etch Rate (nm/min)**
8	85	200	0	40	0	226.3	40.2
8	100	200	0	40	0	234.1	22.7
8	300	150	0	0	7	152.0	30.9
10	300	150	5	25	0	161.7	32.3
30	150	0	5	30	0	165.6	77.4
60	150	0	0	30	5	1176.7	28.2

Table 3.2 Table of structure heights and etch rates achieved through each etch recipe found to produce MEAR structures, the etch mechanism is an estimate based on the etch selectivity, pressure, and observed etch rate as well as the morphology of moth-eye structures under examination by SEM.

inter-particle sites have been filled with needle-like structures that are the result of micro-masking [29] during the etch process. Earlier in this chapter it was noted that the addition of CHF_3 to an RIE etch process acts to reduce the F/C ratio and promote the deposition of a passive fluorocarbon layer which then protects the substrate. The fluorocarbon polymer inhibits chemical etching of the underlying material in the same manner as a traditional etch mask, one which may be controlled through increased ion bombardment or the addition of SF_6 or O_2. Micromasking occurs when a small localized clump of fluorocarbon is deposited on the surface of the substrate temporarily reducing the selectivity in this area in precisely the same manner as a traditional etch mask. The material under the micromask will remain protected from further fluorine etching, and the exposed sidewalls will continue to be protected as the surrounding substrate material is removed. Indeed, the micromasking effect

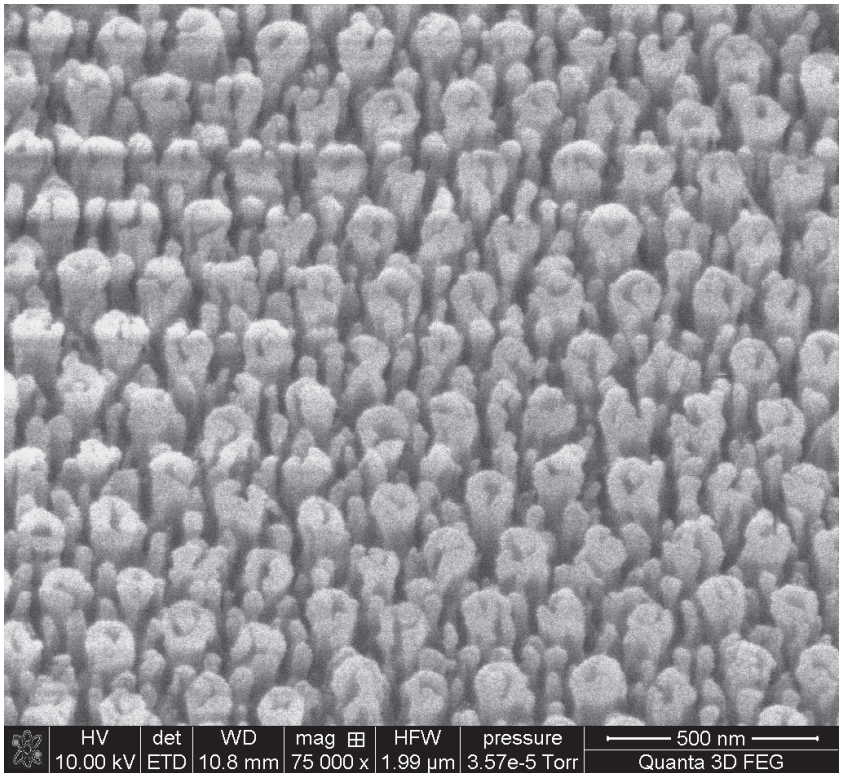

Fig. 3.13 Zoomed-in view of tilted SEM micrograph of MEAR structures fabricated under a colloidal etch mask using a mixture of $CHF_3 + SF_6$. The subwavelength spacing has been decreased thanks to the formation of nanopillars or needles at sites in-between the larger, hexagonally spaced pillars.

in the $CHF_3 + SF_6$ mixture was effective enough to produce micromasked needles with the same height as the hexagonally spaced MEAR features. This indicates that the PS mask is being removed quickly and the resultant structures are formed by the same micromasking mechanism as the adjacent nanopillars.

A major disadvantage of micromasked structures is the lack of a well-defined array pattern, as well as the lack of profile control. It is not possible to produce truly optimal MEAR

structures through micromasking–thanks to the lack of profile control; however, it is possible to achieve the idealized spacing detailed in Chapter 2. The micromasked structures are expected to produce subwavelength antireflective effects as they continue to meet the subwavelength criterion defined in Chapter 2. Furthermore, across the transition from air to the substrate, micromasked structures are expected to gradually increase the fill-factor from zero to near-unity, ensuring a graded refractive-index (GRIN) transition. Therefore, provided that micromasked structures meet the height constraint $h > 0.4\lambda_{\max}$ it is expected that the surface will demonstrate enhanced AR performance, especially at high angles of incidence. The MEAR or more appropriately, SWAR, applications of micromasked structures are more explicitly investigated in the following section.

Aspect ratios near 5:1 [12, 16, 28] demonstrating clean structure profiles have been reported by other groups, however these results could not be replicated without access to the specific $CF_4/H_2/O_2$ chemistry required for this process. The difficulty of replicating the reported results of other groups, as well as the low upper limit in terms of aspect-ratio demonstrates that direct etching using PS etch masks is unsuitable for CubeSat applications.

3.4 Single-Step Fabrication Method

The realization that micromasking is the mechanism behind nano-needle formation in the the inter-particle gaps, as seen in Fig 3.13, as well as the conclusion that the primary fea-

tures may have also formed due to micromasking calls for further investigation. Specifically, if micromasking produces nano-needles in areas where no etch mask is present, and those features exhibit the required height for SWG AR then it is valuable to address the question: "can a top-down SWG AR surface be fabricated in a single step, without a traditional etch mask, solely through the use of the micromasking-effect?"

If applied to a bare surface, micromasking may create a sparse forest of nanopillars often referred to as "RIE grass" [61,62]. In fact, the process of RIE grass formation is well-known and is documented in most process handbooks as an undesirable by-product of low-F/C etch processes. RIE grass was briefly a topic of interest in traditional silicon microfabrication research for its ability to produce highly anti-reflective silicon, dubbed "black silicon" [14,63]. Despite the low reflectance achieved by black silicon, high-aspect MEAR structures with tailored profiles tend to exhibit superior performance. The relative ease of MEAR fabrication in silicon makes tailored MEAR surfaces the preferred AR technology over black silicon; in SiO_2, however, MEAR fabrication is not so straightforward. The phenomenon of RIE grass formation has also been observed in SiO_2 etching, where it is termed "glass grass" [29] however to-date no groups have investigated the AR applications of these features in SiO_2.

Micromasking in SiO_2 is known to produce a variety of subwavelength structures with differing morphologies dependent on bombardment energy. Needle, pyramidal and tube-like

structures have all been demonstrated as a result of micromasking in SiO_2 [29, 62]. Of these, tubed structures show potential for use as MEAR-like surfaces due to both their tight subwavelength spacing and greater tensile strength. The mechanism for tube formation is not yet fully understood, however it bears resemblance to the formation of tube-like structures due to "metal-assisted" or "catalytic" etching [37, 64]. The central channel of tubed glass grass is known to extend down to the base of the cylinder [29], similar to tubes formed through catalytic etching. In this case, a dense forest of tubes is expected to exhibit a subwavelength pitch of half the diameter of the tubes themselves. Furthermore, it has been demonstrated that tubed glass structures can reach heights of up to $15\mu m$, meaning that tubed glass grass is capable of meeting both the height and pitch requirements of the optimal MEAR structures [65].

Using the mixed $CHF_3 + SF_6$ etch recipe described in Table 3.3 the fabrication of glass grass tubes was investigated. Feature heights under four different process times were measured by SEM imaging at a tilt of 30°; the process times were: 8 minutes, 12 minutes, 25 minutes, and 35 minutes. A linear fit to the observed etch heights is shown in Fig 3.14 demonstrating an etch rate of approximately $28nm/min$, which is consistent with reported values for SiO_2 etching in fluorine plasmas [66]. After etching for $45min$ the observed feature height was $1177nm$, while the peak to peak separation of subwavelength features was $134nm$. Hence, disordered structures with aspect-ratios of approximately $9:1$ were achieved using a single-step fabrication process without a traditional etch mask. Quartz wafers were

etched for 45 minutes with no pre-processing or post-processing treatments and the resultant subwavelength structures are shown in Fig 3.15. This process was repeated multiple times, and multiple cleaning steps in high-energy O_2 were used in order to verify that the structures are composed of underlying SiO_2 material and merely CF_x polymer deposited during the etch process.

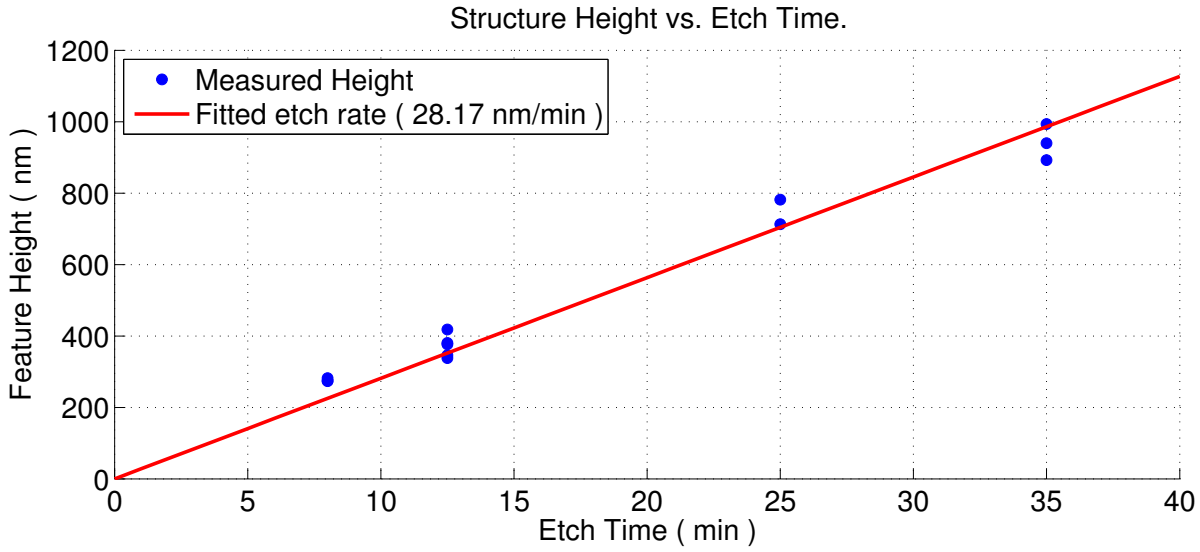

Fig. 3.14 Measured and fitted structure height as a function of time in $CHF_3 + SF_6$ plasma, yields an etch rate of $28nm/min$.

A point on nomenclature: glass grass structures are not true MEAR surfaces. Although these structures are still expected to show increased AR performance this is due to SWAR and cannot truly be said to be "MEAR" as the structures lack the characteristic ordered, hexagonal spacing. As previously noted, MEAR is a subset of SWAR–*i.e.* MEAR operates

on the SWAR principle–and the fundamental requirement of subwavelength feature-spacing for MEAR operation is in fact the same fundamental requirement for SWAR. Irrespective of nomenclature, then, the demonstration of this fabrication method is a significant result in light of the fact that single-step micromasking fabrication is a much simpler and more repeatable etch process that is expected to produce comparable results to more labour intensive lithographic approaches. Micromasking eliminates the need for colloidal mask deposition, which was the most variable step in the fabrication procedure. Indeed, the ability to fabricate SWG AR surfaces without the use of time-consuming and labour-intensive mask preparation makes the use of the glass grass method an attractive option for CubeSat developers unwilling to pursue full-fledged nanofabrication.

In summary, the deposition and tuning of a mask layer was demonstrated and multiple etch chemistries were considered in pursuit of MEAR structures. True MEAR structures at the desired feature heights of $500nm$, and $1204nm$ could not be realized, in that the precisely ordered spacing that is a formal requirement for MEAR operation was not achieved. However, ordered and disordered SWAR structures meeting both the subwavelength constraint and the desired height were achieved. These structures are expected to exhibit comparable performance to their MEAR counterparts by virtue of the dependent between SWAR and MEAR, in which the MEAR-effect is merely a specific instance of SWAR. A single step fabrication approach was developed that immensely simplifies the production of SWAR

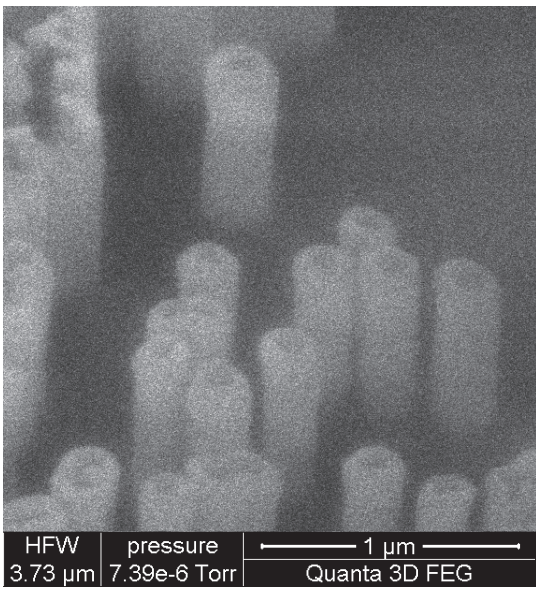

Fig. 3.15 SEM micrograph of 1177nm subwavelength AR structures produced through the "RIE grass" method with no etch mask applied. A sparse region is shown in order to highlight the height and aspect-ratio of the structures

surfaces on SiO_2. It is possible that this effect could be further used to produce highly optimized MEAR-like surfaces with mixed feature profiles similar to structures designed by Ji *et al.* [16]. Using this approach irregularly spaced subwavelength features with maximal height of 1177nm, and average spacing of 134nm were produced, as well as more regularly spaced features with maximal height of 350nm and pitch 130nm. This represents a significant improvement over the aspect-ratio achievable using direct PS on SiO_2 etching, at the expense of tight profile control. The cost of fabricating these structures is not unduly expensive; a one-hour etch session would yield enough glass to cover one side of a 1-U CubeSat (100mmx100mm) at cost of 90$. Covering a 1-U CubeSat, then would cost 540, an insignif-

icant amount when compared to the typical budget of a CubeSat mission. In the following chapter the the AR performance of these SWAR structures is examined.

4 Performance Tests of Antireflective Coverglasses

Procedures for characterizing SWAR surfaces are well established in the literature [67,68]. Spectral transmission coefficients at normal incidence is typically used, as these measurements are readily comparable to common modelling techniques. Unfortunately the majority of characterization methods are limited to normal or very low angles of incidence, and are therefore unsuitable for evaluating the impact of MEAR structures for CubeSat applications. Typically a MEAR-enhanced, or SWAR-enhanced substrate is illuminated at normal incidence by a broadband white-light source, the transmitted light passes into an integrating sphere after which the light is coupled to a spectrometer [12, 16, 24, 43]. An established alternative is to place the sample at the rear of an integrating sphere and measure the amount of light that is reflected when the sample is illuminated by an external source [63, 67–69]. One benefit of reflectance measurements versus transmittance measurements is that they can also be performed cheaply using a reflectance probe [43]. Null-diffraction is guaranteed by the subwavelength criterion, provided that the range of aperiodic spacings in a disordered structure falls below the subwavelength limit. This has been experimentally confirmed

by measurements of diffuse reflectance in RIE-grass on Silicon [70], confirming that both transmittance and reflectance measurements of SWAR surfaces need only consider specular components.

When non-normal angles of incidence are examined measurements are typically restricted to angles of incidence $< 60°$. One notable exception is an experiment operated at the University of Southampton [68] in which transmission coefficients as a function of both wavelength and incident angle were measured to a high degree of accuracy in order to perform a 1:1 comparison between experimental data and the results of RCWA calculations such as Fig 2.10. Briefly, this experiment used a highly coherent white light source from a fixed position to illuminate a MEAR-enhanced silicon substrate mounted to a rotating stage. Specular reflection at an angle θ_{inc} was measured by positioning a mobile optical fibre aperture at incidence, $-\theta_{\text{inc}}$ from the substrate normal such that specular components of reflected light would fall directly on the aperture of the integrating sphere. The reflected light was then fed to an optical fibre and the intensity as a function of wavelength could be measured using a spectrometer. This experimental apparatus produced accurate measurements of the transmission coefficients at wavelengths between $450nm$ and $850nm$ and incidence angles between $0°$ and $85°$ which agreed well with RCWA simulations. This method is ideal for investigating different MEAR structure morphologies and their effects on the transmittance and reflectance of a substrate. However, if the objective is merely to demonstrate angular MEAR enhance-

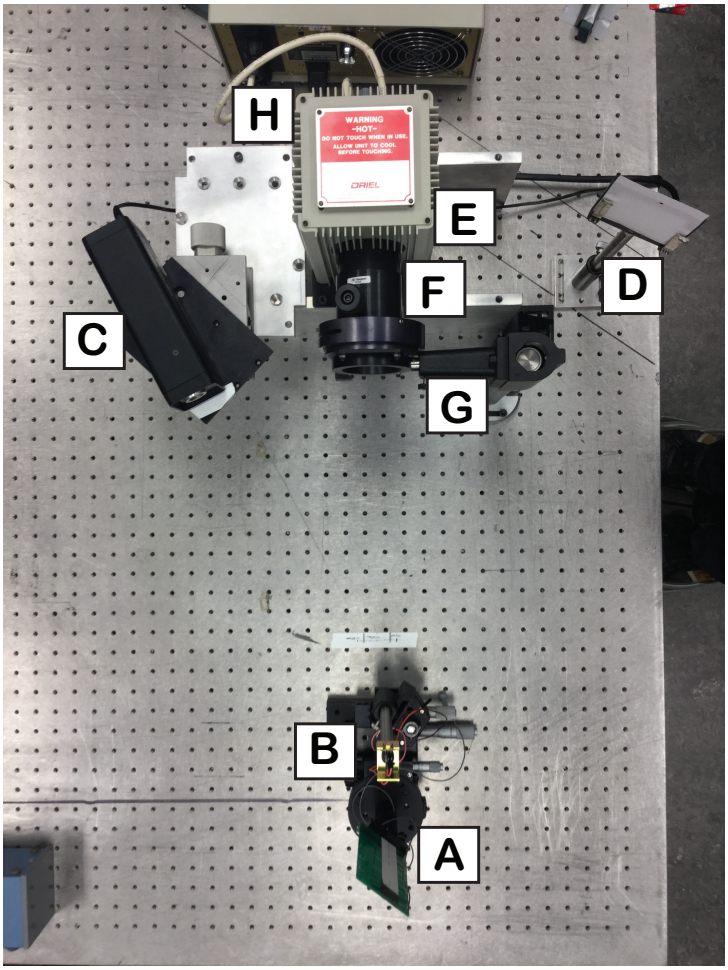

Fig. 4.1 Experimental setup on optical table. Solar cells are mounted to a rotation stage as well as a horizontal translator (A). A photodiode, (B), acts as a power meter. The cell is aligned using a fixed laser-source, (C), which reflects off of a flat mirror adhered to the PCB and onto a $1mm$-ruled screen, (D). Cells and power sensor are illuminated under light from an arc-lamp, (E), which is collimated, (F), and manually shuttered, (G).

ment then the wavelength dependency of the transmission coefficients is not required. The performance of a solar cell on orbit will be dependent on the angular transmittance of the

coverglass with respect to a solar spectrum; hence it is sufficient to reproduce Fig 2.8 *in experientia* absent detailed knowledge of spectral characteristics.

4.1 Optical Test Setup

To test the efficacy of the moth-eye surface at high angles of incidence an optical test-bed was assembled. Solar cells were mounted to a printed circuit board (PCB), aligned using a rotating stage and fixed laser source and illuminated by a light source with spectral irradiance approximating the solar spectrum. This setup is shown in Fig 4.1. This apparatus is expected to produce sufficiently small uncertainties to demonstrate the moth-eye effect in SiO_2 coverglass mounted to TASC cells.

Using the optical testbed pictured in Fig 4.1, and further detailed in Fig 4.2 it is possible to determine the short circuit current of the cell by direct measurement using a digital ammeter. Adjustment of the rotation stage from 0° to 90° allows for full characterization of the performance of a particular cell across all incident angles. Unfortunately, this measurement is complicated by the fact that MEAR and SWAR structures cannot be simply "added" to coverglass once that glass is already attached to a solar cell. Furthermore, the coverglass adhesion process is non-reversible, so it is not possible to measure a cell with bare glass, then remove the glass, fabricate a MEAR or SWAR surface and re-apply the glass. In order to determine the enhancement in transmission, then, four sets of incidence-angle data must be

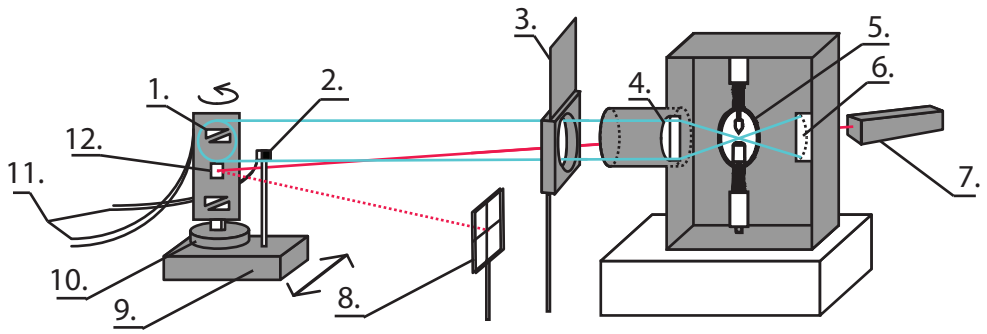

Fig. 4.2 Schematic view of experimental setup. 1. Solar-cells mounted to PCB affixed. 2. Photo-diode power-meter (Thorlabs FDS100-CAL) positioned in the lower-half of illuminated area. 3. Manually operated shutter. 4. Aspheric collimating lens (ORIEL 60006 f/1.5, $\oslash 33mm$). 5. 75W Xenon arc-lamp (ORIEL 6263). 6. Concave rear-reflector assembly (ORIEL 60005) 7. Alignment laser with output beam (solid red) and reflected "alignment" beam (dashed red). 8. Imaging screen for reflected beam. 9. Linear translator stage (Thorlabs). 10. Manual rotator stage (Melles-Griot). 11. Leads from cells and power-sensor; I_{SC} is measured by an ammeter (Agilent U2741A digital multimeter), and the power-sensor is read-out via a standard data-acquisition device (NI USB-6009 DAQ). 12. A flat mirror used to reflect the "alignment" beam.

measured across two different cells: cell A, and cell B. First the short circuit current response to incidence angle changes in cells A & B must be determined in the absence of any coverglass *i.e.* the "bare" cell response. Second, MEAR enhanced coverglass will be adhered to cell A, and bare untreated coverglass will be adhered to cell B. Coverglass in place, incidence-angle data is re-collected for each cell and the resultant data may be compared as follows:

$$I_{\mathrm{SC}}(\theta) \propto T(\theta) \propto P_{\mathrm{max}}, \tag{4.1}$$

$$\frac{I_{\mathrm{SC}}(\theta)'}{I_{\mathrm{SC}}(\theta)} = \frac{I_{MEAR}(\theta)}{I_{GLASS}(\theta)} \tag{4.2}$$

Where $\frac{I_{\mathrm{SC}}(\theta)'}{I_{\mathrm{SC}}(\theta)}$ represents the short circuit current ratio of MEAR enhanced glass relative to untreated glass, this is equivalent to the ratio of optical transmittance, as well as the ratio of $P_{\max}$. Unfortunately I_{MEAR} from cell A and I_{GLASS} from cell B are not directly comparable as the individual current characteristics, I_{BARE} of cell A and B will be different. This problem may be removed by normalizing the MEAR and untreated glass curves to their respective bare-cell curves which is then equivalent to directly comparing I_{MEAR} to I_{GLASS} for the same cell

$$\frac{I_{\mathrm{SC}}(\theta)'}{I_{\mathrm{SC}}(\theta)} = \frac{I_{MEAR-A}(\theta)}{I_{BARE-A}(\theta)} \cdot \frac{I_{BARE-B}(\theta)}{I_{GLASS-B}(\theta)}. \tag{4.3}$$

The light source used for performance testing is a 75-Watt Xenon arc-lamp purchased from Oriel instruments (ORIEL 6263), which provides sun-like spectral-emission allowing for simulation of the space environment; hence the relative improvements of solar cells under Xenon lamp illumination are likely to be similar to the improvements seen on orbit. Within the arc lamp housing seen in Fig 4.2 a rear-reflector assembly is used to maximize light output and a collimating assembly is included in order to ensure a planar wavefront at the solar cell array. The collimating assembly consists of a single aspheric lens with f/1.5 producing a beam diameter $\oslash 33mm$; some beam-expansion is to be expected due to chromatic dispersion, however this will not affect relative measurements. The integrated spectral irradiance

of the light source after the condenser and reflector conversion factors have been applied results in a total beam power density of $1037.1 W/m^2$. This is similar to the power density of the AM1.5G solar spectrum–the same conditions under which the cells were tested by the manufacturer. The conversion factor for the lens is 0.06; the conversion factor for the rear-reflector assembly is 1.6.

4.1.1 Uncertainty Analysis: Temperature

Typically when solar cell performance tests are carried out the temperature of the cell is stabilized using a Peltier or water-cooled stage. In the absence of active cooling cell heating is minimized by illuminating the cell for only milliseconds at a time. In this experiment no active thermal control was used, instead the temperature was regularly monitored and heating effects during measurements were linearized and eliminated.

Solar cells, like photodiodes, generate a stable current when exposed to light; incident photons carrying energy $E = hc/\lambda$ strike the semiconducting lattice of the cell, releasing bound electrons and simultaneously creating positively-charged holes in the lattice. For a semiconductor material such as Silicon the energy required to motivate this dissociation of lattice electrons, the "band-gap energy", is $1.12eV$, hence photocurrent may only be generated by incident photons with $E \geq 1.12eV \iff \lambda \leq 1103.1nm$. Electrons excited

with $E > 1.12eV$ will transfer their energy to the lattice in the form of lattice-vibrations or phonons, which will cause undesirable heating of the cell. Broadband light sources, which will have a distribution of photon energy are therefore expected to cause heating in the cell. The TASC cells used for the purpose of this research are triple junction cells, meaning that they are a composite of three different cells with three different band-gaps ($GaInP_2$, $GaAs$, and Ge with $1.80eV$, $1.424eV$, and $0.66eV$ respectively). The multi-junction structure of the TASC cell ensures that photon energy absorption is maximized, however residual heating commensurate with the intensity of incident light is still expected.

Heating a solar cell will affect the shape of its characteristic performance function: the "I-V" curve. The I-V curve is a function relating the current and voltage of the cell (I_{out}, V_{out}) to the applied resistance R_{load}; it is the standard performance metric for solar cells. The mechanism of photocurrent generation in which an electron-hole pair is created through photon absorption in the semiconductor lattice is theoretically insensitive to resistive loads *i.e.* the electrical equivalent to a solar cell is a constant current source. As the resistive load of a cell is increased, then, the voltage output of the solar cell is expected to increase while the current remains constant. The voltage will increase in this manner until maximal power output is reached, at which point the current output will drop precipitously. This curve is shown schematically in Fig 4.3. The key values that describe this curve are the open circuit current V_{OC} which occurs at $I_{out} = 0$, the short circuit current I_{SC} occurring when $V_{out} = 0$

and the fill-factor η. These three parameters determine the maximal power output, $P_{\max}$ according to Eq 2.10 which is re-printed in Fig 4.3.

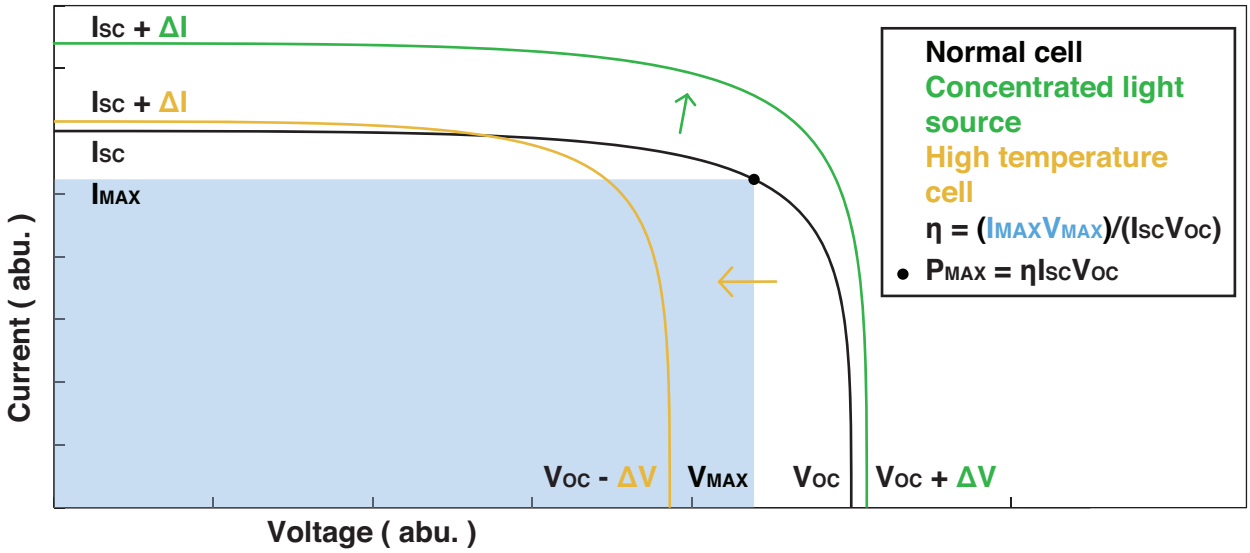

Fig. 4.3 Schematic diagram showing the characteristic or IV curve of a typical solar cell. The fill factor η may be thought of as a measure of the "squareness" of the IV curve. The effect of varying light intensity and cell temperature are also shown.

The temperature dependence of solar cell performance, then, is determined by the interplay between temperature and both I_{SC} and V_{OC}. Of these two factors, variation in $V_{\mathrm{OC}}(T)$ is the more significant. Typically V_{OC} has a linearized coefficient of temperature dependence $\frac{dV_{\mathrm{OC}}}{dT}$ three orders of magnitude greater than the temperature coefficient of short circuit current $C_{\mathrm{I}} = \frac{dI_{\mathrm{SC}}}{dT}$. For the TASC solar cells the thermal coefficient of short circuit current is known to be $< 13.36\mu A/^{\circ}C$ so for any small increase in cell temperature the effect on a

measured value of I_{SC} will be small. In section 4 the short circuit current was identified as the ideal variable to link coverglass transmittance to cell power output, this choice is now reinforced explicitly by the low sensitivity of I_{SC} to cell temperature. To verify the thermal tolerance of the short circuit current a thermistor was attached to the PCB next to the solar cell in the center of the arc-lamp beam and the cell was illuminated for two-minutes. In Fig 4.4 the short circuit current is plotted against the increase in temperature observed in the thermistor. Based on this first order analysis the thermal coefficient of short circuit current was found to be only $7.54\mu A/^{\circ}C$: which is in good agreement with the contention that I_{SC} will not be seriously affected by temperature. In fact the short circuit current was found to have a reliably linear dependence on temperature. Furthermore the time dependence of cell temperature under heating by the arc lamp was found to be sufficiently low that the uncertainty due to temperature effects becomes negligible ($\Delta T/\Delta t = 0.0543^{\circ}C/s$). In particular, the uncertainty associated with changing cell temperature due to heating from the arc lamp over an illumination period of $< 4sec$ is expected to be on the order of $\sigma T = 1.64\mu A$.

4.1.2 Uncertainty Analysis: Beam Intensity

The arc lamp power ripple is 0.5% R.M.S. with a bandwidth of $40Hz$ to $40kHz$; ripple is a repeating sinusoidal signal, therefore I_{SC} values are recorded over long duration pulses ($4s > \Delta t > 2s \iff 160T_{ripple} > \Delta t > 80T_{ripple}$) and the resulting data is linearized to

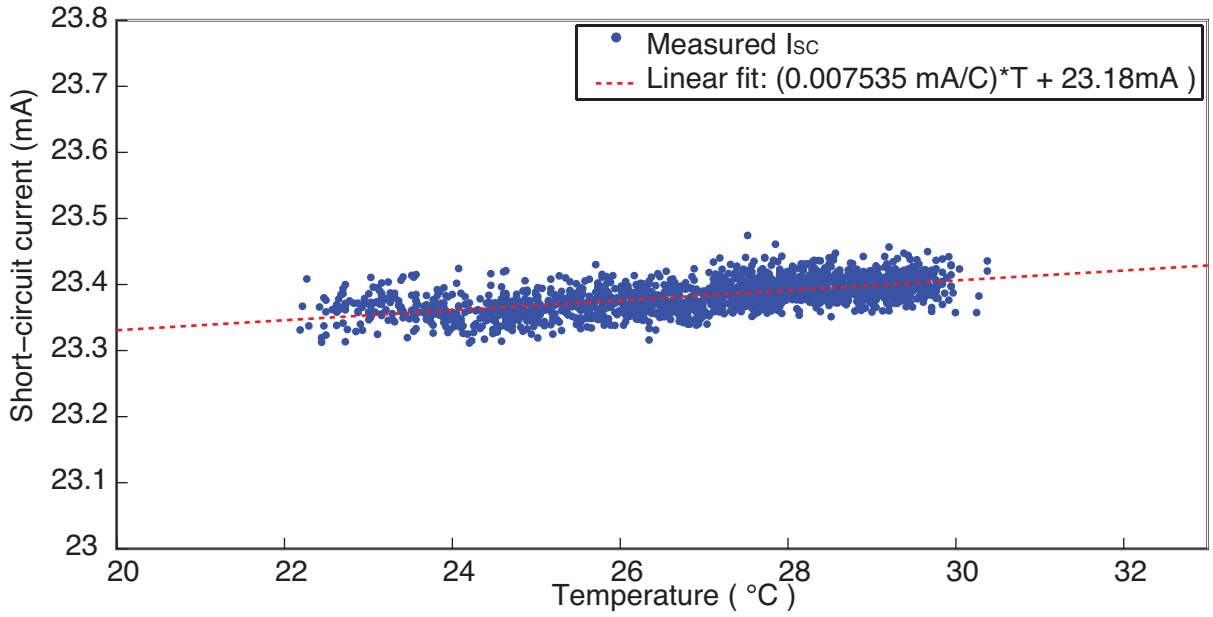

Fig. 4.4 Short-circuit current of the cell at normal incidence plotted against thermistor temperature data. The short-circuit current temperature-coefficient was found to be $7.54\mu A/C$ with an associated $3-\sigma$ uncertainty of $\pm 0.75\mu A/C$

remove the effects of ripple. To measure the long-term drift of the power supply a calibrated photodiode (FDS-100CAL purchased from Thor Labs) is used as a beam power sensor in order to more tightly constrain the uncertainty in the instantaneous beam power. The photoresponsivity of the photodiode in $mAmW^{-1}nm^{-1}$ is an unchanging function inherent to the particular photodiode which is known to lie within 5% of some stated value. This photodiode was then exposed to a calibrated stabilized light source (Thorlabs SLS202M) and the uncertainty of the photodiode response to this source was found to be $< 0.05\%$ of the measured value. While exposure to the calibrated source does not yield any information

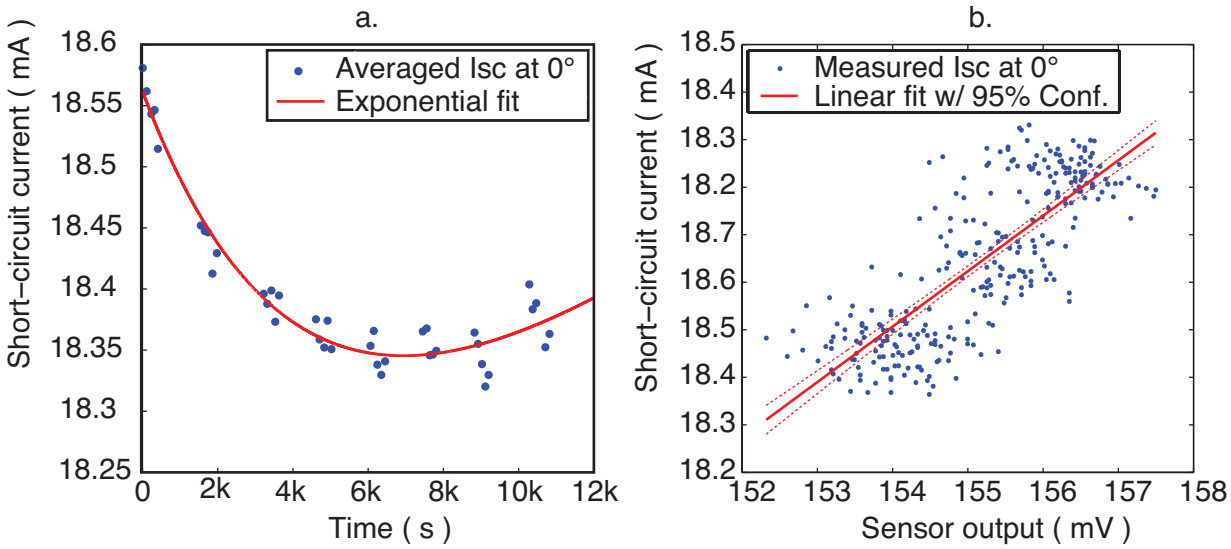

Fig. 4.5 (a) Exponential decay in short-circuit current as a function of time following arc lamp ignition. (b) Relationship between the output of the beam power sensor and the short circuit current throughout exponential time-decay.

regarding the spectral intensity, it does verify that the luminous response is highly repeatable. The arc lamp bulb used is a DC short-arc bulb which is expected to exhibit only minor spectral change in the visible range over its first 100 hours of operation, furthermore any spectral shift as a result of changing conditions in the bulb-envelope are expected to manifest in the far to mid ultraviolet range ($100nm - 300nm$) and will be outside of the spectral range of the TASC cells used for this research.

When exposed to the xenon arc lamp over an extended period and benchmarked against a reference solar cell the uncertainty of linearized photodiode measurements was found to

be less than 0.162% of the observed value across multiple observations. The actual variation in the output value of the photodiode across full data sets was found to remain stable to within $0.5mV$ indicating good long-term stability in the output of the arc lamp. In certain measurements the drift in the observed power is more severe, this is particularly common for measurements performed immediately after lamp-ignition, before the arc-lamp has been given adequate time to warm up and settle into a steady state. In Fig 4.5 the short circuit current measured at 0° of incidence is plotted against the observed photodiode response. The arc lamp output follows an exponential decay, suggesting that it is reaching thermal equilibrium; the response of the photodiode and the short circuit demonstrate a linear relationship, indicating that changes in the photodiode response may be used to normalize the cell output. If the arc lamp is left to settle for a period of 30 minutes or longer then the probability of observing this exponential decay in the source is greatly reduced and the resulting drift in lamp output is either insignificant or easily normalized through photodiode measurements. During regular performance testing the arc lamp was given a minimum of 30 minutes to settle, and the small resultant exponential decays were normalized through the photodiode measurements.

A F/1.5 condensing lens (Oriel Instruments) was used to produce a planar beam with a 33 mm diameter at the exit aperture. For an ideal point source and ideal lens this configuration would yield a perfectly flat collimated beam, however the actual beam of the Xenon

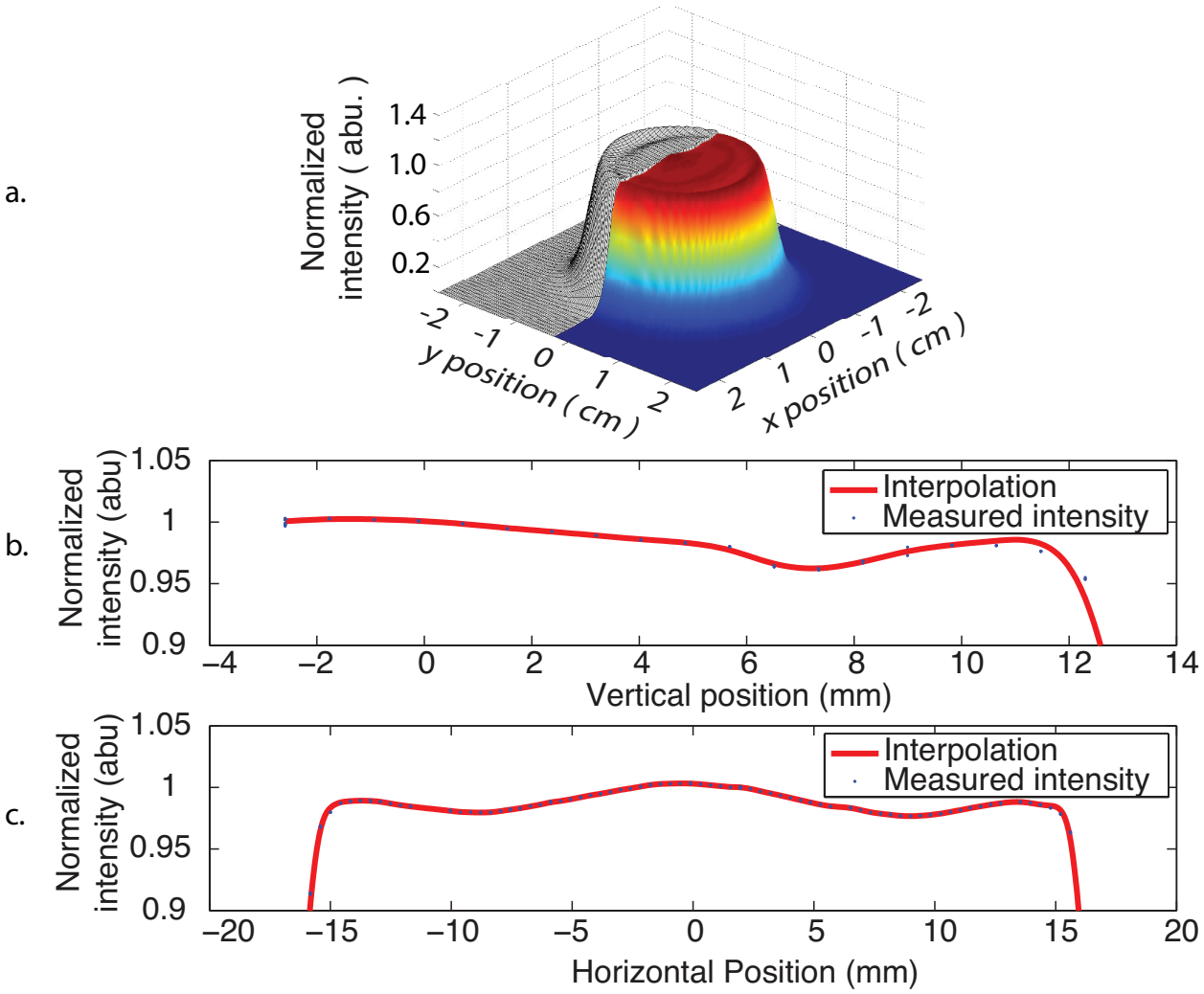

Fig. 4.6 (a) The composite beam profile in the X and Y axes demonstrating reasonable flatness in the illuminated region. 1-Dimensional profiles in the horizontal and vertical axis are shown in (b) and (c) respectively.

arc lamp is expected to exhibit deviations due to lens imperfection, imperfect positioning of the rear-reflector and bulb, and the fact that the plasma ball at the arc tip is not a perfect point source. In order to quantify these deviations the spatial variance of the output beam

was determined by translating the photodiode across the X and Y-axes of the beam profile and measuring the beam intensity. Flashed power measurements were performed at $0.5mm$ increments across the X and Y axes of the beam and periodic measurements of the beam strength at the center of the beam are used to account for and remove any long term drift in the power supply. Data from this profiling is shown in Fig 4.6 as well as the resultant composite beam profile in the X and Y axes. In the composite profile shown in Fig 4.6 nearly one third of the beam area is in grey, this is to indicate that this area was not profiled as the experimental setup lacked the dynamic range to measure the beam power at these heights. The lack of profiling in the grey region is not expected to affect the uncertainty in solar cell measurements, however, as the profiled region is highly uniform, and the rear-reflector ensures that the beam profile is symmetric. Furthermore only a small fraction of the lower cell will touch this region, hence the associated uncertainty is expected to be small. The individual X and Y profiles in Fig 4.6 are best fit to a composite of 5 Gaussian terms in order to build up the 3D composite profile. The variance in spatial intensity, combined with knowledge of the positional uncertainty of the cell and its incident angle gives the total uncertainty in the intensity of incident light.

4.1.3 Uncertainty Analysis: Alignment

Solar cells were soldered to a printed circuit board (PCB) and positioned in such a way that the total area of the cell was equally distributed on either side of the rotational axis of the PCB. The PCB was mounted to an upright stand and the rotational axis of the PCB was aligned with the rotational axis of the stage. A plastic chock was affixed to the rear of the PCB which was then pressed flush against the vertical walls of the upright-stand in order to ensure that the PCB placement was repeatable to high accuracy; likewise, the bottom of the PCB was placed flush against the floor of the upright-stand, ensuring repeatability in the vertical placement of the cells. The assumed misalignment uncertainty is $\sigma_x < 0.1mm$ in the horizontal plane, $\sigma_y < 0.1mm$ in the vertical with an added uncertainty of $\sigma_{axis} < 0.1mm$ in the position of the cells relative to the rotational axis. Rotational alignment of the PCB in order to define the initial position at normal incidence is achieved using the laser alignment system shown in Fig 4.1. The beam is directed at a flat mirror centered on the rotational axis of the PCB (see item 12 in Fig 4.2) and the reflected beam is imaged on $1mm$ ruled graph paper resulting in an uncertainty at the beam position of $0.5mm$; this corresponds to an angular uncertainty of $\sigma_\theta < 364\mu rad$ in the initial position of the rotation stage.

Provided these uncertainties in alignment and initial position of the cell we can determine the effect of this uncertainty on two relative measurements of the short-circuit current by using the beam intensity data shown in Fig 4.6. The fitted beam-profile is reproduced as a

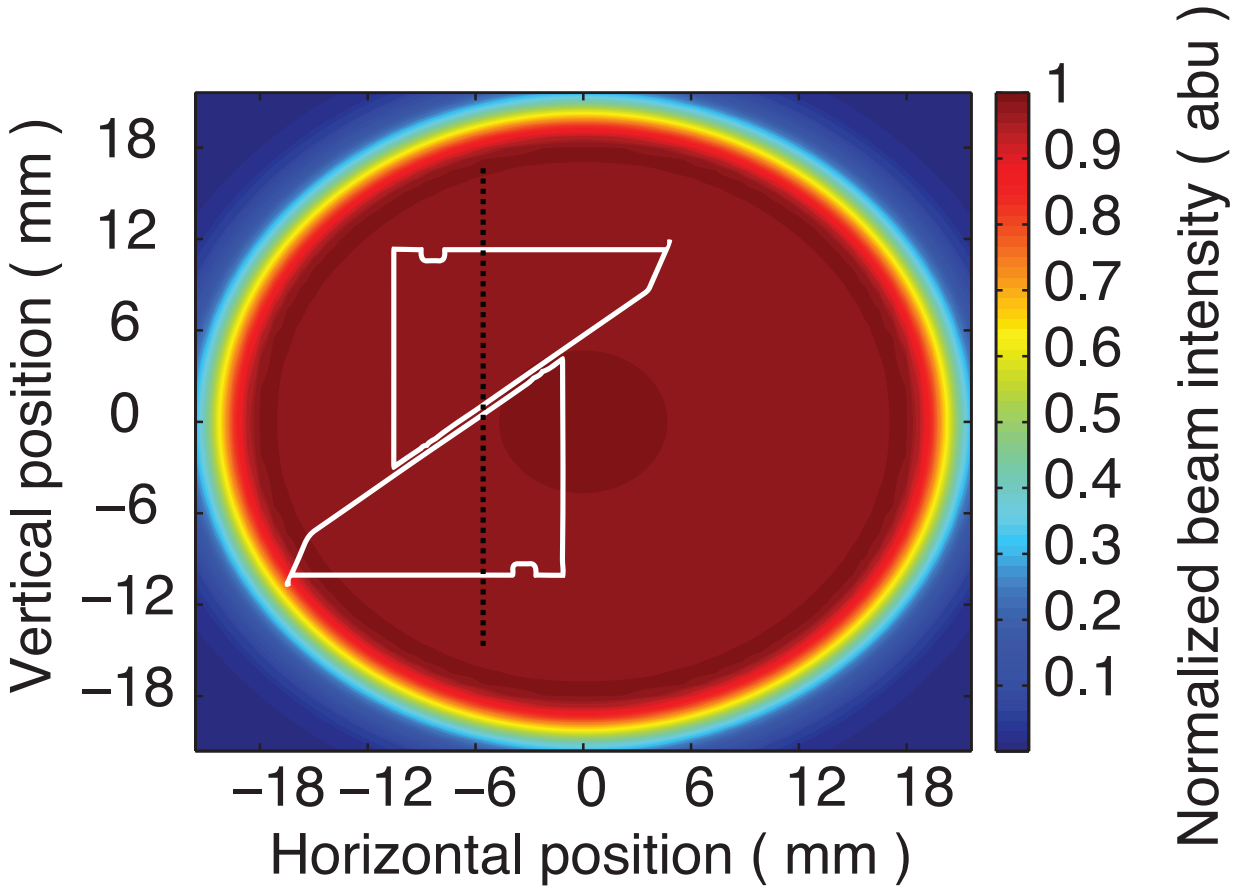

Fig. 4.7 Contour plot of beam power output in x and y. The projected surface area of two solar-cells are outlined in white. In order to fit both cells in the plot at once the cells are rotated by 60°; the rotational axis of the PCB is shown as a black dotted line. The cells are positioned to measure current from the top cell; hence, the top cell does not extend far into the lower half of the beam.

contour plot in Fig 4.7, and the projected surface areas of two TASC cells are outlined in white and overlaid onto the contour. The difference in radiant flux experienced during two different measurements with misalignment, $\sigma(\Delta x, \Delta y, \Delta\theta)$, may then be determined by integrating

over the beam profile (*i.e.* the irradiance) within the bounds of the two projected surface areas. I_{SC} is directly proportional to the radiant flux and since the spectral characteristics do not change it is expected that the uncertainty in transmittance will be given by the maximum relative difference between radiant flux values contained in the set of all misalignments for the domain $\{|\Delta x| < \sigma_x, |\Delta y| < \sigma_y, |\Delta\theta| < \sigma_\theta\}$.

4.1.4 Uncertainty Analysis: Circuit

The solar cell is connected in series with a digital ammeter (Agilent U2741A) which measures the short circuit current of the solar cell. The uncertainty in the measured value of short circuit current from the ammeter was dependent on the readout value, but typically came no higher than 0.385% of the readout value. The photodiode acting as power sensor is connected in series with a low pass noise filter and the voltage drop across a load resistor is measured to determine the photocurrent. The voltage drop across the load resistor is measured using a standard data acquisition device (National Instruments USB-6009 DAQ), the load resistance is chosen to maximize the inherent resolution of the DAQ device with respect to the voltage signal and the photodiode is forward biased at 5 V to ensure linearity in the response and avoid saturation.

Conventionally, measurements of the IV curve of a solar cell are performed using flashed measurements of durations $< 200ms$. Due to the ripple of the power supply and the slow

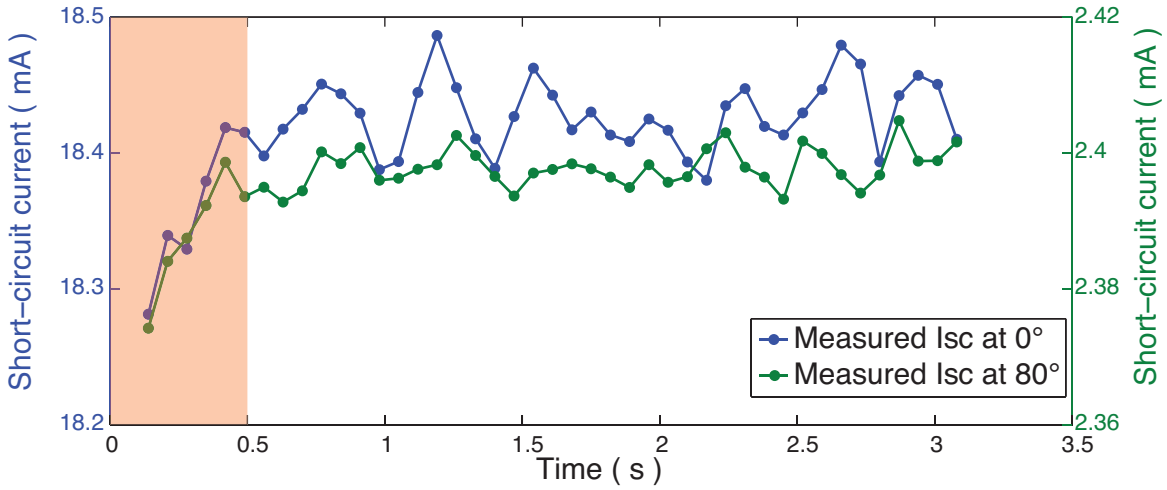

Fig. 4.8 A magnified, highlighted view of the RC lag present during wavefront detection at 0° and 80° of incidence for a bare solar-cell. The RC lag, which occurs during the first 0.5s of signal detection is highlighted in red; in both signals the magnitude of the change during the RC lag is $\sim 1\%$ of the steady-state value.

response speed of the current sensor it is necessary to perform flashed measurements on the order of 2 to 4 seconds in order to obtain useful data. The signals were detected as wavefronts, two of which are shown in Fig 4.8 where the RC-lag, is highlighted in red, is visible throughout the first half-second of signal detection. This RC component is likely a combination of the settling time of the digital ammeter in response to a step input, as well as some self-capacitance in the cell. In every measurement this RC component can be observed to occur with the same settling time and the same magnitude relative to the steady-state measurement of I_{SC}. Since the RC component is so highly repeatable, it is unlikely to affect any relative measurement between two observations. A set of wavefronts

including their leading edges are plotted in Fig 4.9, in which the RC components of the waveform are indistinguishable from the settled values. The presence of this RC component has some small implications for the uncertainty of I_{SC} in light of the observed effect on temperature. The RC-lag prevents accurate determination of the initial value of I_{SC} before any heating can occur, so the uncertainty on the initial value of the short circuit current I_0 will be increased by an amount equivalent to $t_{\mathrm{RC}} C_{\mathrm{I}} \frac{\Delta T}{\Delta t}$ where t_{RC} is the RC-lag time of the system. This contributes a total uncertainty of $\sigma_{\mathrm{RC}} = 0.316 \mu A$ which is effectively negligible.

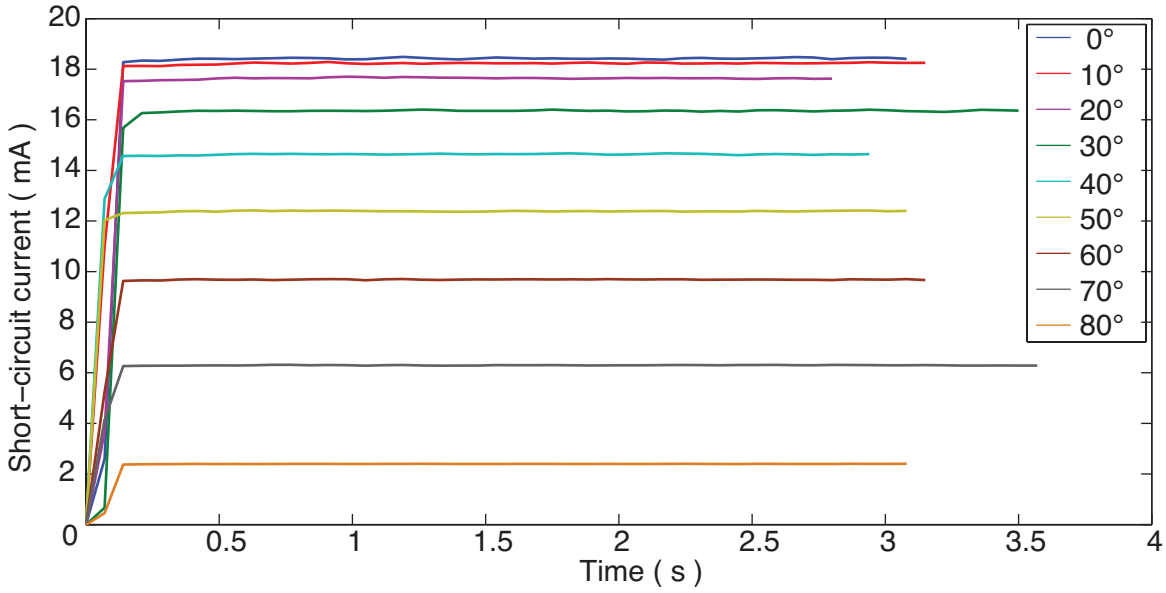

Fig. 4.9 An non-magnified view of 8 wavefronts, corresponding to a bare solar-cell, detected at varying angles of incidence from 0° to 80°. The initial time, $t = 0$ is defined as the time at which I_{SC} crosses from a negative to positive value.

As stated previously, I_{SC} is the ideal measurement parameter due to its direct relation-

ship to the maximal power output, $P_{\max}$. This relationship is described in Eq 2.10 in which η is the fill factor of the cell which is a measure of the efficiency equivalent to a parameter describing the "squareness" of the I-V curve in Fig 4.3. I_{SC} is also a useful measurement due to its direct relationship to the transmittance of the optical surface, hence by measuring the I_{SC} values before and after the application of MEAR coverglass it is possible to indirectly measure the increase in cell power-production relative to untreated glass. Furthermore I_{SC} is relatively insensitive to temperature, and if the appropriate steps are taken to ensure that the intensity of incident light is well-known then precise measurements may be performed in a relatively straightforward manner. To summarize, it is expected that measuring the short circuit current of the cell, I_{SC}, is sufficient to demonstrate increased power-production due to MEAR technology due to its relative insensitivity to temperature, as well as the direct relationships linking I_{SC}, $T_{\mathrm{MEAR}}(\theta)$ and the peak power of the cell, $P_{\max}$.

The uncertainties associated with each step of this procedure are summarized in Table 4.1. The values in the right hand column are determined by computing the variance in the transmission due to each parameter, z_i according to the equation:

$$\sigma^2 = \sum \sigma_i^2 \left(\frac{\partial V}{\partial z_i}\right)^2 \tag{4.4}$$

where V is the expression for short-circuit current developed in Eq 2.9. Taking the square root of Eq 4.1.4 and dividing by the short-circuit current yields the uncertainty as a percentage value of the short-circuit current. Given the relationship between $I_{SC}(\theta)$ and $T(\theta)$ from

Eq 4.1 the uncertainty expressed as a percentage value will translate between I_{SC} and T. Taking the vector sum of the subgroup uncertainties in Table 4.1 as a function of incidence angle yields increasing uncertainty values with respect to incident angle–as expected. These values are then propagated through the right hand side of Eq 4.1 according to Eq 4.1.4. The resultant mean values for uncertainty in terms of the power-enhancement are given explicitly in table 4.2; the range of uncertainty values away from the mean was less than 0.1% indicating that these mean values of uncertainty are a good estimate for overall levels of uncertainty.

4.2 Results of performance tests

SWAR surfaces were fabricated on quartz using the colloidal lithography and micromasking techniques as described in chapter 3. Ultimately two SWAR surfaces were tested: the first SWAR surface was fabricated using colloidal lithography and possessed a feature height of $350nm$ and average spacing of $130nm$, the second SWAR surface was produced using the single step micromasking-method and possessed an average feature height of $1177nm$ with spacing $134nm$. Mean uncertainties in the power-enhancement provided by application of SWAR surfaces is listed in Table 4.2; this table includes two significant figures but from this point onwards only one significant figure will be considered for these experimental results.

The uncertainties associated with this optical setup have been constrained as best as possible and the resulting measurements were both consistent and repeatable. It was not

Table 4.1 Sources of uncertainty in optical setup, the rightmost column refers to the uncertainty in a particular measurement as a percentage of the value of that measurement; the column immediately adjacent refers to the physical value of that uncertainty. The table is separated into four parts representing the major subgroups of uncertainty and the vector magnitude of each subgroup is in bold. The subgroups are current readout, beam power, and misalignment; the misalignment subgroup is shown at 0° and 85° to highlight the increase in uncertainty at high angles of incidence.

Parameter	**Symbol**	**Uncertainty in parameter**	**Uncertainty as %**
	Temperature		
Measured I_{SC}	σI_{SC}	$0.0006 \cdot I_{\mathrm{SC}} + 1.5\mu A$	< 0.385
Heating during RC	σI_{RC}	$0.316\mu A$	0.001
Regular heating	σI_{T}	$1.65\mu A$	0.007
Current readout	σI_{SC}	$0.00432mA$	**0.385**
	Beam power		
Photodiode readout (linearized)	σV_{FDS}	$0.25mV$	0.161
Load resistance	σR_L	4.82Ω	0.003
Beam power	$\sigma \beta_{\mathrm{Xe}}$	..	**0.161**
	Misalignment at 0°		
Cell-axis at 0°	σx_R	$0.1mm$	0.484
PCB-X at 0°	σx_0	$0.1mm$	0.489
PCB-Y at 0°	σy_0	$0.1mm$	0.006
Incident angle at 0°	$\sigma \theta_0$	$364\mu rad$	0.00002
Positional uncertainty	σdA	..	**0.688**
	Misalignment at 85°		
Cell-axis at 85°	σx_R	$0.1mm$	0.004
PCB-X at 85°	σx_{85}	$0.1mm$	0.036
PCB-Y at 85°	σy_{85}	$0.1mm$	0.006
Incident angle at 85°	$\sigma \theta_{85}$	$364\mu rad$	0.832
Positional uncertainty	σdA	..	**0.833**
Overall uncertainty in $T(\theta)$	σT_θ		**.093%**

SWAR height	**Mean $3-\sigma$ uncertainty**
350nm	2.1%
1177nm	1.9%

Table 4.2 Mean uncertainties on relative transmittance between SWAR and glass surfaces for the 350nm tall and 1177nm tall surfaces calculated by propagation of Eq 4.1 through the expression for variance in Eq 4.1.4. These uncertainties are given as values of relative transmittance or, equivalently, power enhancement. A quoted value of power production enhancement of 5% with an uncertainty of 3% would indicate that the level of enhancement is somewhere between 2% and 8%.

possible to fully constrain the system, and as such a few unknowns remain which may contribute to systematic errors in the measurements. Firstly, when calculating the radiant flux seen by the cell it is assumed that the cell is equally efficient across the entire cell. This is unlikely to be the case, as the TASC solar cells have been clipped multiple times resulting in higher overall surface recombination rates near the edges of the cell. It is more likely that the cell is biased towards efficient collection on the wider side of the triangle, however this effect is unlikely to account for significant deviations from the norm. Light emanating from the arc-lamp is assumed to be unpolarized, and the effects of the Xenon-emission lines in comparison to the broadband operation of the cell are expected to be small. Data was collected over multiple weeks, hence the ambient temperature of the room was seen to fluctuate by up to two degrees, however as Fig 4.4 demonstrates, the effect of these fluctuations will be negligible.

The variations that were observed in the short-circuit current are therefore determined

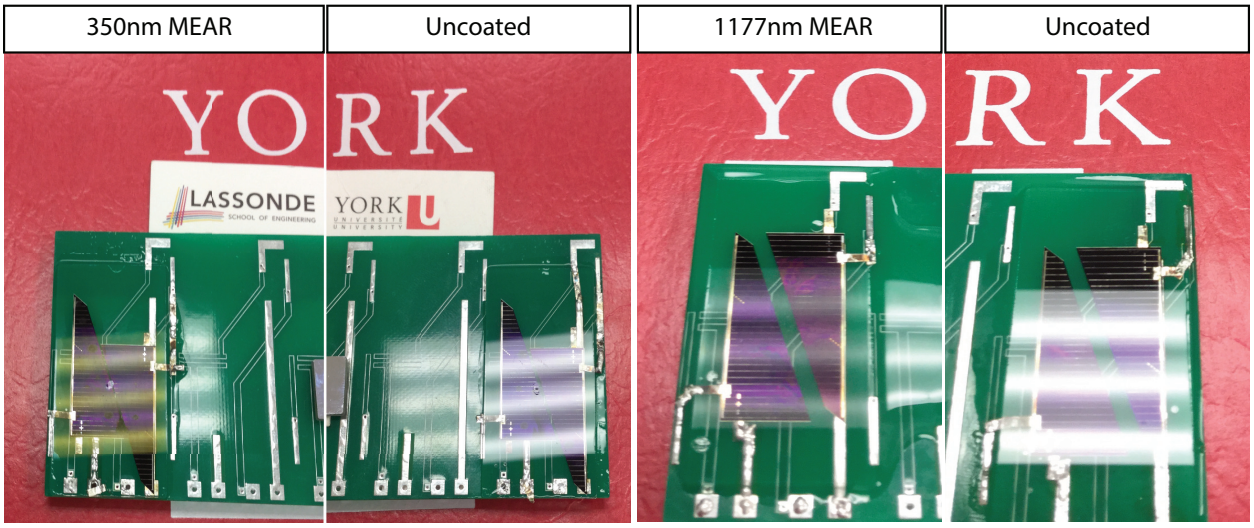

Fig. 4.10 From left to right: photograph of the 350nm SWAR enhanced coverglass on the test PCB, uncoated coverglass to be compared to the 350nm SWAR glass, 1177nm SWAR enhanced coverglass fabricated by single-step maskless etching, uncoated coverglass for comparison.

to be a consequence of an increase in the transmittance of the overall system. The additional fact that the SWAR effect can be verified by the naked eye produces a high degree of confidence that the SWAR surfaces are exhibiting the expected behaviour. However, high confidence that the SWAR effect has been demonstrated does not extend to high confidence in the precision to which the SWAR effect may be constrained. This experimental setup was designed to be sufficient to definitively confirm the presence of SWAR in an optical system, as well as to verify that SWAR is an effective means for increasing power-production at high angles of incidence. This setup is not designed to produce high-precision estimates of the performance characteristics of a SWAR surface–hence the regression to a single significant

digit when discussing expected on-orbit performance of SWAR surfaces.

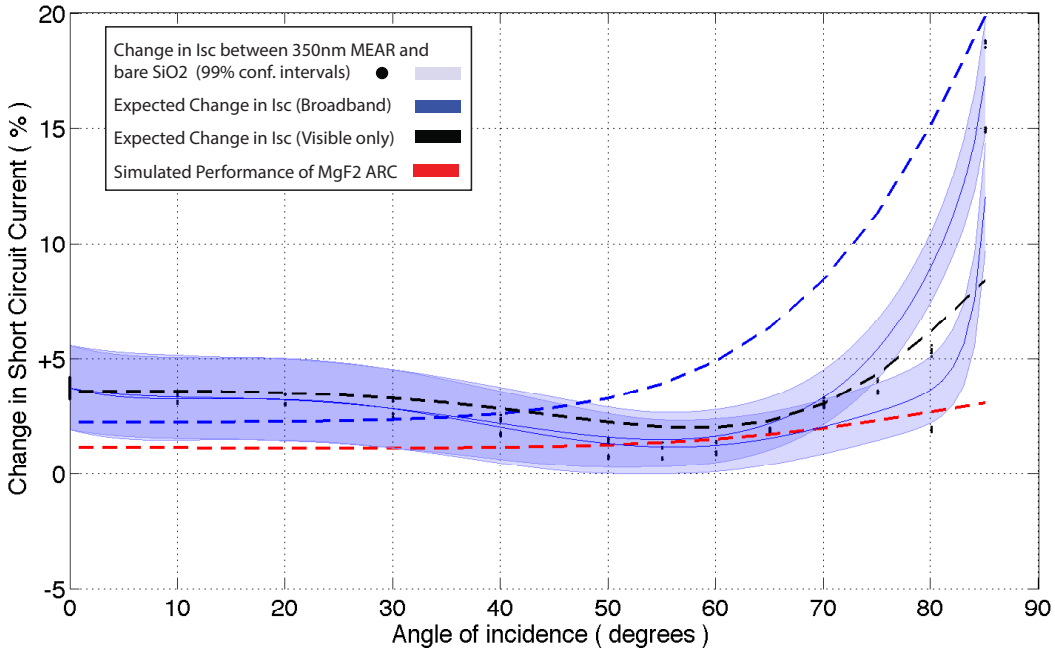

Fig. 4.11 Experimental data showing the observed performance-enhancement due to the application of $350nm$ tall SWAR structures. Two shaded regions represent the 3σ uncertainty surrounding curves fit to the data. A red dashed line indicates RCWA-computed enhancement due to a $\lambda/4$ coating. A dashed blue line shows the RCWA-computed performance of a $350nm$ tall MEAR surface, without compensating for IR effects. A dashed black line shows the RCWA-computed performance of the $350nm$ MEAR surface if only visible components experience MEAR-enhancement–which agrees with measured data. In this plot, the enhancement due to a bare SiO_2 surface relative to itself would be a line across 0.

The $350nm$ and $1177nm$ SWAR surfaces were bonded to two cell solar arrays as shown

in Fig 4.10. The effect of SWAR texturing on the surfaces is immediately apparent from the colour tuning visible in the reflected light. The $350nm$ shows viewed at normal incidence the predominant maxima of reflectance occur in the blue and near-red portions of the visual spectrum, resulting in distinct blue and yellow colour tuning of reflected white light. At high angles of incidence the reflectance shifts strongly to reflect blue light only. This is expected, as the blue light reflectance is a function of spacing, not height and the blue light is expected to come very near to the boundary of the subwavelength regime at higher angles of incidence. The $1177nm$ structures show reflectance only in blue wavelengths of light, indicating that the reflectance peak that occurred in the the yellow-red regime for the $350nm$ features has moved to the near infrared where it cannot be imaged with conventional optics. This is entirely in line with the theoretical observations regarding the height of SWG AR features as denoted in chapter 2. On each PCB, four cells were mounted two of which would receive SWAR-enhanced glass and one which would received untreated glass. Ideally this arrangement will yield four different functions for power-enhancement as a function of incidence angle. Unfortunately, small pockets of air became trapped under some cells when they were first soldered to the PCB; during application of the coverglass these pockets rose through the gel and sat underneath the glass, distorting the transmission of light. In both trials the data from one of the four cells needed to be discarded due to air-bubble effects–yielding a total of two experimental curves per surface trial rather than four.

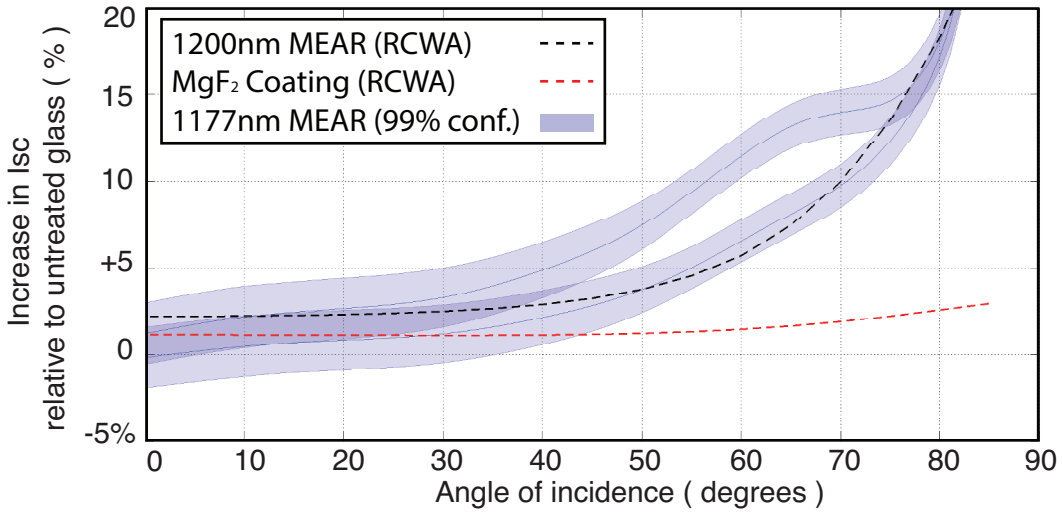

Fig. 4.12 Experimental data showing the performance-enhancement on a TASC solar cell for coverglass enhanced by 1177nm tall SWAR structures relative to a bare SiO_2 substrate. Two shaded regions represent the $3-\sigma$ uncertainty regions surrounding curves fit to the data. A red dashed line shows the RCWA-computed performance enhancement expected from application of a $\lambda/4$ coating. A blue dashed line shows the RCWA-computed performance of a 1200nm tall MEAR structure, which agrees with the measured data for one of the 1177nm SWAR curves.

The short circuit current performance of the SWAR surfaces relative to bare quartz were evaluated in averaged measurements performed in increments of 10° from 0° to 50° and in increments of 5° thereafter up to 85°. Measurements were not performed at incidence angles greater than 85° due to the explosive growth in measurement uncertainty related to rotational misalignment at incidence angles $\theta > 85°$. The relative increase in the short circuit current after the application of the 350nm SWAR surface are plotted in Fig 4.11 along with

expected values from RCWA simulations of the MEAR surface. The performance data for the $1177nm$ surface and its theoretical values are similarly plotted in Fig 4.12. Both figures show power-production relative to an untreated substrate, and the simulated performance of commercially available $\lambda/4$ AR coated glass relative to untreated glass is also shown for the purpose of comparison. In Fig 4.11 and Fig 4.12 unchanged performance with respect to untreated glass would appear as a horizontal line at 0%.

As expected, both SWAR-enhanced substrates showed improved transmission at high angles of incidence resulting in greater overall power-production; these results are consistent with results from the RCWA simulations with some minor variations. One notable difference between the simulated results and experimental data for the $350nm$ SWAR surface is that the minimal increase in performance occurred at an incidence angle of approximately $55.4°$ rather than at normal incidence. This discontinuity between the expected and experimental results is a result of poor consideration of the Brewster angle effect [71]. As discussed in chapter 2, perfect antireflection from a GRIN region requires all phases of the incident light to be present in the GRIN region simultaneously; this is equivalent to the statement: the depth of the GRIN region must be greater than 0.4λ. For wavelengths where $h < 0.4\lambda$ perfect antireflection is not achieved and the values of reflectance will be more in-line with that of an uncoated surface. This requirement implies that for wavelengths longer than $875nm$ the antireflective properties should be similar to untreated glass with residual differences arising

from the fact that SWAR structures have highly-suppressed Brewster-angle effects [71].

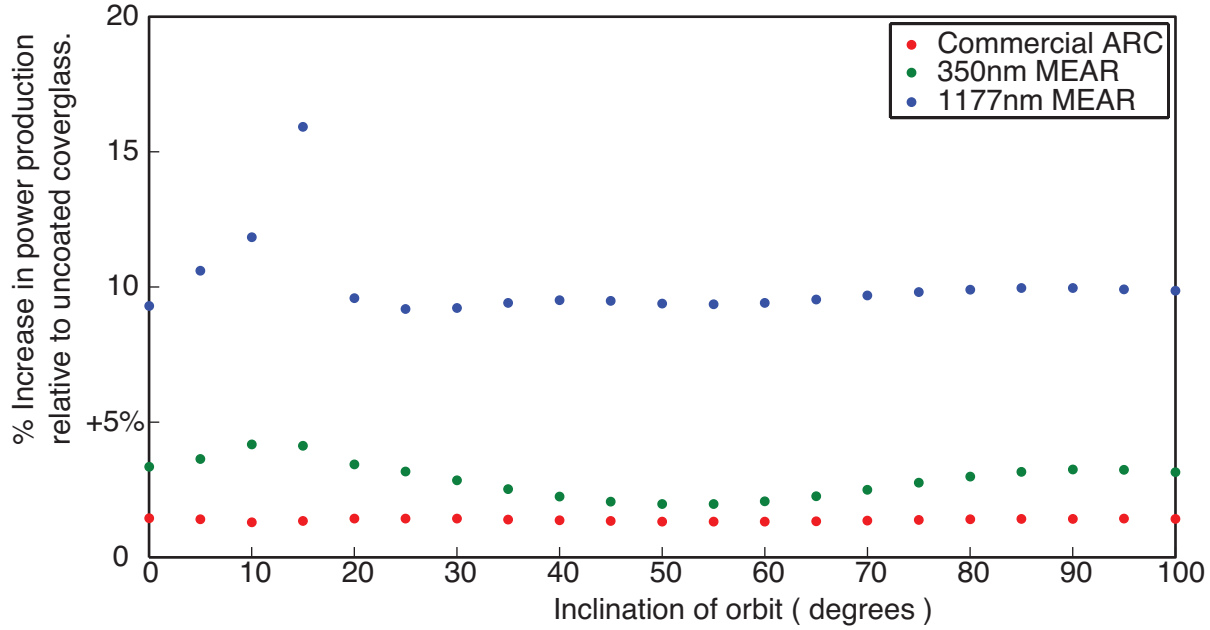

Fig. 4.13 Re-calculated values for expected power output over orbit in orbital inclinations from 0° to 85°. Theoretical values were originally presented in Fig 2.9, this plot uses the experimental presented in Fig 4.11 and Fig 4.12. The uncertainties associated with these values will be similar to the values quoted in Table 4.2.

The Brewster-angle effect arises from the photo-excitation of oscillations of bound electrons at the interface of the two media, in fact these oscillations are the mechanism driving reflection in the first place. Bound electrons at the interface of the surface media may be thought of as electric dipoles that will align their dipole vectors with the polarization vector of the incoming light and oscillate along that vector. It is the oscillation of these dipoles that

excites the time varying **E** field of the reflected wave. Incoming light may then be polarized in such a way that the axis of the oscillating dipole will become aligned with the direction of propagation for the reflected ray. As light is a transverse electric wave and not a longitudinal wave it is impossible for a dipole oscillating along the direction of travel to excite a wave, hence the intensity of the reflected component for this particular polarization falls to zero. At the surface of a moth-eye structure, however, the surface dipoles are highly disordered and precise alignment of these dipoles is not possible; because of this, the Brewster effect is highly suppressed in SWAR structures [71]. In Fig 4.11 this is precisely what occurs. The SWAR effect for this short structure strongly attenuates the reflection of visible light, however the reduction of reflection through the Brewster effect in long-wavelength, low-energy infrared photons is also eliminated. Non-Brewster reflection in the infrared is more or less unchanged as a result of the SWAR structuring. The overall effect in Fig 4.11 is to temper the observed SWAR effect, particularly at $\theta = 55.4°$ through reduced reflectance of long wavelengths in the bare SiO_2-covered cell that is not matched by the SWAR-effect. This is borne out by the expanded RCWA simulation results plotted in fig 4.11, in which it can be seen that by considering MEAR antireflection in only the visible components of light the RCWA results are made to agree with the experimental data.

Based on this theoretical framework it is expected that Brewster-like features in the incidence curves will be eliminated as the height of the etched structures increases. As the

height of the structures increases, destructive interference in the IR wavelengths can occur, and the loss of the Brewster-angle effect will be offset by SWAR. In Fig 4.12 this is seen to be the case as the SWAR-enhanced performance produced by the $1177nm$ structures improved dramatically from that of the $350nm$ structures, showing good agreement with the predictions of the broadband RCWA simulation. The $1177nm$ structures show a remarkable increase in power-production over untreated glass, reaching levels of improvement greater than 15% at angles of incidence above 70°. In addition, RCWA simulations of a commercial $110nmMgF_2$ $\lambda/4$ AR coating indicate that the optimal SWAR structure demonstrates similar performance at normal incidence, and improved performance at all angles of incidence $\theta >$ 45°. One of the two experimental curves shown in Fig 4.12 diverges quite sharply from the values predicted by RCWA; it is possible that this is due to a misalignment outside of the scope of the error budget. The optical setup does provides for a high degree of repeatability, however as has been previously noted the adhesion of glass is a non-reversible process. Any un-diagnosed errors in the measurements of the bare cell, either due to misalignment or to stray light cannot be re-investigated once the glass layer has been adhered.

Though a useful measure of performance, incidence curves such as Fig 4.12 are not an intuitive method for evaluating SWAR performance. Thankfully, these curves can be used in conjunction with satellite attitude control data, as described in chapter 2 to determine the impact of SWAR technology on satellite power budgets. Attitude data for a 3-U CubeSat orbiting at 750 km in the nadir pointing configuration was simulated for orbital inclinations

Table 4.3 Simulated increase in power-budget over 7 month orbit.

Orbit	**Attitude**	**Mean**	**Maximum**	**Minimum**
		MEAR Surfaces		
A-Train	Nadir	5%	5%	5%
Iridium	Nadir	4%	6%	4%
ISS	Nadir	5%	6%	4%
A-Train	Dart	7.0%	8%	6%
Iridium	Dart	6%	10%	4%
ISS	Dart	6%	12%	4%
		$\lambda/4$ MgF_2 *ARC*		
A-Train	Nadir	1.2%	1.2%	1.2%
Iridium	Nadir	1.2%	1.3%	1.2%
ISS	Nadir	1.2%	1.3%	1.2%
A-Train	Dart	1.2%	1.3%	1.2%
Iridium	Dart	1.2%	1.4%	1.2%
ISS	Dart	1.3%	1.5%	1.2%

The three-sigma experimental uncertainty associated with these SWAR values is ±2%, *i.e.* a CubeSat in the A-Train Nadir configuration is expected receive a power-production enhancement between 3% and 7%. The performance by a $\lambda/4$ is evaluated through RCWA, and an extra significant digit is kept in order to demonstrate the uniformity of the coating performance relative to the SWAR surface.

from 0° to 100° and the curves in Fig 4.11 and Fig 4.12 were applied to determine the expected increase in power generation. The results of this simulation are shown in Fig 4.13, this analysis demonstrates that the application of a $350nm$ SWAR surface to this type of satellite would result in an average increase in power-production of 3% with some significant variance depending on the orbital parameters of the satellite. For a $1176nm$ SWAR surface,

the mean expected increase in power-production rises to 10%, whereas the commercial AR coating provides a mere 1.4% improvement over untreated SiO_2.

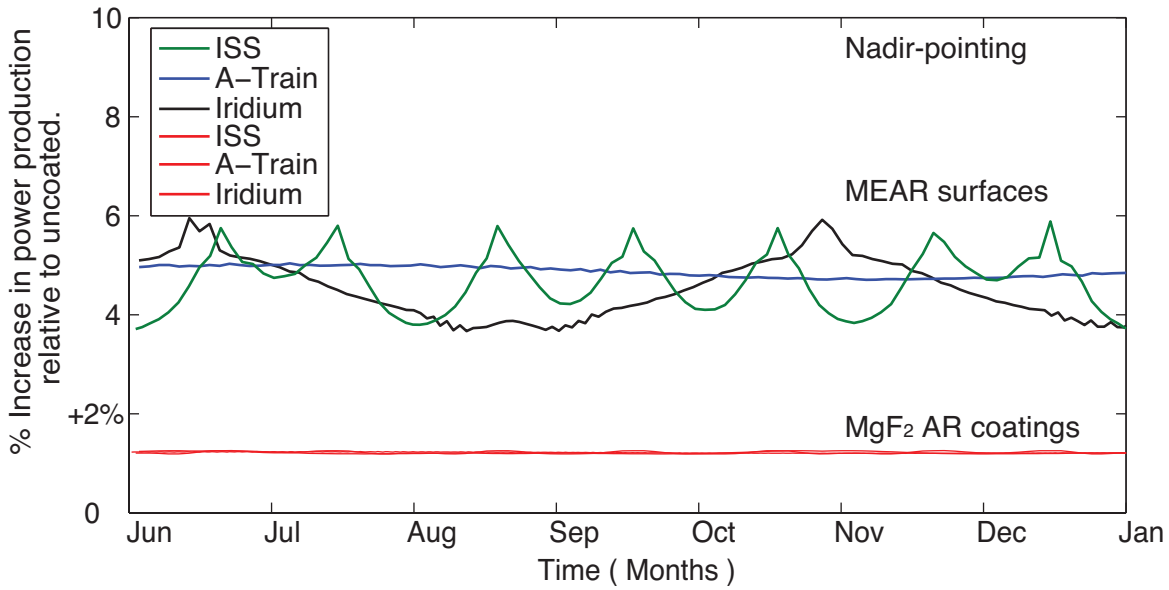

Fig. 4.14 Long-term attitude simulation for nadir-pointing CubeSats showing the effects of nodal precession on power enhancement for a $1177nm$ SWAR surface and $\lambda/4$ MgF_2 ARC.

The simulated results presented in Fig 4.13 are of limited use as the initial simulation time was only for one week of attitude data. Typical CubeSat missions are intended to operate for months or years, in which case the effect of nodal precession must be taken into account. Over the course of a full year nodal precession will cause the orientation of the orbital plane to change with respect to the sun, which will have implications for the incidence angles observed by the CubeSat. In addition it is more useful to simulate the

effect of MEAR enhancement over particularly popular orbits, as it is rare that CubeSat developers choose the orbit at which they operate. To this end, orbital data is simulated for three LEO orbits that a CubeSat might occupy: the "A-train" constellation track, an Iridium track orbit, and the ISS orbital track. The A-train track is used as a representative orbit for the popular noon-midnight sun-synchronous orbit, which would be a uniquely challenging orbit for a CubeSat to occupy due to the low light levels. The Iridium orbit is chosen as a stand-in orbit for LEO communication satellites, which are launched frequently and provide ready opportunities for CubeSat ride-along missions. Finally, the ISS orbital track is chosen in recognition of the fact that the ISS is increasingly being used as a launch platform for CubeSats. Orbital simulations are carried out over a period of seven months in order to guarantee a number of full precessions. Two different attitude configurations are considered: nadir-pointing and the so-called "dart" configuration in which the long axis of a 3-U CubeSat is directed along the orbital track. In both simulations the $1177nm$ SWAR surface was used, and the attitude incorporates a sun-vector constraint, *i.e.* the satellite is rotated about the pointing-axis in order to minimize incidence angles. The results of these simulations for nadir-pointing CubeSats are shown graphically in Fig 4.14. The results of a second simulation in the dart configuration are shown in Fig 4.15; the results of both simulations are summarized in Table 4.3.

In the nadir-pointing configuration (Fig 4.14) the long-term simulation revealed a stable

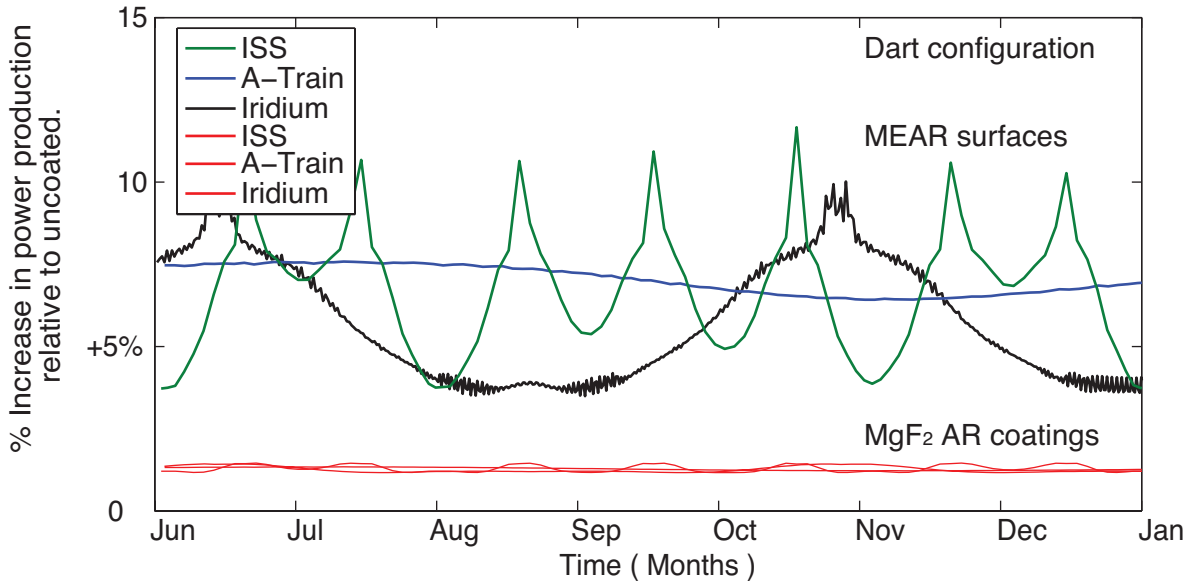

Fig. 4.15 Long-term attitude simulation for CubeSats in the dart configuration showing the effects of nodal precession on power enhancement for a $1177nm$ SWAR surface and $\lambda/4$ MgF_2 ARC.

increase in performance for the $1177nm$ SWAR surface on the order of 5% with an associated three-sigma uncertainty of $\pm 2\%$ due to experimental limitations. The A-train orbit showed very little change, as would be expected for a sun-synchronous orbit, however the Iridium and ISS orbits show fairly significant swings in performance as the orbital plane rotates with respect to the sun. These performance swings may be understood to be a consequence of the increase performance of the SWAR surface at high angles of incidence as seen in Fig 4.12. Higher angles of incidence are seen as the orbital plane precesses, which adds weight to the right hand side of the curve in Fig 4.12. It should be noted at this point that higher degrees of enhancement correspond to periods of lower overall power, as the overall amount of

power produced during periods of high incidence will still decrease with the cosine law. The variability of the SWAR surface is contrasted by the relatively steady performance expected from the MgF_2 $\lambda/4$ coating, indicating that the MgF_2 coating will not be able to provide a significant power "boost" in low-light conditions. In Fig 4.15 the overall level of power enhancement is slightly greater indicating that CubeSats in the dart configuration experience greater angles of incidence, and benefit more from the SWAR effect. The effect of the MgF_2 coating is also more variable in the dart configuration, however it is still uniformly less than the SWAR surface.

These results demonstrate that SWAR surfaces can be expected to provide a baseline increase in power-production of approximately 5% over orbit. For example, the SIGMA CubeSat operated in partnership between York University and Kyung-Hee University is a 3-U CubeSat in an Iridium-like orbit operating in the nadir-pointing configuration. Using Table 4.3 it is possible to estimate that the application of an $1177nm$ SWAR surface would increase its power budget by 4%. SIGMA's total power budget is expected to be $4059mW$, therefore the application of a SWAR surface is expected to produce an extra $160mW$ of power with an associated uncertainty of $\pm 80mW$. Comparatively, a traditional $\lambda/4$ MgF_2 coating would be expected to produce only $50mW$. Furthermore, Fig 4.15 shows that in low-power situations the SWAR effect is strongly increased. This "boost" effect would be useful for satellites interested in performing extended scientific observations at high angles

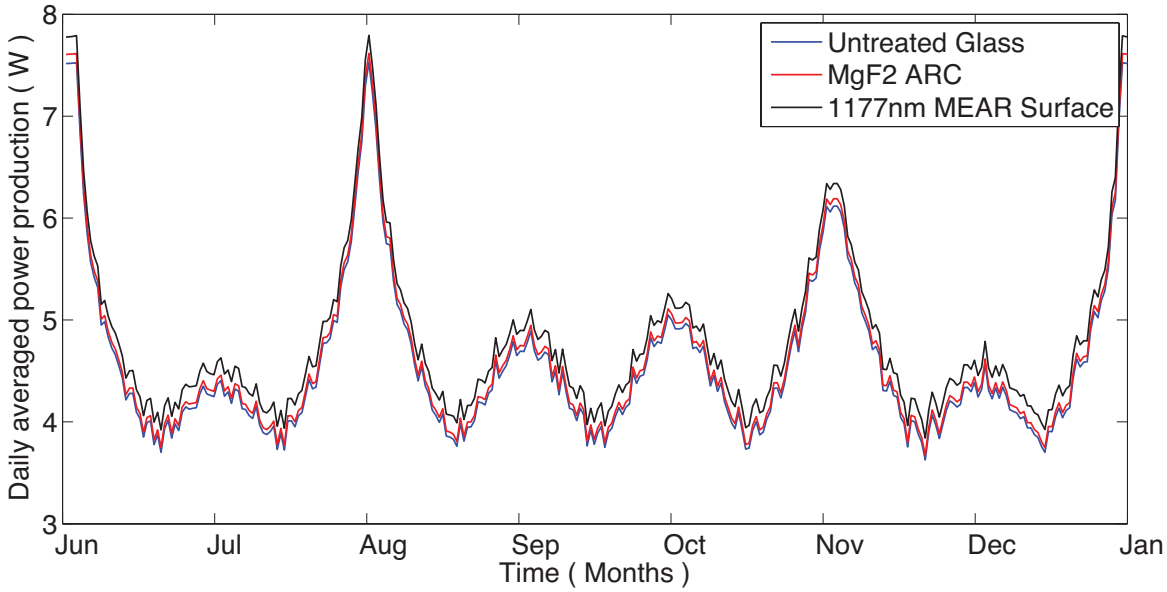

Fig. 4.16 Long-term attitude simulation of Nadir-pointing CubeSat launched from the ISS showing daily-averaged power generation for uncoated, $\lambda/4$ AR coating, and $1177nm$ SWAR surface.

of incidence, or for maximizing power-generation during daylight in a noon-midnight orbit.

This analysis is extended for the specific case of an Earth-observing 3-U CubeSat that has been launched from the ISS–similar to Dove 1 and Dove 2. It is assumed that solar panels cover the full surface area of the satellite, with the exception of the 1-U panel facing the earth, which is assumed to host payload. The panels in question were assumed to be off the shelf panels purchased from Clyde Space, providing power output of $7.29W$ for the 3-U side and $2.08W$ for the 1-U at normal incidence. Fig 4.16 shows averaged daily power-production

as a function of time over 7 months of simulated orbit time for bare coverglass, a conventional $\lambda/4$ AR coating, and the $1177nm$ MEAR surface. Throughout this time it was found that the MEAR surface increased daily average power output by $4W \cdot h/day$ over the $\lambda/4$ ARC. Excess daily power output increased during periods of low illumination, such as the interval between mid June and July. Meaning that throughout low-power periods, in which overall power output decreased, the excess power produced by the MEAR surface stayed constant. In the mid-June to mid-July period the MEAR surface produced $4W \cdot h/day$ more power than the $\lambda/4$ AR coating. This serves to demonstrate the primary benefits of MEAR surfaces on CubeSats: increased power generation across the board, and markedly improved performance at high angles of incidence in order to mitigate power loss during low-light operations.

5 Discussion and Conclusions

5.1 MEAR Surfaces for CubeSats

Increasingly nanosatellites and CubeSats in particular are being used for scientific and commercial purposes, rather than as technical demonstrations and educational tools. Redefining mission success and mission objectives beyond the classic "beepsat" mission places more stringent requirements on all satellite subsystems. In particular, scientific missions require precise attitude control during data acquisition, implying heavy power-draw from both the payload instrument and ACS simultaneously. Moreover, during observations the desired attitude of the satellite will be determined by the position of the target, resulting in sub-optimal positioning with respect to the sun. Increased demand for scientific missions as well as the desire for high-quality data products therefore implies the need for greater power generation and power storage capabilities for CubeSats. Unfortunately, the fundamental constraints of the CubeSat platform are weight and volume; these severely limit ACS capabilities, which are necessarily large and heavy subsystems. The use of flexible structures such as solar arrays are highly destabilizing from a controls standpoint, and are expected to

place additional demands on the capabilities of the ACS.

Hence, a CubeSat interested in performing scientific observations must necessarily employ a large and power-hungry ACS, and will often operate at high angles of incidence from the sun. Furthermore scientific satellites are limited in their ability to deploy large solar arrays for increased power generation, as this will place further demands on the attitude control system and potentially reduce the scientific capabilities of the satellite. A partial solution to this problem is to increase the effectiveness of solar cells at high angles of incidence to the sun in an effort to increase the amount of power-produced without altering the form factor of the satellite. In this research it has been demonstrated that SWAR and MEAR surfaces are capable of increasing the output power of solar cells by $\sim 5\%$, over their current values. While this may not seem to be a significant improvement at first glance it is significant when considered in the context of triple-junction solar cells as a mature technology. In the past 10 years the base efficiency of triple-junction concentrator solar cells has increased from 32% in 2000, to 44% in 2014, an increase in base efficiency of roughly 1% per year. Non-concentrated triple-junction cells for space applications, meanwhile, have remained roughly static at 30%. The impact of SWAR surfaces applied to the coverglass is roughly equivalent to a 1.5% increase in the base efficiency of the underlying cell–a significant improvement in this field. SWAR surfaces also possess the advantage of non-invasive post-process fabrication, meaning that they may be applied to any cell–and-coverglass system regardless of the underlying cell.

In addition, the use of SWAR surfaces does not preclude the use of solar arrays, and in fact would improve the performance of solar arrays as well. CubeSats already employ coverglass layers in order to protect cells from UV damage, the application of SWAR surfaces to these layers adds no new components, mass, or volume to the overall system while still providing an increase to overall power-production.

This research does not intend to suggest that SWAR surfaces are the only possible avenue to solving the power-production problem for scientific CubeSats. Solar arrays, increased energy storage capacity, and more efficient base cells are all valuable areas of research in the ongoing journey towards performing high-quality science using the CubeSat platform. The major advantage of SWAR technology, however, is that it is low impact and cross-platform. The SWAR-effect will increase power-production by 5% over orbit, it will not increase the mass nor the volume of the satellite and will not place additional demands on the ACS. Furthermore, as the SWAR effect does not preclude the use of solar arrays or high-efficiency cells, any subsequent increases in power-production through alternate means will be compounded by the SWAR effect. The sum total of these results, then, indicate that SWAR surfaces are a highly promising technology for space application and that further investigation into their use in the space environment is warranted.

5.2 Design and Fabrication Methods

A theoretical treatment of subwavelength antireflection (SWAR) was presented in chapter 2 and the practicalities and design rules of SWAR fabrication were discussed. RCWA and EMT-TMM simulations were carried out in order to investigate the effect of altering design parameters and the optimal feature height for space application was determined to be $1204nm$. A method was presented to couple the results of RCWA simulations to satellite attitude data in order to determine the effect of MEAR-enhanced coverglass on space-bound solar cells. Two different SWAR surfaces with similar characteristics were then fabricated using ICP-RIE techniques and RCWA simulations of the MEAR surfaces were shown to compare well with experimentally determined transmittance for SWAR-enhanced glass.

The fabrication of MEAR and SWAR surfaces remains an obstacle to their widespread adoption. There has been some success in recent years in streamlining the fabrication process through the use of curable photoresists [72–74], however these approaches are all unsuitable for space application. SWAR and MEAR surfaces for the space environment will experience a harsher thermal environment than those intended for ground application, hence they must be fabricated in such a way as to remain robust in the face of thermal cycling. It is outside the scope of this research to examine the impact of thermal cycling on SWAR structures, however work performed by outside groups has demonstrated that MEAR structures fabricated through top-down approaches are expected to hold up well to the thermal environment

of space [33, 75].

The major threat to SWAR surfaces in the space environment is degradation through exposure to atomic oxygen (AO); this effect is so severe, and AO so chemically corrosive, as to completely preclude MEAR or SWAR structure fabrication using curable resists. If SWAR surfaces are to be deployed in the space-environment, then, an effective top-down fabrication method for SWAR structures must be developed. Top-down fabrication of SWAR surfaces on an SiO_2 substrate is expected to minimize or even eliminate AO degradation of the structures as SWAR structures fabricated from SiO_2 are chemically inert to AO. In the absence of chemical etching, AO degradation is expected to take the form of physical sputtering of the surface; this effect is unlikely to be significant given the low bombardment energy of oxygen atoms in LEO. The bombardment energy of AO species is between $4.2eV$ and $4.5eV$ whereas the $Si - O$ bond energy is $4.7eV$. In the past it has been demonstrated that RIE and ICP etching systems are capable of generating plasmas with similar bombardment energies to AO in LEO. The primary challenge is in generating plasmas of sufficient density to simulate the LEO environment. Atomic oxygen erosion simulations are not in the scope of this research, however any future work on SWAR surfaces for space applications would do well to consider the use of ICP-RIE equipment to test for survivability.

It is unlikely that bottom-up fabrication processes employing curable polymers would be

stable in the space environment; chemical etching by AO would remove PMMA-moulded SWAR structures within a matter of days. A bottom-up process employing oxidized, AO-resistant materials with refractive indexes greater than SiO_2 could be used to produce a GRIN region by appropriately limiting the maximum fill-factor of the SWAR structures. This approach would require a multi-step fabrication procedure, implying low-throughput and high production-costs. A multi-step fabrication process would not be out of the question for a scientific payload; for solar-cells, however, a more convenient fabrication procedure capable of delivering AO-resistant SWAR structures is preferred. Two top-down approaches were investigated in this research: colloidal lithography and micromasking. Colloidal lithography has been widely reported in the literature and is a simple, repeatable process that may be performed even by relatively unskilled technicians. Etch masks were prepared using various types of polystyrene nanoparticles that self-assembled at the liquid-air interface of a DI water bath. Various deposition techniques were attempted and simple lift-off techniques were found to produce adequate results for subsequent etch processes. Once assembled into hexagonally close-packed monolayers the nanoparticles could be used as etch masks for RIE etching in a CF_{x} based plasma. Gaps were introduced into the etch mask by brief exposure to O_2 plasma under RIE conditions, allowing for precise control of SWAR structure spacing. A variety of RIE processes were carried out with different gas mixtures, bombardment energies and pressures. Ultimately the selectivity of the PS nanospheres proved to be too poor to produce traditional highly-arranged MEAR surfaces with the desired feature heights. In

fact, no groups have achieved success in demonstrating the preferred aspect-ratio of 9 : 1 through directly etching SiO_2 with PS etch masks. This is not surprising as colloidal lithography was initially demonstrated for pure Si etching, which has higher selectivity than SiO_2. Multi-step processes using colloidal lithography have been demonstrated to produce superior results than direct etching with a PS mask [27]. Multi-step process have inherently lower throughput and higher cost, however, future work would do well to continue to consider these approaches over direct etching with PS nanospheres.

More interestingly, it was found that SWAR structures could be produced through a single-step, maskless etch process. This maskless fabrication approach utilizes self-masking of the substrate through random deposition of fluorocarbon-polymers as a consequence of the etch chemistry. This process is known as "micromasking", and the resultant formation of surface structures (termed "glass-grass") has been repeatedly described in microfabrication and nanofabrication literature [61]. In typical microfabrication glass-grass is a defect to be avoided, however glass-grass may in fact be highly desirable if the sole purpose of fabrication is to produce SWAR structures. Using a mixture of CHF_3 and SF_6, glass-grass features were realized in SiO_2. Glass-grass features were found to satisfy the subwavelength condition and the feature height was easily controlled by varying the etch time. Provided that glass-grass meets the SWAR criteria and has the appropriate feature height it follows naturally that it should demonstrate strong AR characteristics similar to MEAR structur-

ing. In fact, this effect had already been observed in pure Si etching a number of years ago [63]; until now, however, RIE-grass antireflection has not been demonstrated in SiO_2. This result is of great interest for SWAR applications to space as it helps to alleviate the issue of low manufacturing-throughput, which is a traditional stumbling block in nano and microfabrication. It is unlikely that CubeSat developers would be interested in performing complicated multi-step fabrication processes for each coverglass slip. A single-step approach is therefore greatly preferred. This research has demonstrated that a highly effective AR surface may be fabricated in a single step process: quartz substrates were purchased from a well-known supplier, etched for 45 minutes in CHF_3 and SF_6 and adhered to standard triple junction solar cells with no pre-processing, post-processing or intermediate steps.

The simplicity of the micromasking approach raises the possibility that CubeSat developers could supplement COTS coverglass with a simple one-time etch process, and thereby increase their power budget by $\sim 5\%$. The absence of pre-processing and post-processing requirements significantly lowers the bar for access to this technology, putting subwavelength antireflection well within reach of all CubeSat developers. Microfabrication facilities are now relatively commonplace and indeed, these structures were fabricated using ICP-RIE infrastructure that is over a decade old. Most CubeSat developers would therefore be expected to have ready access to the infrastructure required to replicate these structures and apply the MEAR effect to their own missions.

5.3 Future Work

There are some caveats to implementing SiO_2 SWAR structures in space. First and foremost is that the glass used throughout the research, fused quartz, is known to degrade in the space environment when exposed to radiation. This research focused on the use of quartz as its chemistry is simple and the corresponding etch mechanism is relatively well understood. Many satellites, however, employ cerium-doped borosilicate glass thanks to its lack of discolouration due to radiation damage. For a long-term mission (duration of five or more years) the power-loss due to discolouration in fused-silica is expected to reach 5 to 6%, hence for any interplanetary applications CMO glass will be preferred [76]. Thankfully, the choice of substrate material does not greatly affect the SWAR effect, which is based purely on the geometry of surface features. SWAR structures realized in CMO, CMX or CMG coverglass are expected to perform just as well as those in SiO_2, however the fabrication process will need to be re-visited for these chemistries. Micromasking does still occur when etching borosilicate glass [77], hence single-step fabrication of radiation-tolerant SWAR surfaces may be possible. It is recommended that future work aim to address this issue, as the loss in performance due to radiation damage encountered in a long-term mission will overshadow any increase in performance due to SWAR effects [76, 78].

As mentioned previously, the effect of AO degradation on SWAR surfaces must be determined. It is unlikely that the low ion-bombardment energies found in LEO will be sufficient to cause significant damage to the SWAR surfaces, however this should be verified experimentally. One benefit of adopting CMO, CMX or CMG coverglass is that borosilicate glass exhibits greater tensile strength than pure SiO_2 and is therefore more likely to be resistant to any AO erosion effects. Current plans for the future of this work include a demonstration flight as a hosted payload on board a remote-sensing 3-U CubeSat mission. This mission is expected to provide valuable information on the efficacy of the SWAR effect on orbit, particularly during the type of high-incidence conditions in which SWAR structures would be most useful. In advance of this mission, expected to fly in 2017, SWAR structures should be realized on thin borosilicate glass and the AO response of these structures should be simulated using available ICP-RIE infrastructure.

In addition, it has been shown that it is possible to improve the SWAR-enhancement for a glass/solar-cell system through the application of a second SWAR surface to the rear face of the coverglass [32, 74, 79]. MEAR-enhancement in solar-cell modules consisting of, from bottom to top: a Silicon cell, ethylene vinyl acetate (EVA) layer, polyethylene terephthalate (PET), and glass with MEAR-patterning on both sides. The results of this experiment, conducted by Shin *et al.* are highly suggestive that the application of a MEAR surface to both sides of solar-cell coverglass should double the effect of MEAR enhancement at the

front surface. This experiment did not use traditional coverglass; rather the coverglass was textured on the rear surface, which may have allowed for air-gaps between the glass and PET layer, resulting in an air-glass-air transition. The impedance mismatch due to the transition between glass and PET ($\Delta n = 0.1$) is not expected to be as significant as the transition between air and glass ($\Delta n = 0.46$), hence the observed doubling of the MEAR-effect prompts further investigation. Future research in this field would be well-advised to attempt replication of these results.

We have yet to experimentally verify the survivability of SWAR surfaces in the space environment. Silicon dioxide is known to be resistant to atomic oxygen bombardment–it is often used as a protective coating for more vulnerable materials–however, it is unclear whether the fine structures necessary to maintain the moth-eye effect can survive bombardment for an extended mission. It is entirely possible that subwavelength spacing in the near UV limit (grating period $d < 130nm$) will be incompatible with the mechanical strength required for the space environment. The decision to manufacture SWAR structures using a top down manufacturing process was in part made to alleviate concerns over atomic oxygen and thermal stress. It is reassuring also that the fabrication process itself involves bombardment with atomic oxygen at energies greater than those that would be experienced in LEO, however more study is needed.

5.4 Summary and Closing Remarks

This research explored the potential of subwavelength antireflection structures or "SWAR" structures to increase power generation on CubeSats. The central premise of the research was that the unique properties of SWAR structures could be harnessed to address non-traditional problems of power generation on CubeSats. Specifically, it was postulated that the low reflectance of SWAR structures at high angles of incidence would be uniquely beneficial to CubeSats. This was indeed found to be the case.

The numerical simulation of SWAR and MEAR structures was investigated and ultimately two different simulation regimes were adopted for MEAR surface design. From these two methods, EMT-TMM and RCWA, contour plots of transmittance and reflectance were generated allowing for a comparison of the transmittance of bare glass, $\lambda/4$ AR coated glass, and MEAR-enhanced glass. Transmittance as a function of incident angle and wavelength was convolved with the $AM0$ solar spectrum and the spectral responsivity of the solar cell in order to determine the total amount of power that would be generated by a triple-junction solar cell at all angles of incidence. These functions describing power generation as a function of incidence angle were then propagated through simulated attitude data for CubeSats in a variety of common configurations.

Optimal characteristics for a MEAR structure were investigated through RCWA and EMT-TMM. Design and fabrication rules for SWAR structures in space were discussed and an attempt was made to realize the EMT-TMM and RCWA designed MEAR structures on quartz substrates. The fabrication methods used in this research were deliberately selected for their simplicity and not for their high-fidelity. This decision was made in order to adhere to the low-cost ethos of CubeSat design (inasmuch as nanofabrication can be said to be low-cost) and to lower the barrier to entry for groups interested in replicating this work. Using these techniques two SWAR structures were fabricated according to the designs specified by the EMT-TMM formulation and by the the RCWA simulations. Ultimately a new technique for single-step fabrication of irregular MEAR structures in quartz was demonstrated, which has wide-reaching implications for accessible subwavelength antireflection.

An optical test bed was assembled for experimental validation of the SWAR effect as applied to commercially available solar cells. The EMT-TMM designed SWAR surface did not perform as expected; increased transmission was demonstrated, however the overall effect fell far short of its expected value. SWAR theory suggests that this is caused by insufficient feature height, which causes the SWAR structure to perform inefficiently in the infrared. Structures designed according to the RCWA simulations suggested much taller feature heights and subsequently showed improved performance. The experimentally observed performance of RCWA designed structures was used to calculate the expected impact of

SWAR surfaces using simulated CubeSat attitude. A variety of orbital scenarios and attitude configurations were considered. Ultimately it was determined that a CubeSat engineer could expect a minimum increase in instantaneous power generation of $\sim 5\%$ over untreated glass.

In conclusion this research demonstrated the validity of employing SWAR structures on CubeSats to increase power-generation. Experimental investigation into the SWAR effect revealed that SWAR structures provide outsized increases in solar power-generation at high angles of incidence, as was expected. Further simulations using common CubeSat geometries and orbital configurations revealed that the minimum expected increase in power-production was $\sim 5\%$ and that this effect is further increased during low-light, high-incidence operations. In addition, a single-step fabrication process for SWAR structures was demonstrated which significantly lowers the adoption cost to SWAR technology. The micromasking fabrication approach developed in this thesis is straightforward enough that it may be performed by an unskilled technician with no prior knowledge or experience in nanofabrication. Ultimately this research has demonstrated two main findings. First, that SWAR technology can provide a noticeable increase to power-generation on orbit and can do so passively and with no added weight or volume. Secondly, this research has demonstrated that SWAR technology can be realized quickly and cheaply. Indeed, it is likely that most CubeSat developers already have the capability to fabricate these structures; they were merely unaware that they could do so.

Bibliography

[1] Ho, P., Johannes, J. E., Buss, R. J., and Meeks, E., "Chemical reaction Mechanisms for Modeling the Fluorocarbon Plasma Etch of Silicon Oxide and Related Materials," *Sandia Report*, Sandia National Laboratories, Albuquerque, NM, 2001.

[2] Christophorou, L. G., Olthoff, J. K., and Rao, M. V. V. S., "Electron Interactions with CF_4," *Journal of Physical and Chemical Reference Data*, Vol. 25, Sept. 1996, pp. 1341–1388.

[3] Tarnovsky, V., Kurunczi, P., Rogozhnikov, D., and Becker, K., "Absolute cross sections for the dissociative electron impact ionization of the {CFx} (x = 13) free radicals," *International Journal of Mass Spectrometry and Ion Processes*, Vol. 128, No. 3, 1993, pp. 181 – 194.

[4] Kushner, M. J. and Zhang, D., "An electron impact cross section set for CHF3," *Journal of Applied Physics*, Vol. 88, No. 6, 2000, pp. 3231–3234.

[5] Crew, A. B., Larsen, B. A., Klumpar, D. M., Mosleh, E., Spence, H. E., Legere, J., Blake, J. B., Springer, L., Widholm, M., Driscoll, S., Longworth, S., Smith, S., and O'Brien, T. P., "Focusing on Size and Energy Dependence of Electron Microbursts From the Van Allen Radiation Belts," *Space Weather*, Vol. 10, No. 11, 2012, pp. n/a–n/a, S11004.

[6] Buchen, E. and DePasquale, D., "2014 Nano / Microsatellite Market Assessment," *SpaceWorks Enterprises, Inc.*, 2014.

[7] Swartwout, M., "The first one hundred CubeSats: A statistical look," *JoSS 2pp*, 2014, pp. 213–233.

[8] Bouwmeester, J. and Guo, J., "Survey of worldwide pico- and nanosatellite missions, distributions and subsystem technology," *Acta Astronautica*, Vol. 67, No. 78, 2010, pp. 854 – 862.

[9] Ono, Y., Kimura, Y., Ohta, Y., and Nishida, N., "Antireflection effect in ultrahigh spatial-frequency holographic relief gratings," *Appl. Opt.*, Vol. 26, No. 6, Mar 1987, pp. 1142–1146.

[10] Song, Y. M., Choi, H. J., Yu, J. S., and Lee, Y. T., "Design of highly transparent glasses with broadband antireflective subwavelength structures," *Opt. Express*, Vol. 18, No. 12, Jun 2010, pp. 13063–13071.

[11] Song, Y. M., Jeong, Y., Yeo, C. I., and Lee, Y. T., "Enhanced power generation in concentrated photovoltaics using broadband antireflective coverglasses with moth eye structures," *Opt. Express*, Vol. 20, No. S6, Nov 2012, pp. A916–A923.

[12] Ji, S., Park, J., and Lim, H., "Improved antireflection properties of moth eye mimicking nanopillars on transparent glass: flat antireflection and color tuning," *Nanoscale*, Vol. 4, 2012, pp. 4603–4610.

[13] Wilson, S. and Hutley, M., "The Optical Properties of 'Moth Eye' Antireflection Surfaces," *Optica Acta: International Journal of Optics*, Vol. 29, No. 7, 1982, pp. 993–1009.

[14] Kalem, S., Werner, P., Arthursson, ., Talalaev, V., Nilsson, B., Hagberg, M., Frederiksen, H., and Sdervall, U., "Black silicon with high density and high aspect ratio nanowhiskers," *Nanotechnology*, Vol. 22, No. 23, 2011, pp. 235307.

[15] Lohmueller, T., Brunner, R., and Spatz, J. P., "Improved properties of optical surfaces by following the example of the moth eye," *by A. Mukherjee (Intech, 2010)*, 2010.

[16] Ji, S., Song, K., Nguyen, T. B., Kim, N., and Lim, H., "Optimal Moth Eye Nanostructure Array on Transparent Glass Towards Broadband Antireflection," *ACS Applied Materials and Interfaces*, Vol. 5, No. 21, 2013, pp. 10731–10737.

[17] Xu, H., Lu, N., Qi, D., Hao, J., Gao, L., Zhang, B., and Chi, L., "Biomimetic Antireflective Si Nanopillar Arrays," *Small*, Vol. 4, No. 11, 2008, pp. 1972–1975.

[18] Park, H., Shin, D., Kang, G., Baek, S., Kim, K., and Padilla, W. J., "Broadband Optical Antireflection Enhancement by Integrating Antireflective Nanoislands with Silicon Nanoconical-Frustum Arrays," *Advanced Materials*, Vol. 23, No. 48, 2011, pp. 5796–5800.

[19] Rayleigh, L., "On the Propagation of Waves through a Stratified Medium, with Special Reference to the Question of Reflection," *Proceedings of the Royal Society of London. Series A, Containing Papers of a Mathematical and Physical Character*, Vol. 86, No. 586, 1912, pp. pp. 207–226.

[20] Kim, K.-H. and Park, Q.-H., "Perfect anti-reflection from first principles," *Scientific Reports*, Vol. 3, 2013.

[21] Han, K. and Chang, C.-H., "Numerical Modeling of Sub-Wavelength Anti-Reflective Structures for Solar Module Applications," *Nanomaterials*, Vol. 4, No. 1, 2014, pp. 87.

[22] Janicki, V., Sancho-Parramon, J., and Zorc, H., "Refractive index profile modelling of dielectric inhomogeneous coatings using effective medium theories," *Thin Solid Films*, Vol. 516, No. 10, 2008, pp. 3368 – 3373.

[23] Milster, T., "Physical Optics Simulation in Matlab for High-Performance Systems," *Optical Review*, Vol. 10, No. 4, 2003, pp. 246–250.

[24] Forberich, K., Dennler, G., Scharber, M. C., Hingerl, K., Fromherz, T., and Brabec, C. J., "Performance improvement of organic solar cells with moth eye anti-reflection coating," *Thin Solid Films*, Vol. 516, No. 20, 2008, pp. 7167 – 7170, Proceedings on Advanced Materials and Concepts for Photovoltaics {EMRS} 2007 Conference, Strasbourg, France.

[25] "Standard Solar Constant and Zero Air Mass Solar Spectral Irradiance Tables," .

[26] King, R. R., Fetzer, C., Colter, P., Edmondson, K., Ermer, J., Cotal, H., Yoon, H., Stavrides, A., Kinsey, G., Krut, D., and Karam, N., "High-efficiency space and terrestrial multijunction solar cells through bandgap control in cell structures," *Photovoltaic Specialists Conference, 2002. Conference Record of the Twenty-Ninth IEEE*, May 2002, pp. 776–781.

[27] Park, K.-C., Choi, H. J., Chang, C.-H., Cohen, R. E., McKinley, G. H., and Barbastathis, G., "Nanotextured Silica Surfaces with Robust Superhydrophobicity and Omnidirectional Broadband Supertransmissivity," *ACS Nano*, Vol. 6, No. 5, 2012, pp. 3789–3799.

[28] Lim, H., Jung, D.-H., Noh, J.-H., Choi, G.-R., and Kim, W.-D., "Simple nanofabrication of a superhydrophobic and transparent biomimetic surface," *Chinese Science Bulletin*, Vol. 54, No. 19, 2009, pp. 3613–3616.

[29] Lilienthal, K., Stubenrauch, M., Fischer, M., and Schober, A., "Fused silica 'glass grass': fabrication and utilization," *Journal of Micromechanics and Microengineering*, Vol. 20, No. 2, 2010, pp. 025017.

[30] Tommila, J., Aho, A., Tukiainen, A., Polojrvi, V., Salmi, J., Niemi, T., and Guina, M., "Moth-eye antireflection coating fabricated by nanoimprint lithography on 1eV dilute nitride solar cell," *Progress in Photovoltaics: Research and Applications*, Vol. 21, No. 5, 2013, pp. 1158–1162.

[31] Yamada, N., Ijiro, T., Okamoto, E., Hayashi, K., and Masuda, H., "Characterization of antireflection moth-eye film on crystalline silicon photovoltaic module," *Opt. Express*, Vol. 19, No. S2, Mar 2011, pp. A118–A125.

[32] Shin, J.-H., Go, B.-N., Choi, H.-J., Cho, J.-Y., Sung Soo Lee, A., Hwang, S. S., Cha, H. J., and Lee, H., "Fabrication of functional nanosized patterns with UV-curable polysilsesquioxane on photovoltaic protective glass substrates using hybrid nano-imprint lithography," *J. Mater. Chem. C*, Vol. 2, 2014, pp. 5864–5869.

[33] "Spacecraft Polymers Atomic Ocygen Durability Handbook," *NASA Technical Handbook*, edited by R. Roe, National Aeronautics and Space Administration, Washington, DC, 2014.

[34] Johnston, W. R., OBrien, T. P., Ginet, G. P., Huston, S. L., Guild, T. B., and Fennelly, J. A., "AE9/AP9/SPM: new models for radiation belt and space plasma specification," Vol. 9085, 2014, pp. 908508–908508–9.

[35] Dever, J., Banks, B., de Groh, K., and Miller, S., "Chapter 23 - Degradation of spacecraft materials," *Handbook of Environmental Degradation of Materials*, edited by M. Kutz, William Andrew Publishing, Norwich, NY, 2005, pp. 465 – 501.

[36] Vajpeyi, A. P., Ajagunna, A. O., Tsagaraki, K., Androulidaki, M., and Georgakilas, A., "InGaN nanopillars grown on silicon substrate using plasma assisted molecular beam epitaxy," *Nanotechnology*, Vol. 20, No. 32, 2009, pp. 325605.

[37] Wang, H.-P., Lai, K.-Y., Lin, Y.-R., Lin, C.-A., and He, J.-H., "Periodic Si Nanopillar Arrays Fabricated by Colloidal Lithography and Catalytic Etching for Broadband and Omnidirectional Elimination of Fresnel Reflection," *Langmuir*, Vol. 26, No. 15, 2010, pp. 12855–12858.

[38] Seisyan, R., "Nanolithography in microelectronics: A review," *Technical Physics*, Vol. 56, No. 8, 2011, pp. 1061–1073.

[39] Yu, H.-D., Regulacio, M. D., Ye, E., and Han, M.-Y., "Chemical routes to top-down nanofabrication," *Chem. Soc. Rev.*, Vol. 42, 2013, pp. 6006–6018.

[40] Ventzek, P., Rauf, S., and Sparks, T., "Chapter 21 - Plasma Etch," *Handbook of Semiconductor Manufacturing Technology*, CRC Press, 2nd ed., 2007, pp. 21–1 – 21–69.

[41] Donnelly, V. M. and Kornblit, A., "Plasma etching: Yesterday, today, and tomorrow," *Journal of Vacuum Science and Technology A*, Vol. 31, No. 5, 2013, pp. –.

[42] Ko, D.-H., Tumbleston, J. R., Henderson, K. J., Euliss, L. E., DeSimone, J. M., Lopez, R., and Samulski, E. T., "Biomimetic microlens array with antireflective "moth-eye" surface," *Soft Matter*, Vol. 7, 2011, pp. 6404–6407.

[43] Stavroulakis, P., "Fabrication and characterization of biomimetic antireflective surfaces with reduced glare," .

[44] Vogel, N., Goerres, S., Landfester, K., and Weiss, C. K., "A Convenient Method to Produce Close- and Non-close-Packed Monolayers using Direct Assembly at the AirWater Interface and Subsequent Plasma-Induced Size Reduction," *Macromolecular Chemistry and Physics*, Vol. 212, No. 16, 2011, pp. 1719–1734.

[45] Rybczynski, J., Ebels, U., and Giersig, M., "Large-scale, 2D arrays of magnetic nanoparticles," *Colloids and Surfaces A: Physicochemical and Engineering Aspects*, Vol. 219, No. 13, 2003, pp. 1 – 6.

[46] Zhao, Y., Wang, J., and Mao, G., "Colloidal subwavelength nanostructures for antireflection optical coatings," *Opt. Lett.*, Vol. 30, No. 14, Jul 2005, pp. 1885–1887.

[47] Chen, H. L., Chuang, S. Y., Lin, C. H., and Lin, Y. H., "Using colloidal lithography to fabricate and optimize sub-wavelength pyramidal and honeycomb structures in solar cells," *Opt. Express*, Vol. 15, No. 22, Oct 2007, pp. 14793–14803.

[48] Lee, Y.-C., Chang, C.-C., and Chou, Y.-Y., "Fabrication of broadband anti-reflective sub-micron structures using polystyrene sphere lithography on a Si substrate," *Photonics and Nanostructures - Fundamentals and Applications*, Vol. 12, No. 1, 2014, pp. 16 – 22.

[49] Rybczynski, J., Ebels, U., and Giersig, M., "Large-scale, 2D arrays of magnetic nanoparticles," *Colloids and Surfaces A: Physicochemical and Engineering Aspects*, Vol. 219, No. 13, 2003, pp. 1 – 6.

[50] Sirotkin, E., Apweiler, J. D., and Ogrin, F. Y., "Macroscopic Ordering of Polystyrene Carboxylate-Modified Nanospheres Self-Assembled at the WaterAir Interface," *Langmuir*, Vol. 26, No. 13, 2010, pp. 10677–10683.

[51] Li, Q., Jonas, U., Zhao, X. S., and Kappl, M., "The forces at work in colloidal self-assembly: a review on fundamental interactions between colloidal particles," *Asia-Pacific Journal of Chemical Engineering*, Vol. 3, No. 3, 2008, pp. 255–268.

[52] Stavroulakis, P. I., Christou, N., and Bagnall, D., "Improved deposition of large scale ordered nanosphere monolayers via liquid surface self-assembly," *Materials Science and*

Engineering: B, Vol. 165, No. 3, 2009, pp. 186 – 189, 5th International Workshop on Nanosciences and Nanotechnologies.

[53] Plummer, J. D., Deal, M., and Griffin, P. D., *Silicon VLSI Technology*, Prentice Hall Press, Upper Saddle River, NJ, USA, 2nd ed., 2008.

[54] Jansen, H., Gardeniers, H., de Boer, M., Elwenspoek, M., and Fluitman, J., "A survey on the reactive ion etching of silicon in microtechnology," *Journal of Micromechanics and Microengineering*, Vol. 6, No. 1, 1996, pp. 14.

[55] Hsiao, R. and Carr, J., "Si/SiO2 etching in high density SF6/CHF3/O2 plasma," *Materials Science and Engineering: B*, Vol. 52, No. 1, 1998, pp. 63 – 77.

[56] Bariya, A. J., Shan, H., Frank, C. W., Self, S. A., and McVittie, J. P., "The etching of CHF3 plasma polymer in fluorinecontaining discharges," *Journal of Vacuum Science and Technology B*, Vol. 9, No. 1, 1991, pp. 1–7.

[57] Steinbrchel, C., Lehmann, H. W., and Frick, K., "Mechanism of Dry Etching of Silicon Dioxide: A Case of Direct Reactive Ion Etching," *Journal of The Electrochemical Society*, Vol. 132, No. 1, 1985, pp. 180–186.

[58] Gaboriau, F., Cartry, G., Peignon, M.-C., and Cardinaud, C., "Etching mechanisms of Si and SiO 2 in fluorocarbon ICP plasmas: analysis of the plasma by mass spectrometry,

Langmuir probe and optical emission spectroscopy," *Journal of Physics D: Applied Physics*, Vol. 39, No. 9, 2006, pp. 1830.

[59] Schaepkens, M., Standaert, T. E. F. M., Rueger, N. R., Sebel, P. G. M., Oehrlein, G. S., and Cook, J. M., "Study of the SiO2-to-Si3N4 etch selectivity mechanism in inductively coupled fluorocarbon plasmas and a comparison with the SiO2-to-Si mechanism," *Journal of Vacuum Science and Technology A*, Vol. 17, No. 1, 1999, pp. 26–37.

[60] Rueger, N., Doemling, M., Schaepkens, M., Beulens, J., Standaert, T., and Oehrlein, G., "Selective etching of SiO2 over polycrystalline silicon using CHF3 in an inductively coupled plasma reactor," *Journal of Vacuum Science and Technology A*, Vol. 17, No. 5, 1999, pp. 2492–2502.

[61] Ross, R. J., ASM International, 2011.

[62] Grigoras, K. and Franssila, S., "Formation of Nanoporous Glass Layer," *Physica Scripta Volume T*, Vol. 114, Jan. 2004, pp. 66–68.

[63] Bi, Y., Su, X., Zou, S., Xin, Y., Dai, Z., Huang, J., Wang, X., and Zhang, L., "Plasma-etching fabrication and properties of black silicon by using sputtered silver nanoparticles as micromasks," *Thin Solid Films*, Vol. 521, No. 0, 2012, pp. 176 – 180, The 3rd International Conference on Microelectronics and Plasma Technology (ICMAP) 2011.

[64] Scheeler, S. P., Ullrich, S., Kudera, S., and Pacholski, C., "Fabrication of porous silicon by metal-assisted etching using highly ordered gold nanoparticle arrays," *Nanoscale research letters*, Vol. 7, No. 1, 2012, pp. 1–7.

[65] Kolari, K., Saarela, V., and Franssila, S., "Deep plasma etching of glass for fluidic devices with different mask materials," *Journal of Micromechanics and Microengineering*, Vol. 18, No. 6, 2008, pp. 064010.

[66] Williams, K. R., Gupta, K., and Wasilik, M., "Etch rates for micromachining processing-Part II," *Microelectromechanical Systems, Journal of*, Vol. 12, No. 6, 2003, pp. 761–778.

[67] Koynov, S., Brandt, M. S., and Stutzmann, M., "Black nonreflecting silicon surfaces for solar cells," *Applied Physics Letters*, Vol. 88, No. 20, 2006, pp. –.

[68] Asadollahbaik, A., Boden, S. A., Charlton, M. D. B., Payne, D. N. R., Cox, S., and Bagnall, D. M., "Reflectance properties of silicon moth-eyes in response to variations in angle of incidence, polarisation and azimuth orientation," *Opt. Express*, Vol. 22, No. S2, Mar 2014, pp. A402–A415.

[69] Parretta, A., Sarno, A., and Yakubu, H., "Non-destructive optical characterization of photovoltaic modules by an integrating sphere.: Part I: Mono-Si modules," *Optics Communications*, Vol. 161, No. 46, 1999, pp. 297 – 309.

[70] Di Mundo, R., Ambrico, M., Ambrico, P. F., d'Agostino, R., Italiano, F., and Palumbo, F., "Single-Step Plasma Process Producing Anti-Reflective and Photovoltaic Behavior on Crystalline Silicon," *Plasma Processes and Polymers*, Vol. 8, No. 3, 2011, pp. 239–245.

[71] Chuang, S.-Y., Chen, H.-L., Shieh, J., Lin, C.-H., Cheng, C.-C., Liu, H.-W., and Yu, C.-C., "Nanoscale of biomimetic moth eye structures exhibiting inverse polarization phenomena at the Brewster angle," *Nanoscale*, Vol. 2, 2010, pp. 799–805.

[72] UOZU, Y., "Continuous Roll Imprinting of Moth Eye Antireflection Surface Using Anodic Porous Alumina," *Design for Innovative Value Towards a Sustainable Society*, edited by M. Matsumoto, Y. Umeda, K. Masui, and S. Fukushige, Springer Netherlands, 2012, pp. 915–917.

[73] Chen, Q., Hubbard, G., Shields, P. A., Liu, C., Allsopp, D. W. E., Wang, W. N., and Abbott, S., "Broadband moth-eye antireflection coatings fabricated by low-cost nanoimprinting," *Applied Physics Letters*, Vol. 94, No. 26, 2009, pp. –.

[74] Hong, S.-H., Bae, B.-J., Han, K.-S., Hong, E.-J., Lee, H., and Choi, K.-W., "Imprinted moth-eye antireflection patterns on glass substrate," *Electronic Materials Letters*, Vol. 5, No. 1, 2009, pp. 39–42.

[75] Clark, E., Kane, M., and Jiang, P., *Performance of Moth Eye Anti-Reflective Coatings for Solar Cell Applications*, Mar 2011.

[76] Russell, J. and Jones, G., "Radiation testing of coverglasses and second surface mirrors," *Materials in a Space Environment*, edited by K. Fletcher, Vol. 540 of *ESA Special Publication*, Sept. 2003, pp. 643–648.

[77] Thinot, E., Domingo, F., Cambril, E., and Gosse, C., "Reactive ion etching of glass for biochip applications: Composition effects and surface damages," *Microelectronic Engineering*, Vol. 83, No. 49, 2006, pp. 1155 – 1158, Micro- and Nano-Engineering {MNE} 2005Proceedings of the 31st International Conference on Micro- and Nano-Engineering.

[78] Haynes, G., Aeronautics, U. S. N., Administration, S., and Center, L. R., *Effect of Radiation on Cerium-doped Solar-cell Cover Glass*, NASA technical note, National Aeronautics and Space Administration, 1970.

[79] Raut, H. K., Dinachali, S. S., He, A. Y., Ganesh, V. A., Saifullah, M. S. M., Law, J., and Ramakrishna, S., "Robust and durable polyhedral oligomeric silsesquioxane-based anti-reflective nanostructures with broadband quasi-omnidirectional properties," *Energy Environ. Sci.*, Vol. 6, 2013, pp. 1929–1937.